1-1-2012

Metal chalcogenide nanoparticle gel networks: their formation mechanism and application for novel material generation and heavy metal remediation via cation exchange reactions

Irina Ramona Pala
Wayne State University,

METAL CHALCOGENIDE NANOPARTICLE GEL NETWORKS: THEIR FORMATION MECHANISM AND APPLICATION FOR NOVEL MATERIAL GENERATION AND HEAVY METAL WATER REMEDIATION VIA CATION EXCHANGE REACTIONS

by

IRINA R. PALA

DISSERTATION

Submitted to the Graduate School

of Wayne State University,

Detroit, Michigan

in partial fulfillment of the requirements

for the degree of

DOCTOR OF PHILOSOPHY

2012

MAJOR: CHEMISTRY (Inorganic)

Approved by:

_____

Advisor Date

_____

_____

_____

DEDICATION

To my dear great-grandmother, Rozalia Paraon, who taught me to read and write

ACKNOWLEDGEMENTS

I would not be able to write this today, had it not been for the great guidance provided by my advisor, Prof. Stephanie Brock. She is the epitome of what a dedicated, passionate and knowledgeable mentor should be. Her deep understanding of the scientific and interpersonal aspects of the graduate research experience is only paralleled by her utmost professionalism and simultaneous personable approach to dealing with the multitude of issues presented in such a diverse environment. She was the one to always keep me as focused as possible, to slowly but surely ensure that I hone my skills and I achieve my goals. Under her calm and strong advice, I grew as a person and as a professional scientist and I want to thank her from the bottom of my heart.

I would also like to thank my dissertation committee members, Prof. Matthew Allen, Prof. Vladimir Chernyak and Prof. Gavin Lawes, for always being available for comments and suggestions and making time in their busy schedule to ensure that the program deadlines were met. Many thanks go to Prof. Claudio Verani and Prof. David Rueda for writing recommendation letters for me and sending them in time.

To all my Chemistry teachers, starting with my 7th grade teacher Corina Lazarovici, to my dear high school teacher Vasile Gheorgita (R.I.P), to my undergraduate research advisors Dr. Sheila Smith, Dr. Craig Donahue, Dr. William Kaiser and Dr. Krisanu Bandyopadhyay: you have started and kept the passion throughout the years and I was so fortunate to be your pupil and to benefit from your knowledge. Thank you.

I want to thank my collaborators from Weinberg Physics, LLC: Dr. Irving Weinberg, Dr. Pavel Stepanov, Dr. Mario Urdaneta and Dr. Andrew Watt for providing me with financial support and allowing me to participate in a research project that

introduced me to the slightly different approach of industry. I would also like to thank Wayne State University, the Graduate School and the Department of Chemistry for the opportunity to carry out my dissertation research here and for the recognition and support offered through various awards and fellowships. I am most thankful for the opportunity to be a teaching assistant and I thank Dr. Barber in particular for her teachings.

I want to thank all the staff members in the Department of Chemistry, especially Melissa Barton, Debbie McCreless, Diane Kudla, Bernie Miesik, Mary Wood and Diane Klimas. They are all wonderful to work with, knowledgeable and always willing to help. I also thank the staff members of the Science Stores for always ensuring the chemicals and apparatus I ordered got here in time. The help that Nestor Ocampo was always ready to provide when it came to IT stuff and poster deadlines is also much appreciated.

A bunch of thanks are given to the former Brock group members who were there for me during the beginning of my PhD endeavor. Dr. Qinghong Yao has been one of the first to teach me the ways of the lab, both in the synthesis and in the human aspects, and I want to thank her immensely. She has been and continues to be a good friend, whose friendship and advice I will always treasure. I must also thank Dr. Hongtao Yu for his unique way of sharing his knowledge; he taught me to be detail-oriented and persistent if I want to succeed in my inquiries. I thank Dr. Indika Arachchige for passing along some of his knowledge and inspiration for research projects in the short time we spent together. I would also like to thank Dr. Kennedy Kalebaila and Dr. Keerthi Senevirathne for the good interactions and answers to questions. Dr. Elayaraja Muthuswamy has been a good friend, also, and I thank him for the help given with instrumentation, software and synthesis suggestions, but also for his quirky sense of humor and dedicated contributions

to the PR 720˚ broadcasts. I would also like to acknowledge the current members of the Brock group. I thank my classmate, Dr. Shreyashi Ganguly, for taking this journey with me. We've been together through good times and bad, and I hope we will continue to support each other in the future. I am also fortunate to have had the rest of the group as my colleagues: Yanhua Zhang, Layan Savithra, Lasantha Perera, Asha Bandara, Roshini Pimmachcharige and Derak James. I want to thank them for the research discussions, lively outings and parties, coffee breaks and overall keeping a friendly atmosphere that made graduate life so much easier. To the newest members, Jessica and Ruchira I thank for the nice interactions and wish them best of luck in their careers.

My friends who have been there for me in the past few months: Dajena, Fernando, Tomasz, David, Jean Paul, Myriame, Batiste, Eric, Rebecca, Jeremy and Derek deserve thanks for helping keep my sanity level at acceptable values. To my dear friends Anca and Catalin Nastasa I extend my deepest thanks for effectively taking care of me and pulling me out every time I fell into any kind of trouble. I also thank my lady friends in the Lady Circle for allowing periodic venting rituals accompanied by a nice glass of wine. I would like to thank Dr. Rama Shanmugam for her friendship and good talks.

In the end, I want to thank my always-changing family for their support and love throughout all my endeavors. I thank my mother for making sure I understood that the only thing I was slightly good at was school and therefore being the main reason why I don't seem to want to do anything else anymore. I thank my father because, in a way that he thought was the right one, instilled in me the desire to always be the best at whatever I do.

Here is to a new start, which might bring about a new beginning…

TABLE OF CONTENTS

LIST OF TABLES

LIST OF FIGURES

LIST OF SCHEMES

CHAPTER 1

INTRODUCTION

The dissertation research studied the synthesis, characterization and application of semiconducting metal chalcogenide gel networks. The main goals were to (1) investigate the mechanism of metal chalcogenide nanopaerticle (NP) gel formation, (2) explore the cation exchange ability of ZnS gel networks for the generation of new aerogel materials and for understanding the driving forces behind the process, and (3) quantify the ability of ZnS aerogels to remove heavy metals from aqueous solutions. This first chapter provides background introductory information on semiconducting materials, especially metal chalcogenide nanomaterials, their synthesis and assembly methods. Sol-gel chemistry and cation-exchange reactions are two of the areas of study of the dissertation research, and are therefore introduced, as well. The status of water remediation materials and procedures, mainly of those using cation exchange materials, is also presented.

1.1 Semiconducting NPs

"Nanomaterials" and "nanotechnology" have become buzz words in most gatherings of the scientific research community. Usually associated with artificially achieved materials of recent origin, nanomaterials have been surrounding us, and have been part of us, since the beginning of time. Examples of such include beautiful structures like DNA, the ultimate nanomaterial, with an intricate combination of form and function, or the amazing light-into-energy converter photosynthetic nanofactory found in all green leaves. The fever from the nanotechnology bug started once scientists realized the plethora of

new properties and applications that can be accessed and capitalized upon when materials reach this unique nano-scale domain. As it emerges from its infancy, the main goal of nanotechnology today is to develop new functional materials. To achieve this goal, it is necessary to exploit and enhance the functional performance of the NP for the achievement of optimum properties. The challenge comes in the effort of developing new synthetic strategies and materials using *rational* chemistry, with the ability to control the composition, size, shape and structural aspects of the desired NPs.

Bulk inorganic materials are classified based on their electronic conductivity into three groups: metals, semiconductors and insulators. Metals are regarded as consisting of a lattice of positive cores surrounded by a freely moving sea of electrons that renders them electronically conducting. Semiconductors (materials from group IV, III-V, II-VI or IV-VI) have a filled electronic band (the valence band) and an empty band (the conduction band).[1] These two bands are analogous to the highest occupied molecular orbital (HOMO) and lowest unoccupied molecular orbital (LUMO) in molecules. As atoms or ions are packed together to form the bulk solid, the electronic HOMO and LUMO levels combine to form bands. The separation between the conduction and valence bands is between 0.3 and 3.8 eV depending on the material, and it is known as the band gap energy (E_g).[1, 2] Conductivity occurs when sufficient energy is provided to promote electrons from the valence band to the conduction band. In insulating materials, the band gap energy is very large (> 4 eV), and the materials do not conduct electricity.

NPs, defined as materials that have at least one dimension below 100 nm, and thus having a limited number of atoms in their composition, exhibit an electronic structure intermediate between the molecular and bulk materials. The restriction in size

causes the electrons to follow the "particle in a box" model, and the electronic levels within the conduction and valence bands become quantized, instead of being continuous, as is the case in bulk. More specifically, when the NP size is smaller than a critical characteristic size of the bulk-exciton Bohr radius,[3-5] electronic energy levels split, according to Pauli's exclusion principle. Thus, in semiconductors, the band gap energy increases in NPs with respect to bulk, yielding the phenomenon referred to as the "quantum confinement effect". That is why semiconducting NPs are also named "quantum dots" (QDs). For a specific material and temperature, the band gap energy is dependent on the quantum dot size, with smaller dots having larger band gap energies. The quantum confinement effect on the band gap energy is exemplified in Figure 1.1 and imparts unusual opto-electronic characteristics to QDs. Upon irradiation with light with energy higher than E_g, an electron from the valence band can be excited into the conduction band, leaving a hole in the valence band. This results in an absorption peak in the spectrum. Since the E_g value is dependent on the particle size, the position of the absorption peak also shifts to higher wavelengths (lower energies) as the particle size increases. Also, upon the electron relaxation from the conduction to the valence band, the energy can be emitted as light, conferring photoluminescent properties. Thus, the emission wavelength is also size dependent and tunable. The ability to control and tune the optical emission and absorption properties by changing the particle size spurred numerous investigations into the use of QDs in applications such as imaging and labeling,[6] photovoltaics,[7-10] photodetectors,[11] and sensors.[12-14]

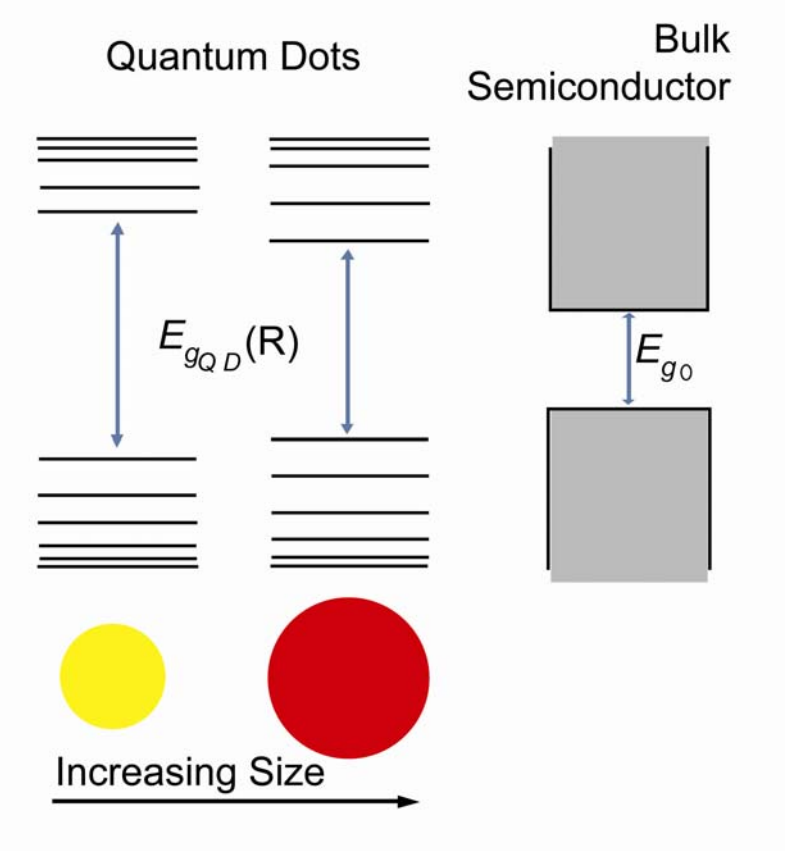

Figure 1.1. Schematic representation of the electronic states in nanoscale and bulk semiconductors, showing the increase of the band gap energy (E_g) with the decrease in particle size (adapted from Steigerwald and Brus[3])

Another characteristic of QDs is their high surface to volume ratio. As the particle size decreases, a higher percentage of atoms are surface atoms, and can result in the presence of surface imperfections and dangling bonds. This causes the availability of energy levels that are usually located within the QDs bandgap, creating surface trap states. These trap states can provide an alternate path for electrons or holes to recombine, affecting the overall performance of devices that depend on the QDs emission properties. Usually, these trap state emissions cause the lowering of the overall fluorescence

quantum yield, the presence of broad fluorescence ranges or the phenomenon of blinking because of charge recombination pathways.[6] To eliminate the side effects created by the presence of surface defects, two main pathways have been adopted. The first uses a combination of two or more semiconductors forming heterojunctions in a core-shell fashion, passivating the QD surface. Usually, a material with a wider bandgap is used to surround the core and effectively trap the electron and hole within the electronic energy levels of the core semiconductor.[15] A second pathway involves the use of certain organic coordinating ligands such as alkyl amines, alkyl phosphine oxides or fatty acids[16] to passivate the QD surface. This approach is usually less effective than the use of an inorganic passivating shell in eliminating the trap states.

1.2 Metal chalcogenide NPs

One of the factors driving the current research in nanoscale materials is the need for constant miniaturization of optical and electronic devices. Semiconducting metal chalcogenide NPs (II-VI and IV-VI) have received particular interest, due to the strong quantum confinement behavior that they exhibit in the 1–20 nm range. Therefore, significant progress has been made in the synthesis of materials such as CdSe, CdS, CdTe, ZnS, ZnSe, PbS, PbSe and PbTe with controlled sizes and shapes. The precise control of size and shape is very important when investigating the physical properties of the NPs. For example, by manipulating the size and composition of the particles, band gap energies that span from the mid–to–near infrared (PbS, PbSe, PbTe), to visible (CdSe, CdS, CdTe) and even into the ultraviolet (ZnS, ZnSe) can be accessed. Several synthetic routes[3, 17, 18] have been most successful in producing high quality metal

chalcogenide NPs. For the dissertation research, the II-VI metal chalcogenides (CdSe, CdS and ZnS) are of interest, and their synthetic strategies will be discussed further. The two main types of colloidal chemistry used for the preparation of metal chalcogenide NPs are the arrested precipitation in solution (room temperature synthesis) and the molecular precursor method (high temperature synthesis).

1.2.1 Synthesis of metal chalcogenide NPs using the arrested precipitation method

Controlled precipitation reactions can be performed in inverse micelle solutions (i.e. AOT/H_2O/heptane, where AOT= sodium bis(2-ethylhexyl)sulfosuccinate) to yield dilute suspensions of almost monodisperse NPs and were first reported in the 1980s.[19-21] Materials such as CdS, CdSe and ZnS were produced using such methods.[22, 23] The method involves the mixing of two separate dilute aqueous solutions of the metal ion and the chalcogenide ion that have been previously dispersed in a much larger volume of nonpolar solvent (i.e. heptane) and surfactant (AOT), resulting in the formation of the metal chalcogenide particles inside the confined inverse micellar nano-reactors.[24] The size of the resulting NP is controlled by the micelle size, which can be tuned by varying the ratio of the surfactant to water.[25] The NPs thus formed have bare surfaces, which are usually then capped using organic ligands.[23] This room temperature route provides a cheap route for the formation of many NP chemistries. At the same time, the low temperature also causes any initial defects to be trapped in the material, resulting in NPs that are usually poorly crystalline, and are therefore poorly luminescent.[26]

1.2.2 Synthesis of metal chalcogenide NPs using the molecular precursor method

This powerful synthetic method was first reported in 1993 for the synthesis of CdSe NPs by injecting $(CH_3)_2Cd$ and tri-*n*-octylphosphine selenide (TOPSe) into hot (120–300˚C) tri-*n*-octylphosphine oxide (TOPO).[27] The resulting TOPO-capped NPs can be dispersed in non-polar solvents and are monodisperse and highly crystalline, exhibiting sharp band-edge emission. This synthetic method was one of the first that triggered a slew of other studies meant to finally rationalize the mystery of the controlled NP synthesis. Thus, the concept of "size distribution focusing"[28] has been proposed to explain the formation of monodisperse NPs. According to this concept, the key for size control lies in having a fast nucleation event at high temperature, followed by slower growth of the particles at lower temperature. This is achieved by using the strong size-dependent solubility properties of NPs in solution. Upon a rapid injection of the chalcogenide precursor into a hot (i.e. 300˚C) coordinating solvent containing the metal precursor, the local precursor concentration increases above the nucleation threshold, forming metal chalcogenide nuclei.[29] The nucleation is then stopped by reducing the temperature (150–250˚C), and the precursors still present in solution serve for the slow, uniform growth of material onto the existing nuclei, resulting in particles of almost uniform size.[30]

Usually, the high temperature synthesis of metal chalcogenide NPs uses long chain alkylphosphines and alkylphosphine oxides or amines as the coordinating solvents.[27] These species have a dual role in the process: that of providing the reaction medium, and at the same time acting as stabilizers, preventing the particle aggregation and passivating the surface dangling bonds.[23] If solubility in polar solvents is desired, as required for

applications in biological media, the dynamic nature[31] of the surfactant-NP interaction allows for the exchange of the non-polar surface group with polar ones, such as mercaptoundecanoic acid, mercaptoacetic acid, or dihydrolipoic acid, usually in base.[32] These particles have been proven to be less stable than their non-polar-capped brethren, and particle precipitation often occurs over time.

Another step in the right direction in the synthesis of metal chalcogenide NPs came with the reported replacement of the highly toxic $(CH_3)_2Cd$ by the air-stable CdO or $Cd(OOCCH_3)_2$.[33] The NPs produced thusly have comparable quality to those synthesized using $(CH_3)_2Cd$ as the precursor, having good size dispersity, crystallinity and band-edge luminescence. This improvement has been widely adopted by the NP community and has spurred a multitude of studies on these systems.

1.3 NP assembly methods

As we stand today, nanomaterials have already been used in applications such as bio-imaging,[6] photovoltaics,[7-10] light emitting diodes, sensors,[12-14] catalysts[34] and thermoelectrics.[35, 36] Many more applications of these materials are envisioned and the improvement of their performance by better control and understanding of the chemistry that occurs on the nano-scale is expected. To date, a lot of effort has been focused on the synthesis of various materials with nano-scale dimensions; controlling their size,[27] shape,[37] solubility;[38] and determining their properties. However, achieving the envisioned nanotechnology applications and performance requires going past the synthesis of discrete NPs and assembling them into 3D solid-state structures that maintain the size-dependent optical, electronic and magnetic properties of the NP building blocks. To reach

this goal, various techniques such as the top-down (carving your way from macro- to nano-scale using lasers) or the bottom-up (assembling the NPs together using organic ligands as linkers or van der Waals interactions) methods have been used. The former suffers from the need for costly, sophisticated instrumentation, and the latter from reduced electronic transport through the network due to the presence of organic linkers or feeble assemblies that result from the weak van der Waals interactions. Since 3D assemblies of NPs are relevant to the dissertation research, the bottom-up assembly methods will be discussed in more detail in this section. Two of the most commonly used approaches are the layer by layer assembly and the self-assembly of close-packed NPs.

The layer-by-layer (LbL) method was first described in 1991[39]; it uses the alternating electrostatic deposition of polyanionic and polycationic species onto solid substrates. The same concept can be extended to the assembly of NPs using oppositely charged polyelectrolytes.[40] The components of successive layers need not be the same but can be varied, resulting in assemblies with practically unlimited compositions. Also, the thickness and the function can be varied. The method is quite general and can be applied to most NP systems, as long as they can participate in the charge-overcompensation responsible for the electrostatic attraction between successive layers. One of the deficiencies of the LbL technique is that the minimum distance between two NP layers can not be decreased below the thickness of the polyelectrolyte used, which is at least several Ångstroms, thus limiting the efficiency of inter-layer interactions (i.e. electrical conductivity). To try and circumvent this limitation, the LbL technique was adapted by assembling NPs that were rendered with opposite charges by the stabilizer used for surface coating.[41] This has resulted in the decrease of the distance between NP layers to

the extent of the thickness of the stabilizer shell, but it also decreased the stability of the assembly.

Assemblies constructed by the self-organization of close-packed NPs use the slow evaporation of the NP solution solvent. By controlling the reaction parameters such as the choice of solvent, ambient temperature and humidity, assemblies consisting of colloid glasses with local order or superlattice structures with long range order can be obtained.[42] Just like in the LbL method, the separation between NPs is controlled by the thickness of the capping group layer, which presents the same drawbacks for applications that require charge carrier transport between particles.

1.4 The sol-gel assembly: gels, aerogels, xerogels

An alternate assembly technique is provided by the sol-gel method, by which NPs can be directly assembled, without any intervening ligand, to produce highly porous structures. Historically, this technique has been limited to insulating metal oxide materials,[43] such as SiO_2, Al_2O_3 and TiO_2. Typically, the sol gel process involves the hydrolysis and condensation of a metal alkoxide ($M(OR)_n$) precursor.[44-46] In the hydrolysis step, the metal alkoxide precursor reacts with water to form alcohols and hydroxylated metal centers (Equation 1.1). In the second step, the hydroxylated metal centers undergo condensation, generating M-O-M bonds that connect the particles together, while eliminating water and alcohol (Equation 1.2). These bonds connect the nano-sized particles together, generating a wet gel network.

(1) Hydrolysis

$$M(OR)_n + H_2O \rightarrow M(OR)_{n-1}(OH) + ROH \qquad (1.1)$$

(2) Condensation

$$\text{M-OH} + \text{M-OX} \rightarrow \text{M-O-M} + \text{X-OH} \quad (\text{X= H or R}) \qquad (1.2)$$

Silica is one of the most studied systems for the sol-gel chemistry. For the sol-gel synthesis of silica gels, the morphology of the final gel network is dependent on the reaction pH.[45] When the reaction is catalyzed by an acidic medium (pH = 2–5), the hydrolysis step is favored and the rate determining step is the condensation process. This results in the simultaneous formation of a high number of oligomers, and the final gel network has a polymer-like morphology and low porosity.[43] When a basic pH is used, the hydrolysis step becomes rate determining, yielding a gel that consists of an interconnected network of colloidal particles, with high porosity and higher surface area than the acid-catalyzed gels.

The wet gels obtained from the initial sol-gel reactions can be dried in one of three ways. If the drying occurs directly from the mother liquid (usually water or an alcohol), under ambient conditions, the capillary forces existent at the liquid-vapor interface act on the gel network pore walls, causing the collapse of the pore structure as the solvent evaporates. The final result is dense dry gel with reduced volume, surface area and porosity, which is designated as a xerogel.[45]

When maintaining the surface area and porosity of the wet gel is of interest, an alternative drying method can be used. This uses a supercritical fluid as the drying solvent. In this case, the liquid-vapor interface vanishes, as do the capillary forces acting on the pore walls. The result is a dry gel that maintains the volume, porosity and surface

area of the wet gel, and also exhibits very low density and is therefore known as an aerogel.[45]

Theoretically, pressure and temperature can be adjusted to bring most solvents in the supercritical state, which makes supercritical drying amenable for a variety of systems. In practice, though, there are safety issues related to some of the high pressures and temperatures required by certain solvents (i.e. ~250˚C and 5-8 MPa for alcohols or acetone). The harsh conditions also result in damage to the gel network, resulting in densification of the network, loss of stoichiometry or phase separation.[45] Consequently, the use of CO_2 as the supercritical fluid has become the main drying procedure. The main advantage of using CO_2 is the fact that it is supercritical at relatively low temperatures (30–40˚C) and at similar pressures as the organic solvents (~ 8MPa). As a result, the final aerogel shows very little shrinkage when compared to the wet gel, and the porosity and surface area are maintained, also.

A third way of drying the wet gels is by first exchanging the mother liquid polar solvent with a non-polar one (e.g. hexane), followed by drying under ambient conditions. Due to the lower surface tension of the solvent, the collapse of the pore walls is minimized when compared to drying a polar-solvent filled gel. As a result, the final gel has a volume, porosity and surface area that is intermediate between those of an aerogel and a xerogel, being known as an ambigel.

1.5 Previous studies on metal chalcogenide gels and aerogels

Traditionally, the sol-gel chemistry employed in the synthesis of aerogel materials was limited to oxide and carbon-based compositions. Recognizing the distinct properties

of metal chalcogenides (i.e. semiconducting behavior with tunable band gaps in the visible range of the spectrum and soft Lewis basicity), researchers have investigated the expansion of aerogel chemistries to include such metal chalcogenide frameworks. Accordingly, in a direct analogy to the hydrolysis process used for metal oxide gel syntheses, thiolysis reactions between H_2S and metal alkoxides, thiolates, or amides have been used to access metal chalcogenide gels.[47-57] Suitable metal precursors for the thiolysis reaction are limited in number, and the materials obtained were mostly amorphous or poorly crystalline gels or precipitates (TiS_2,[48] GeS_x,[53, 56, 57] ZnS,[54] LaS_2,[50] WS_x,[55] NbS_2,[49] and YS_x[51]). A $GeS_{2.4}$ aerogel with an amorphous structure and high surface area (up to 755 m^2/g) was obtained by supercritically drying a wet gel obtained via the thiolysis reaction.[58] Nevertheless, the handling and synthetic requirements (complete exclusion of water or oxygen from the reaction) limits the extension and feasibility of this route for the development of other metal chalcogenide gels.

An alternate method of generating metal chalcogenide gels first reported in 2000 uses condensation reactions between small anionic Zintl clusters (i.e. $[Ge_4S_{10}]^{4-}$) and linking transition metal cations (i.e. Zn^{2+}, Cd^{2+}, Hg^{2+} or Co^{2+}).[59] This approach has demonstrated considerable versatility, mainly due to the various available building blocks. Consequently, a new class of chalcogenide aerogels was obtained that exhibits characteristic properties (optical, catalytic, structural) that stem from the geometry of the Zintl clusters and the coordination mode of the metal used. To date materials such as $Pt_2[Ge_4S_{10}]$,[60] $CoMoS_4$, $NiWS_4$,[61] Zn_2SnS_4, $Zn_2Sn_2S_6$, $Zn_2Sn_4S_{10}$,[62] were synthesized and their applications for heavy metal remediation from aqueous solutions and hydrodesulfurization of fossil fuels, evaluated. The highly polarizable nature of the

chalcogenide framework, combined with the large surface area characteristic of aerogels have imparted better activity to the metal chalcogenide aerogels, when compared to traditional remediation or catalytic materials.[60, 62]

Another approach for accessing chalcogenide aerogels uses condensation reactions between discrete metal chalcogenide NPs. In 1997, Gacoin and co-workers[24, 63] reported the use of a two-step sol-gel synthesis for the preparation of CdS gels. The first step consisted of the synthesis of 4-fluorophenylthiolate (FPhSH) capped CdS NPs using the inverse micelle route. The colloidal gel formation was achieved by the controlled oxidation of the CdS NP sol with H_2O_2. The same group reported on the optimization of the gelation conditions to allow for the control of the reaction kinetics, yielding gel networks, as opposed to precipitates. They have also used ^{19}F NMR analyses to confirm the fact that the organic capping ligands had no role in the particle-particle bonding.[26]

The Brock group published the first report of a CdS aerogel[64] using the two-step sol-gel strategy developed by Gacoin and following it with supercritical drying. The same strategy was also used for the preparation of PbS, ZnS and CdSe aerogels.[22] The resultant aerogels have high porosity and high surface area (up to 250 m^2/g), comparable to the traditional silica aerogels. The aerogels have the characteristic base-catalyzed silica gel morphology, in which the crystalline metal chalcogenide NPs are assembled into a 3D connected network. Nevertheless, the opto-electronic properties of the aerogels show that the quantum confined nature of the NP building blocks is maintained even after the gel network is formed.[22, 64] The optical features of the aerogels can be tuned by using precursor NPs of different sizes,[25] by post-synthetic mild heat treatments,[22, 64] or by tuning the density of the network.[65] However, even though quantum confined, the

luminescent properties of the initial aerogels were poor, mostly due to the low crystallinity and surface defects inherent to the low temperature NP synthesis route used. The issue was addressed by investigating the use of a high-temperature arrested precipitation method[33] for the synthesis of highly crystalline CdSe NP precursors. The aerogels formed by subsequent supercritical drying of these CdSe NPs showed a significant enhancement in their band-edge emission.[66] Moreover, the PL was even further enhanced by surface passivation techniques using organic (i.e. pyridine wash of wet gels) or inorganic (ZnS capping shell treatment of the CdSe cores)[66, 67] methods. The effect of the NP precursor morphology[68, 69] (sphere, rod, branched and hyperbranched) and network density[65] (tuned by varying the amount of oxidizing agent used) on the final structural and optical properties of the resultant aerogels was also investigated. Recently, the two-step sol-gel methodology has been expanded to metal tellurides. Accordingly, aerogels of CdTe,[70, 71] PbTe and Bi_2Te_3,[35, 36] were synthesized. Also, the exploration of possible applications was addressed by evaluating the ability of CdSe aerogels to act as a sensor for amines[72] and that of PbTe/Bi_2Te_3 aerogels for thermoelectric materials.[35, 36]

1.6 Cation exchange reactions in bulk and nano-materials

Cation-exchange reactions are well known and involve the replacement of a metal cation in a solid with a mobile cation in solution.[73] The general process for the cation-exchange reaction of metal chalcogenides can be represented by equation 1.3

$$M_1A_{(s)} + M_2^{n+}{}_{(solv.)} \rightarrow M_2A_{(s)} + M_1^{m+}{}_{(solv.)} \quad (1.3)$$

where M_1 = Zn, Cd; A = S, Se, Te; M_2^{n+} = an incoming metal cation.

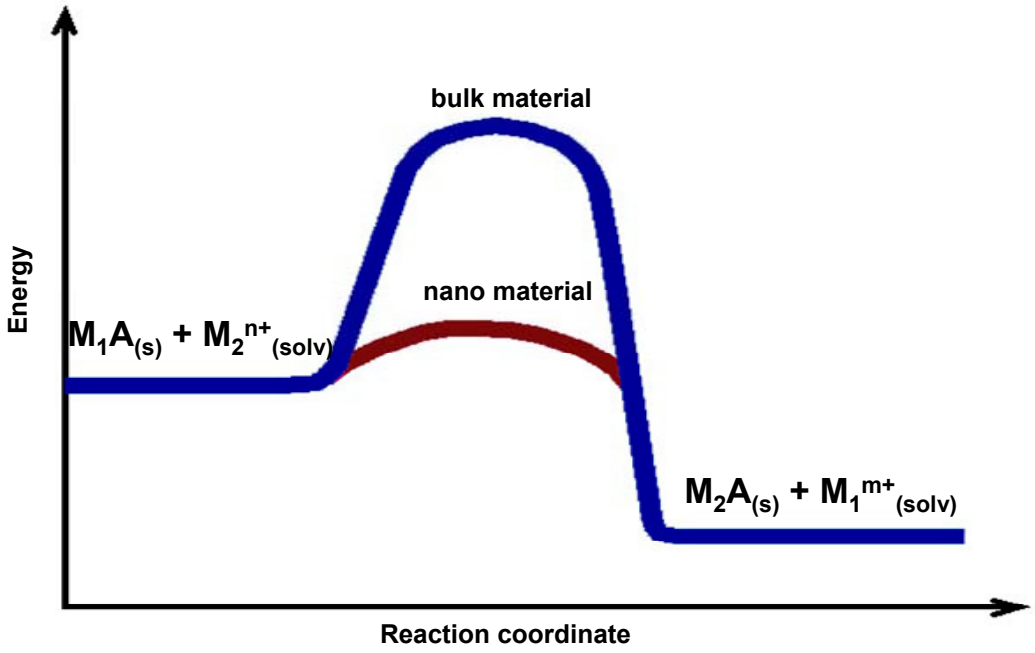

Figure 1.2. Reaction coordinate representing the cation exchange reaction in bulk and in nanoscale materials

The application of cation exchange reactions, though thermodynamically favored when exchangers with appropriate solubility product constants are used, is practically impeded in bulk materials by the slow kinetics that arise from the high activation energy demanded for the ion diffusion in the solid lattice.[74] A decrease in particle size causes the lowering of the activation energy barrier, allowing for fast transformations in NPs (Figure 1.2).[75] Accordingly, new material compositions have been prepared in thin film and NP form using cation exchange reactions. Specifically, there are reports of ZnS films being cation exchanged to yield materials including SnS, CuS and Bi_2S_3[76] and even very interesting ternary compositions like $CuInS_2$,[77] which is widely desired for applications in photovoltaic cells. Also, binary cadmium sulfide and selenide NPs have been transformed by cation exchange with solutions containing Ag^+ or Cu^+.[74, 75]

Recently, our group has extended the cation exchange reaction previously observed in NP solutions to CdSe gels[78] which were easily converted into Ag_2Se, PbSe and CuSe simply by immersing an already gelled CdSe wet gel monolith in the cation solution of choice. The exchange resulted in complete conversion, while the monoliths remained intact.

1.7 Water remediation

The increase in the industrialization level of the world, beneficial in so many ways, also comes with a slew of drawbacks. One of the most prominent and pressing issues is the environmental deterioration that accompanies industrial processes.[79, 80] For example, the heavy metal content in the aquatic ecosystems increases constantly from sources such as domestic wastewater effluents (As, Cr, Cu, Mn and Ni), coal-burning power plants (As, Hg and Se), metallurgy (Cd, Ni, Pb, Mo, Se, and Sb) and the dumping of sewage sludge (As, Mn and Pb).[79] Heavy metal contaminants are especially detrimental to the environment since they do not degrade over time and thus need to be physically removed from the contaminated samples. At the same time as industrial chemical use is rising, so is the demand for clean water. Accordingly, regulatory agencies in Europe and North America are imposing stricter rules for contaminated water discharge levels. Currently, the discharge levels are at parts per billion (ppb) but are expected to be reduced to parts per trillion (ppt) in the very near future, to counteract the overall increase in the pollution sources.

Current methods used for heavy-metal removal from water, such as precipitation as hydrated metal oxides or hydroxides, usually yield large amounts of contaminant-

containing sediments, formed due to flocculation or coagulation.[81] Moreover, even after precipitation, the concentration levels of some heavy metals are well above those considered to be safe and acceptable today (i.e. the Environmental Protection Agency's 15 ppb action level for Pb or the maximum allowed concentration of 2 ppb Hg in drinking water). Ion exchange provides a way to remove all ions of interest from a solution, while at the same time physically separating the contaminant.[81]

Water remediation processes using ion exchange materials are dominated by oxidic inorganic clays[82, 83] or zeolites.[84] These materials have complex compositions that only allow for a limited theoretical cation exchange capacity (i.e. up to 1 mmol of exchangeable cation/g of exchanging material). Also, due to their mostly oxidic framework, they suffer from low binding affinity and selectivity for heavy metals. To improve the exchange capacity and affinity towards heavy metals, new materials have been developed by functionalizing the oxidic materials with softer Lewis-basic thiol groups.[85, 86] The functionalization supplements the ion exchange ability with chemisorption at the surface thiol groups, resulting in improved affinity (up to 2 mmol/g exchanger) and selectivity for mercury, but not so much for other heavy metals. Sulfide-based ion exchange materials should be ideal candidates for heavy-metal remediation applications due to their soft basic frameworks, which should show increased affinity towards soft Lewis acids (heavy metal ions). Surprisingly, there are just a few reports[60, 62, 87-89] on the soft heavy metal exchange properties of metal sulfides (typically layered phases), but they all show improved affinity and capacities. Thus, the soft Lewis base characteristics of mineral sulfides such as FeS_2, results in augmented exchange with soft Lewis acids; (~5 mmol Cd/g exchanger, but only 0.7 mmol Pb/g).[90-92] Because exchange

is limited to the surface, the theoretical exchange capacity (~8 mmol/g) is not realized. A material capable of sequestering the heavy metals via chemical exchange throughout its structure, in a mole-to-mole fashion, should be better suited for remediation of contaminated effluent streams using fixed-bed adsorption technologies.

1.8 Thesis statement

Our research group has extended the use of sol-gel chemistry to semiconducting metal chalcogenide aerogels,[22, 25, 64, 93] thus opening an avenue for applications that require electrical conductivity through the network. The assembly is achieved by the controlled oxidation of thiolate-capped metal chalcogenide NPs, resulting in highly porous 3D architectures that retain the quantum confined properties of the NP building blocks. The porosity of the network is beneficial for applications that require direct accessibility to the NP surface, such as sensing or catalysis. At the same time, the direct connectivity between particles should provide enhanced electrical conductivity and thus be beneficial for applications in PV devices, where the conductivity is limited by interparticle electron hopping.

A key factor impacting electrical transport in the nanostructure is expected to be the chemical nature of the inter-particle interfaces. Accordingly, in the dissertation research, I aimed to uncover the mechanism of metal chalcogenide gel formation by conducting a systematic investigation of the chemical changes occurring in various stages of the gel network formation process. Previous results[94] suggest that the gelation of cadmium selenide particles occurs via an oxidation reaction and the formation of covalent di-selenide bonds bridging the NPs and that a reducing agent is required to break the

bonds holding the network together, thus dispersing the gel. A series of physical and chemical techniques will be used to unequivocally probe the exact nature of the chemical bonds that allow for the NP assembly and also the generality of the process with respect to other metal chalcogenide systems.

In addition to the chemistry of the particle-particle interfaces, chemical composition is also important for tuning parameters relevant to optical absorbance characteristics, charge separation, charge and ion transport. The typical aerogel synthesis involves two distinct processes: NP synthesis and oxidation-induced assembly. Therefore, every new material requires the development of a new set of non-trivial synthesis and optimization protocols for each step, thereby slowing the generation of new compositions. Cation exchange is a well-known chemical process that should allow for simple modifications of chemical compositions of already gelled networks. As previously mentioned, the cation exchange process, even though thermodynamically favored when systems with appropriate solubility constants are used, is impeded in bulk materials by the slow kinetics of cation diffusion through the crystal lattice. In NP systems, the size of the particles is similar to the reaction front size,[95] and the reaction occurs at much faster rates. In the dissertation research, I aimed to use the knowledge we have generated for synthesizing certain metal sulfide gels (i.e. ZnS) and combine it with the easy cation-exchange chemistry previously demonstrated in our group for CdSe gel systems[78] to achieve new binary, ternary and even quaternary sulfide gel materials. Specific phases to be targeted are binaries Ag-S, Pb-S, Cd-S, Cu-S; ternaries $CuInS_2$, and quaternary $CuZnInS_2$. Binary phases were chosen for comparison to previously studied selenides,

whereas the ternary and quaternary phases aim to show the complexity that can be obtained and also generate materials of interest for solar cell applications

Understanding of kinetics and thermodynamics of ion exchange is also relevant to the use of chalcogenide gels for removal of heavy ions from contaminated water sources. The cation exchange process occurring in the soft metal sulfide aerogels, combined with the high porosity and high surface area inherent to aerogels, should allow for increased heavy metal removal capacities when compared to the reported oxidic and even layered sulfide materials, where most of the removal occurs through physisorbtion. Assuming that the cation exchange process will occur in a mole–to–mole ratio, a calculated capacity of 2127 mg Pb/ g ZnS aerogel is predicted. This is almost an order of magnitude higher than the highest capacities reported to date (319 mg/g for a layered sulfide material[88] or 365 mg/g for thiol functionalized oxidic materials[85]). Accordingly, in the last part of the dissertation research I used the cation exchange process to conduct a quantitative analytical study of the ability of ZnS aerogels to remove hazardous heavy metals from aqueous solutions. Heavy metal cations such as Pb^{2+} and Hg^{2+} will be investigated at environmentally relevant concentrations and compositions to determine the suitability of the ZnS aerogel materials to be used as heavy-metal filtering materials.

The thesis statement is summarized in Figure 1.3.

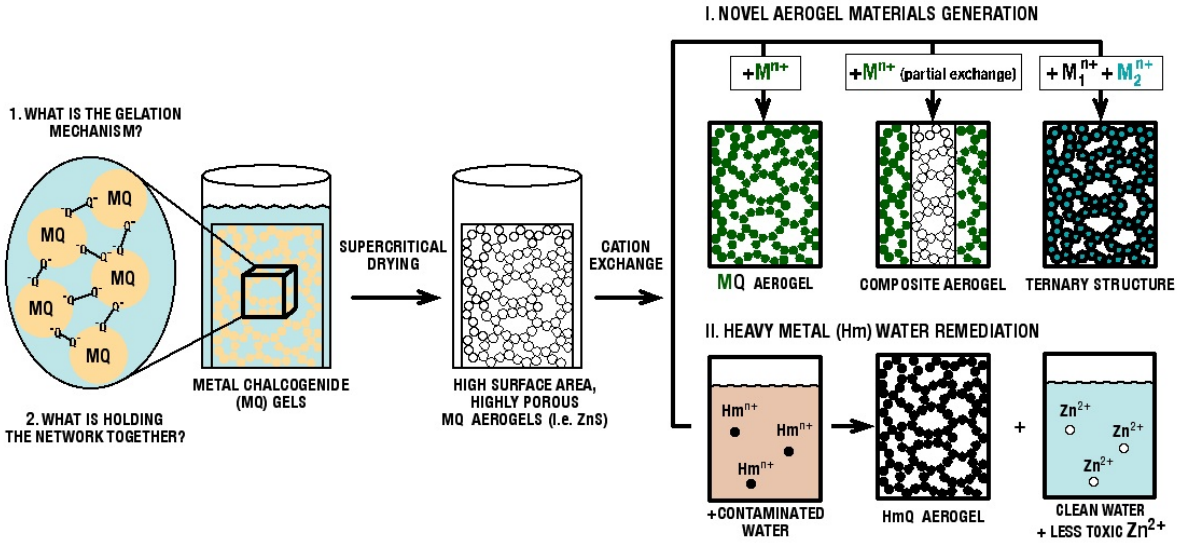

Figure 1.3. Dissertation research thesis statement summary

The dissertation thesis is organized as follows:

- Chapter 2 presents the experimental methods and relevant characterization techniques used;
- Chapter 3 describes the study of the mechanism of metal chalcogenide NP gel formation;
- Chapter 4 discusses the experimental and mechanistic studies of the cation exchange reaction for zinc sulfide gel networks;
- Chapter 5 documents the suitability of ZnS aerogel materials for use as heavy metal remediation materials;
- Chapter 6 summarizes the conclusions drawn and presents a possible direction for future studies.

CHAPTER 2

EXPERIMENTAL AND CHARACTERIZATION TECHNIQUES

Metal chalcogenide aerogels and xerogels are formed by sol-gel assembly of precursor NPs, followed by supercritical or bench top drying, respectively. The NPs and gels are characterized by powder X-ray diffraction, transmission electron microscopy, energy dispersive spectroscopy, X-ray photoelectron spectroscopy, UV-visible absorption spectroscopy, photoluminescence spectroscopy and nitrogen adsorption/desorption surface area analysis. The heavy metal concentrations were measured using inductively coupled plasma mass spectrometry. This chapter will present the materials, synthetic conditions, and characterization techniques used in synthesizing and characterizing the investigated nanomaterials.

2.1 Synthetic Methods

2.1.1 Materials

Bis-(2-ethylhexyl) sulfosuccinate sodium salt (AOT, 96%), cadmium nitrate tetrahydrate (99%), oleylamine (OA), sodium borohydride ($NaBH_4$, 98+%), silver nitrate and triethylamine (TEA, 99%) were purchased from Acros. Trioctylphosphine oxide (TOPO, 90%), cadmium oxide (99.99%), selenium powder (99.5%), trioctylphosphine (TOP, 90%), 11-mercaptoundecanoic acid (MUA, 95%), tetramethylammonium hydroxide pentahydrate (TMAH, 97%), ethylenediamine (99%), acetone, 4-fluorobenzenethiol (FPhSH, 98%), 2-mercaptoethanol (ME) and tetranitromethane (TNM) were purchased from Aldrich. Sodium selenide (metal basis 99.8 %) and n-

tetradecylphosphonic acid (TDPA, 98%) were purchased from Alfa-Aesar. Lead nitrate (99%), cupric nitrate tetrahydrate (99%), ethyl acetate, ethyl ether, 3% aqueous hydrogen peroxide, regent grade methanol, absolute ethanol, butanol, toluene, pyridine and n-heptane were purchased from Fisher. All the chemicals were used without further purification.

2.1.2 Synthesis of Metal Chalcogenide NPs and Gel Networks

2.1.2.1 Synthesis of CdSe NPs using the high temperature route

The synthesis of the CdSe NPs and gels has been accomplished using methods previously developed by our group.[66] In a typical synthesis (Scheme 2.1), highly coordinating surfactant ligands (i.e. TOPO, TOP) are used to generate TOPO-capped CdSe NPs from the reaction of CdO and Se at high temperature (280°C). These NPs are then complexed with thiolate ligands (i.e. MUA); TOPO/TOP capping groups are exchanged and thiolate-capped CdSe NPs are generated. These are then dispersed in methanol to yield an orange-red colored CdSe sol.

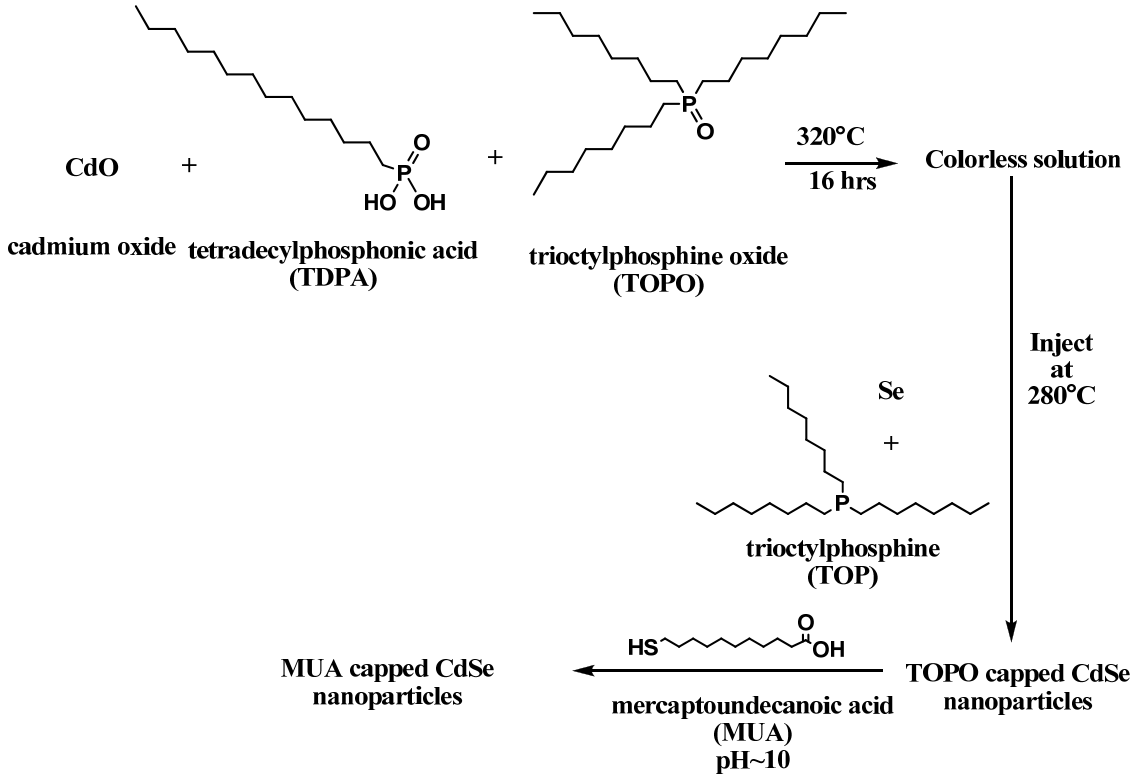

Scheme 2.1. Synthesis of CdSe NPs and gels using the high temperature route

2.1.2.2 Synthesis of ZnS NPs using the room temperature route

Thiolate-capped ZnS NPs were prepared using an established room temperature inverse micellar route optimized by our group.[96] The synthesis involves the use of inverse micelles of aqueous metal ion and chalcogenide precursors in an n-heptane/ sodium bis-(2-ethylhexyl) sulfosuccinate (AOT) mix (Scheme 2.2). The water to surfactant ratio (W), which controls the micelle size, can be controlled in order to obtain various sized NPs. The thiolate-capped NPs can subsequently be oxidized to form gels. The method can be extended easily to other metal chalcogenide systems, such as CdS or CdSe.

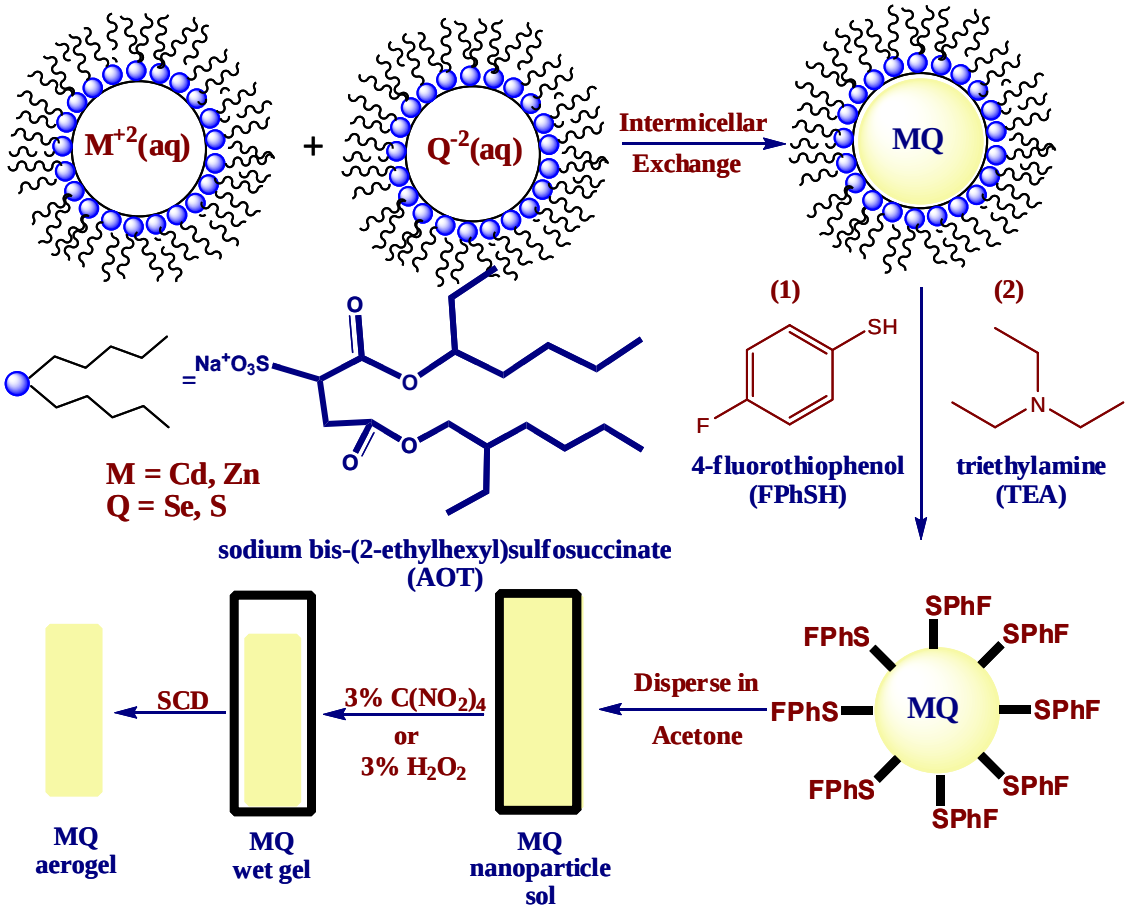

Scheme 2.2. Illustration of MQ (metal chalcogenide) NP and gel formation using the inverse micellar route. This procedure can be used for the syntheses of ZnS, CdS, and CdSe. (SCD= supercritical drying)

2.1.2.3 Formation of 3D NP gel networks

The addition of a chemical oxidizing agent (i.e. tetranitromethane, TNM or hydrogen peroxide, H_2O_2) to the NP sol (obtained from either the high or room temperature synthetic routes) results in the controlled oxidation of the surface-bound thiolate groups, yielding a solvent-swollen polymeric wet gel network within a couple of hours. The wet gels are then aged for two days under ambient conditions to form

monolithic wet gels, and the byproducts of the oxidation process are removed by exchanging the solvent with acetone 4-5 times over 2-3 days.

2.1.3 Supercritical Fluid Drying for Aerogel Formation

The sol-gel synthetic method described above yields metal chalcogenide wet gels consisting of interconnected particles and polar-solvent-filled pores. If the wet gels are allowed to dry on the bench top, under ambient conditions, the capillary forces between the evaporating solvent and the pore walls cause the pores to shrink, drastically reducing the volume of the monolith to less than 10% of the wet gel volume. The materials formed in this way, with a resulting decreased porosity and surface area, are termed xerogels. For applications in which the NP interconnectivity is important, but the porosity and surface area are not, xerogels are preferred.

If preserving the high porosity and surface area present in the wet gels is desired, the drying is achieved using a supercritical fluid. Supercritical fluids exist above a certain critical temperature and pressure (Figure 2.1) and are characterized by the fact that the gas/liquid phase boundary disappears. This creates conditions in which the capillary forces between the fluid and the pore walls are non-existent, allowing for the monolith volume, porosity and surface area to be almost completely maintained during drying. Historically, supercritical alcohols were used to dry the first silica aerogel monoliths, but the pressure and temperature requirements posed safety concerns.[97] CO_2 has a much more user-friendly critical point pressure and temperature and is the fluid used for this dissertation research. The phase diagram of CO_2 is illustrated in Figure 2.1.

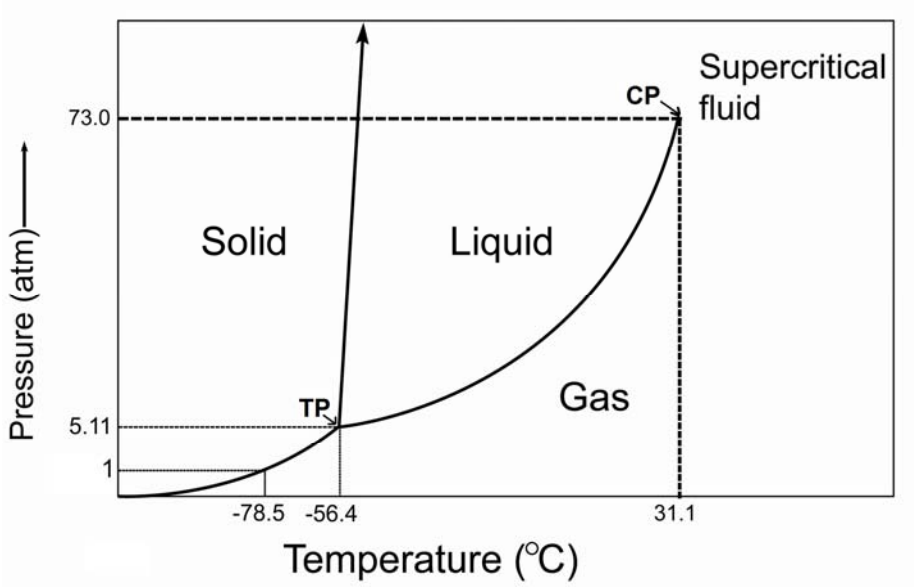

Figure 2.1. CO_2 phase diagram (adapted from Lieu[98]). TP = triple point; CP = critical point

The supercritical CO_2 drying technique has been previously reported[45] for the formation of various aerogels. In the dissertation research, the procedure involves the replacement of the wet gel solvent (i.e. acetone) with liquid CO_2 in the pressurized vessel of a SPI Dry model critical point dryer at 19˚C and 65 atm. The chamber is drained and refilled 3-4 times over a 4 hour period, to ensure that the acetone in the wet gel pores is completely removed and replaced by the liquid CO_2. The temperature is then raised to 39˚C, which causes the pressure to also rise to ~100 atm and the CO_2 to reach the supercritical fluid state. The gel is kept in this environment for one hour, to ensure the complete gas to supercritical fluid conversion. Afterwards, the chamber pressure is vented slowly, while keeping the temperature at 39˚C. The temperature of the drying chamber was controlled using a Fisher Scientific ISOTEMP 10065 water circulator. This drying method ensures that the porosity and high volume of the wet gel are maintained.

2.2 Characterization Techniques

2.2.1 Powder X-Ray Diffraction (PXRD)

X-ray diffraction is a technique that uses the wave-like character of electromagnetic radiation to investigate the structure of solid samples. When a wave interacts with gratings with spacings similar to the wavelength, diffraction occurs. By using X-ray radiation, whose wavelengths are on the order of 1Å, atomic distances in solids, which are of the same order of magnitude, can be probed.[1]

The most common way to produce X-rays for analytical work is to first generate an electron beam by heating up a filament; this electron beam is accelerated and strikes a metal target (copper is most widely used). As illustrated in Figure 2.2, the incident electron beam causes electrons from inner K shells to be removed, and so electronic vacancies are created. Electrons from outer shells can then relax into these vacancies, emitting X-ray photons. The most intense of these radiations is the K_α (corresponding to a transition from the L to K shells), making it the most suitable for use in analytical processes. For Cu metal, the K_α line has a wavelength of 1.54 Å, appropriate for probing angstrom-scale atomic distances.[1]

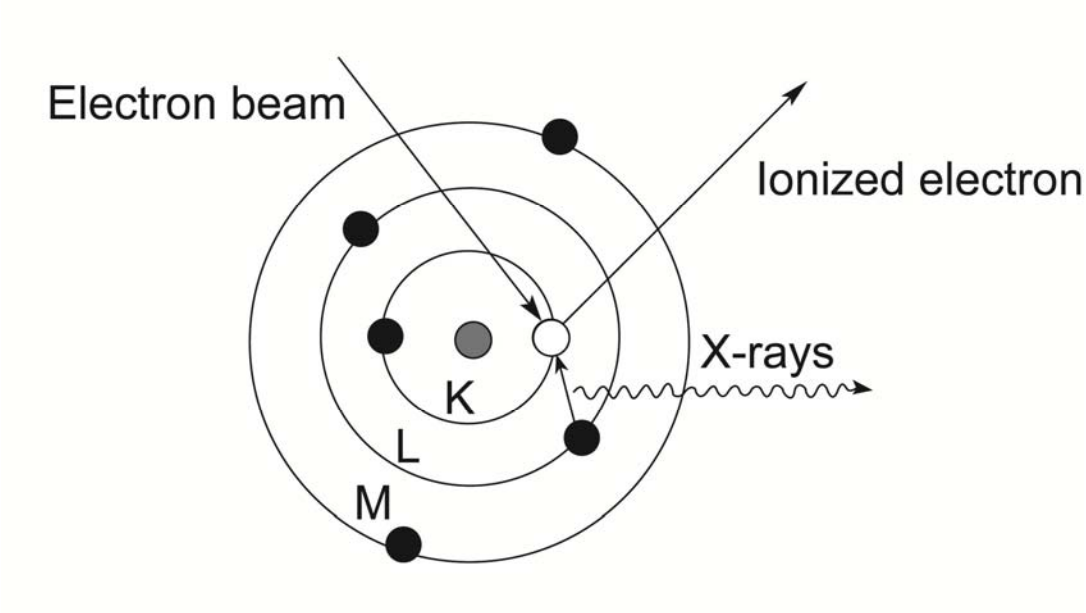

Figure 2.2. Schematic representation of X-ray generation as an electron from the L shell relaxes into the hole created when an electron from the K shell is ionized by an incident electron beam (adapted from West[1])

The interatomic spacing in solids is on the order of 1 Å ; therefore, a crystal can be viewed as a 3D diffraction grating for X-rays. Diffraction maxima can be used in an optical diffraction experiment to calculate the spacing of the lines on the grating; similarly, measuring the separation of the X-ray diffraction maxima from a crystal provides information about the size of the unit cell and the intensities of the diffracted beams correlate to the different arrangement of atoms within the cell.

When an X-ray beam strikes a crystal surface at some angle θ, part of it is scattered by the interaction with the electrons of the atoms in the surface layer. The portion of the beam that is unscattered reaches the second layer of atoms where again a part is scattered (Figure 2.3). When the scattering atoms are distributed in a highly

regular way (crystalline solid) at distances similar to the radiation wavelength, diffraction occurs. The diffracted beams can interfere constructively or destructively.

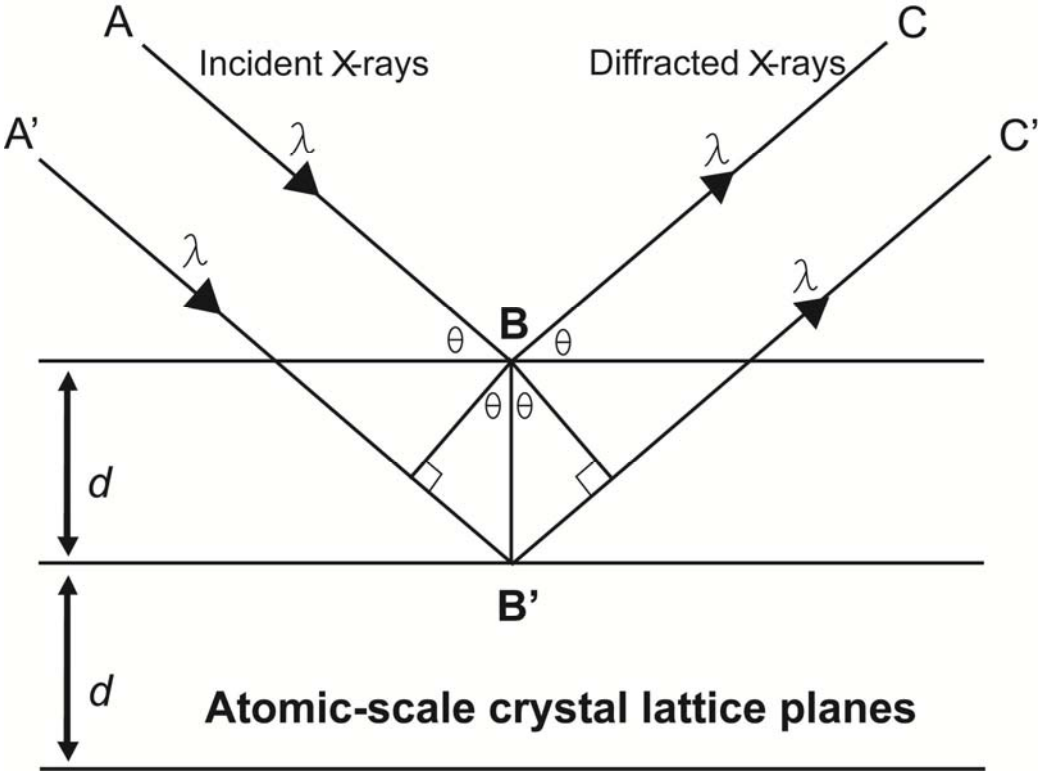

Figure 2.3. Schematic representation of X-ray diffraction by atomic crystal planes and Bragg's law (adapted from Skoog[99])

W. L. Bragg derived the condition for constructive interference to occur from X-rays scattered from a set of parallel lattice planes. Considering the two incident beams shown in Figure 2.3, AB and A'B', scattered by two consecutive atom planes at points B and B', constructive interference will occur when the extra path travelled by the electrons in A'B'C' relative to ABC, equals an integer number multiple of the beam's wavelength, λ. Considering the geometry of the system, this can be expressed as Equation 2.1,

$$2d \sin\theta = n\lambda \qquad \text{(Equation 2.1)}$$

where d is the interatomic plane spacing, θ is the incident angle, and n is an integer. This condition for constructive interference is known as Bragg's law, and it gives the angles at which the diffracted beams can occur.

In powder diffraction, monochromatic X-rays are used to probe a powder sample that contains crystals present in all possible orientations. Thus, all allowed reflections can be identified with no sample rotation. Often, the detector is rotated around the sample and a full diffraction pattern can be obtained by plotting the intensities of different diffraction planes as a function of 2θ. The position of the peak (2θ) is determined by the size and shape of the unit cell; the peak intensity is dependent on the atomic number (i.e. the atomic form factor, proportional to the total number of electrons in an atom) and position of the atoms (the structure factor) in the cell.[1] This results in unique diffraction patterns that are dependent on the crystal structure and material composition, which can be compared with those in crystallographic pattern libraries.

Just as the peak position and intensity provide information about the crystal structure and chemical composition of the sample, the peak broadness can give an indication about the crystallite size. In a bulk material, the presence of a large number of atoms allows the cancellation of partial interferences and results in very sharp diffraction peaks. When the crystal domain size decreases, as is the case in nanomaterials, the limited number of atoms in each orientation causes the broadening of the peaks. The Debye-Scherrer equation (Equation 2.2) relates the width of a peak to the crystallite size t

$$t = 0.9\,\lambda/\beta\cos\theta \qquad \text{(Equation 2.2)}$$

where λ is the incident X-ray wavelength (1.54 Å for Cu K_α radiation), and β is the full width at half maximum (in radians) of the peak at the angle 2θ. This equation can be used

to estimate the NP size, but it should be used with caution, since it makes the assumption that only size effects are responsible for the peak broadening. Other factors, such as defects in the crystal lattice, can also cause peak broadening.

In this dissertation research, a Rigaku RU 200B X-ray diffractometer with a Cu K_α rotating anode source was used for PXRD measurements. Powder samples were affixed to a zero background quartz holder using a small amount of grease. Data were collected in the 20–80˚ 2θ range, using 40 kV voltage and 150 mA current intensity. The diffraction patterns obtained were indexed by comparison to the International Center for Diffraction Data (ICDD) Powder Diffraction File (PDF) database (release 2000). An example of a PXRD pattern for a PbS NP sample is shown in Figure 2.4.

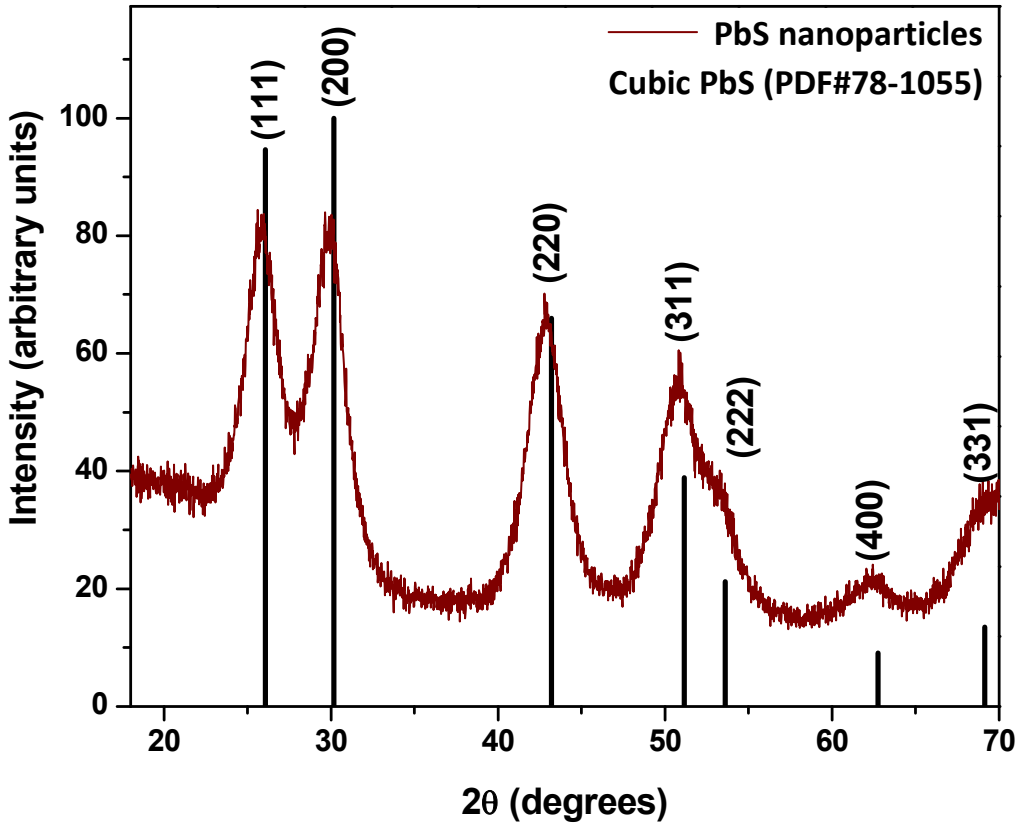

Figure 2.4. PXRD spectra of PbS NPs. The black vertical lines correspond to reflections from the specified (hkl) atomic planes and can be matched with the cubic PbS phase. Using the Debye-Scherrer equation on the (220) peak at $2\theta = 43^{\circ}$, a crystallite size of 10.6 nm can be calculated. The peak broadening is an indication of the small crystallite size

2.2.2 Transmission Electron Microscopy (TEM)

In spectroscopic methods, the sample of interest is irradiated with a primary beam that can be constituted of photons, electrons, ions, or neutral molecules. The interaction of this primary beam with the sample generates a secondary beam, which can also consist

of photons, electrons, ions, or molecules from the sample. The secondary beam does not necessarily consist of the same type of particles as the primary beam. The secondary beam is then analyzed by different detectors, providing information about the sample.

Figure 2.5 illustrates an example of spectroscopy in which the primary beam consists of electrons. Through scattering or emission, secondary beams of electrons or photons are generated that can be analyzed in techniques such as Energy Dispersive Spectroscopy (EDS) or Scanning Electron Microscopy (SEM).

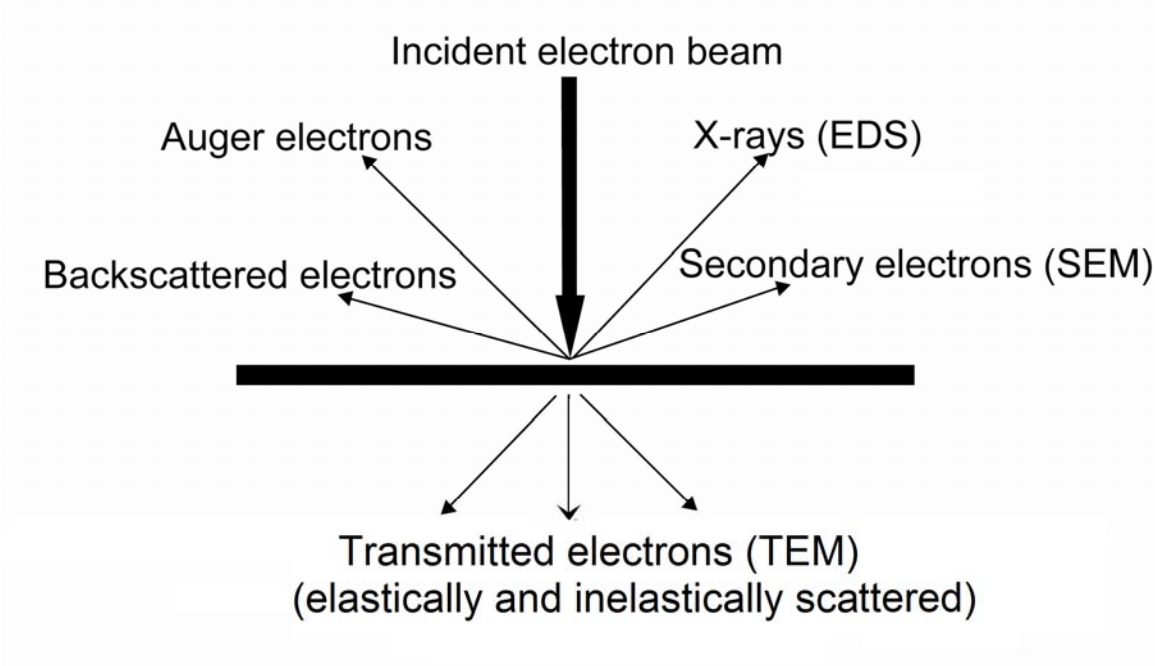

Figure 2.5. Schematic representation of the different processes occurring when an incident beam of electrons interacts with a sample (adapted from Egerton[100])

If the incident electron beam has high enough energy (120–400 keV), and a very thin (250–500 nm) sample is used, after interacting with the sample, some of the inelastically and elastically scattered electrons can tunnel through, and can be imaged on a fluorescent screen positioned on the other side. This is the principle behind

Transmission Electron Microscopy (TEM), which allows the collection of information regarding the sample morphology (size and shape). The advantage in using the wave nature of electrons to image samples, when compared to light in the visible range used in optical microscopy, is that due to wavelengths on the Angstrom scale, electrons can be diffracted by atomic planes, allowing imaging with very high resolution (<1 nm).[100] On the other hand, since electrons are strongly interacting, the sample analysis needs to occur under vacuum, making electron microscopes highly expensive.

For imaging to be possible the transmitted electrons need to be focused; this is achieved by using the fact that electrons are negatively charged particles and so, when moving in a magnetic field, the Lorenz force exerted on the electron can be used to deflect it, effectively acting as a lens that focuses the beam on the screen. There are two basic modes of imaging in TEM: bright field and dark field. A bright field image is collected when an objective aperture centered about the optic axis of the TEM absorbs all the scattered electrons, allowing only the direct beam to pass through the sample. The parts of the field of view that contain no or less sample form from electrons that are not scattered, and so they appear brighter than the specimen, hence the name, bright field imaging. In dark field imaging, the objective aperture is displaced horizontally to block the central undiffracted beam of electrons and, in turn, allow a diffracted beam to be transmitted. This is usually achieved by tilting the illumination beam and using the aperture to select the desired Bragg reflection. In this imaging mode, the strongly diffracting regions appear bright, while the parts that contain no diffracting specimen are dark.[99, 100]

In the dissertation study, TEM analyses were conducted in the bright field mode using a JOEL FasTEM 2010 HR analytical electron microscope operating at an accelerating voltage of 200 kV. Samples were prepared by adding a drop of the NP solution or aerogel that was sonicated in acetone to a carbon-coated copper or nickel TEM grid. The samples were allowed to dry under ambient conditions before analysis. As an example, TEM images of a CdSe aerogel (Figure 2.6) show that the material consists of an interconnected network of almost spherical CdSe NPs. Meso- (2-50 nm) and macro (>50 nm)-pores with a wide range of diameters can be observed throughout.

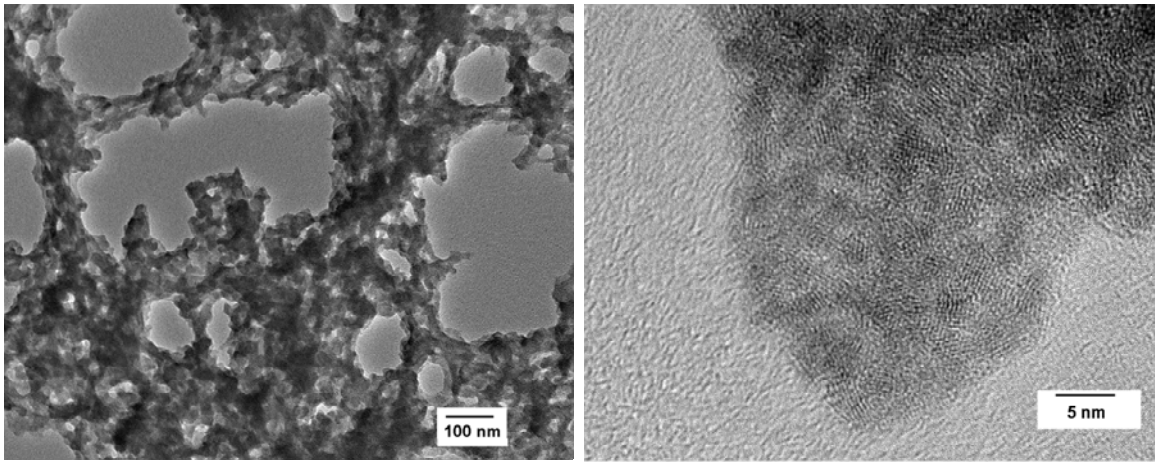

Figure 2.6. TEM images of a CdSe aerogel obtained using bright field imaging. The dark features are a result of the electron beam being blocked by the sample, while the light areas are pores, where the electrons were transmitted through to the detector. Left image: Overall gel morphology showing macro- and mesopores; Right image: High resolution TEM (500,000 x magnification) showing individual CdSe NPs (lattice fringes —resulting from phase contrast imaging of ordered crystalline planes— are visible)

2.2.3 Energy Dispersive Spectroscopy (EDS)

EDS analyzes the X-rays generated by the interaction of an incident beam of electrons with the sample surface. The X-ray generation occurs through the same process illustrated in Figure 2.2, when an electron from an inner shell is ionized through the interaction with an incoming beam of electrons, leaving behind a vacancy that is filled by an electron from an outer shell. Due to characteristic electrostatic interactions, these transitions occur at energies that are specific for each atom, allowing them to be identified. EDS detectors operate at liquid nitrogen temperature and measure the energy of the emitted X-rays, allowing for the determination of the elements present in the sample. The atomic ratios of the elements can also be calculated by comparing the peak areas of the different elements. The technique is more sensitive to heavier elements (atomic number $Z>11$), due to the high background noise inherent in the low energy region. Usually, EDS detectors are coupled with another instrument, such as TEM or SEM. With its higher accelerating voltage, TEM/EDS is capable of detecting K-shell X-rays of more elements than SEM/EDS.

In the dissertation study, the EDS unit (EDAX, Inc.) attached to the TEM instrument described in Section 2.2.2 was used for the determination of elemental composition of NPs and aerogel samples. The sample preparation is the same as that used for the TEM grids. The data collected was analyzed using the EDAX Genesis software.

2.2.4 X-ray Photoelectron Spectroscopy (XPS)

XPS is a surface analysis technique that uses high energy X-ray photons to probe the chemical composition and oxidation state of materials in gaseous, solid and liquid

state.[99] Usually, a magnesium or aluminum target is used to generate an X-ray beam which, upon impinging on the surface of the sample, ejects electrons from different electronic levels. The physical process involved in XPS is schematically represented in Figure 2.7. In principle, a photon of a monochromatic X-ray beam of known energy $h\nu$ displaces an electron e^- from an orbital. The reaction can be represented as

$$A + h\nu \rightarrow A^{+*} + e^-$$

where A is an atom, molecule or ion and A^{+*} is an excited species with a charge one higher than A.

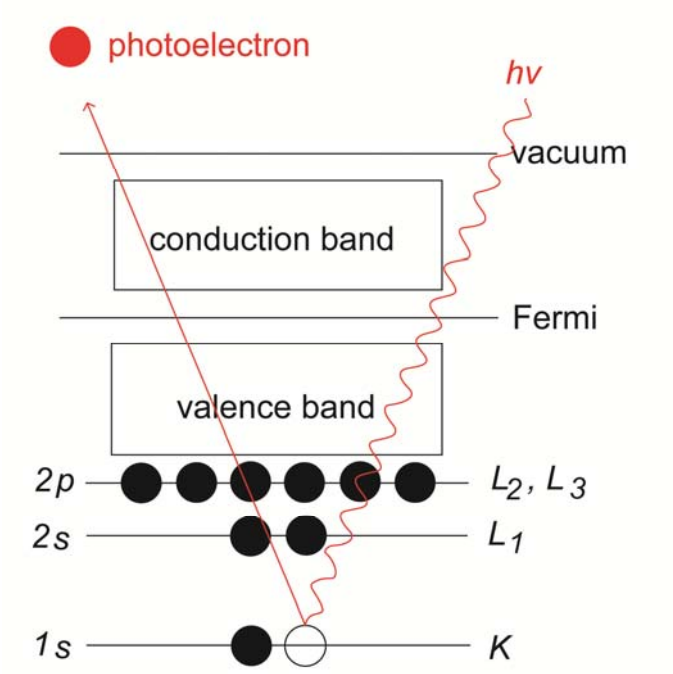

Figure 2.7. Schematic representation of the XPS process (adapted from Skoog[99])

The detector is measuring the kinetic energy *KE* of the ejected electron. For a known value of the incoming photon's energy, the binding energy *BE* of the emitted electron can be calculated by using Equation 2.3

$$BE = h\nu - KE - W \qquad \text{(Equation 2.3)}$$

where W is the work function of the spectrometer, which corrects for the conditions under which the generation of the electron and the measurement take place. The binding energy of the electron is characteristic of the atom and orbital from which the electron was emitted. Using a magnesium or aluminum K_α source, all elements except hydrogen and helium emit core electrons, and the chemical composition of the sample surface can be identified because the binding energies are characteristic of the elements probed. Even though the incident beam of high energy photons has a high penetration depth (about 10^4 Å), the photoelectrons produced can not pass through more than a few to 50 Å, making XPS a true surface analysis technique.

Besides providing qualitative data about the chemical identity of the atoms on the sample surface, the binding energy is also sensitive to the chemical environment of the atom. For example, if the number of valence electrons and the type of bonds they form vary, this influences the binding energy of the core electrons. Consequently, a change in the oxidation state of the probed atom results in a change in the binding energy peak position. This chemical shift manifests itself through higher binding energies corresponding to more positive atom oxidation states, since, as electrons in the outer shells are removed as the atom gets oxidized, the core electrons are attracted more strongly by the nucleus, and thus they feel a higher binding energy.

In this dissertation study, XPS was performed using a PerkinElmer PHI 5500 with a monochromatic Al K_α X-ray radiation source (1486.6 eV) and an Auger-Scan system control (RBD Enterprises, Bend, OR). The samples to be analyzed were pressed onto a piece of conducting indium foil, to avoid surface charging. The binding energy scales

were adjusted using the C (1s) peak of graphite at 284.6 eV. The peak positions were obtained by fitting each of the peaks using a Gaussian/Lorentzian curve fitting program provided by the RBD analysis software. A typical survey spectrum obtained from a MUA-capped CdSe NP sample is shown in Figure 2.8.

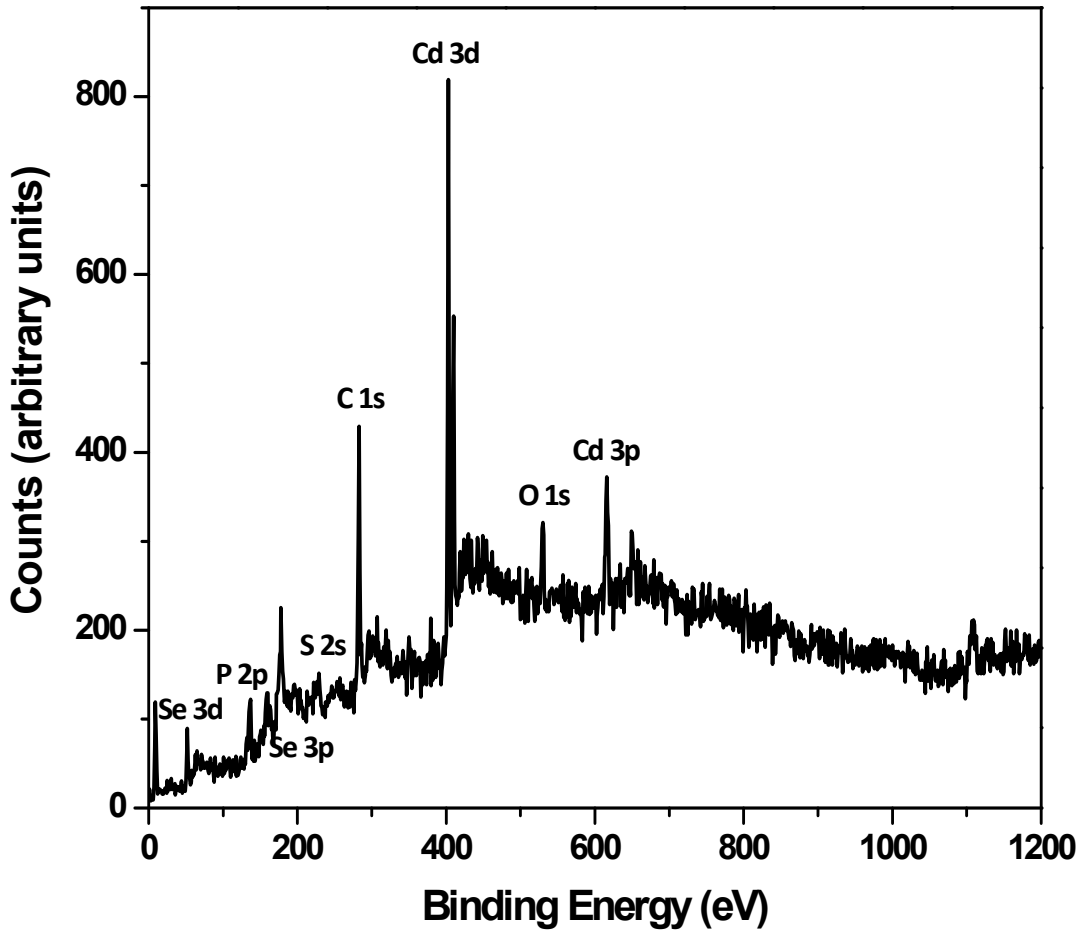

Figure 2.8. XPS survey spectra of MUA capped CdSe NC precursors showing the presence of Cd, Se, S and P from the NPs and C and O from NP surfaces and from adsorbed gaseous molecules

2.2.5 UV-Visible Absorption Spectroscopy (UV-vis)

UV- visible absorption spectroscopy is a technique used to characterize the optical properties of materials interacting with electromagnetic radiation with wavelengths within the 200–800 nm range. When light with energy in this range interacts with absorbing samples, electronic transitions between allowed states can occur. During these transitions from a lower to a higher energy level, energy is absorbed, and the sample appears colored and exhibits an absorption band in the UV-vis spectrum. Materials in which these transitions occur are said to be, or contain, chromophores. In UV-vis, the absorbance A or transmittance T of solutions contained in transparent cells of path length *b* cm is measured. Within certain limits, the concentration *c* of an absorbing species is linearly related to the absorbance, as illustrated by Beer's law (Equation 2.4)

$$A = \varepsilon bc \qquad \text{(Equation 2.4)}$$

where ε is the molar absorptivity coefficient of the species, and is characteristic for the absorbing material.

In semiconducting materials, an electron from the conduction band can absorb a photon with energy equal to or greater than the band gap energy, and be promoted into the conduction band. This gives rise to an absorption edge. In the case of semiconducting quantum dots, the bandgap is very sensitive to the particle size, due to the quantum confinement effect (Chapter 1, Section 1.1). Basically, as the particle size decreases, the bandgap increases. This phenomenon translates to a shift in the position of the absorption edge: as the particle size decreases, the absorption edge (and peak) position shift to higher energy (blue shift). The dependence of the NP bandgap energy E(R) with the

decrease in optical chromophore size R can be described using the mass approximation model proposed by Steigerwald and Brus,[3] and can be expressed as Equation 2.5

$$E(R) = E_g + (\hbar^2\pi^2/ 2R^2) (m_e^{-1} + m_h^{-1}) - (1.8e^2 / \varepsilon R) \qquad \text{(Equation 2.5)}$$

where E_g is the bulk badgap energy; $\hbar = h/ 2\pi$, where h is Plank's constant; m_e and m_h are the electron and hole effective masses, respectively; e is the charge of the electron; and ε is the optical dielectric coefficient of the bulk material.

In this research, UV-vis spectroscopy was used to determine the optical bandgap and chromophore size of semiconducting metal chalcogenide NPs. Optical absorption measurements of NPs were obtained using a Hewlett-Packard (HP) 8453 spectrophotometer. The NPs were dispersed in an appropriate solvent (i.e. acetone, methanol, toluene, depending on the capping agent polarity) and the solutions were analyzed in the region from 200–800 nm. The bangap of the NPs was calculated by converting the absorption band onset wavelength value into energy. This value was then used in the mass approximation model to calculate the optical chromophore size.

For example, for the absorption onset observed in Figure 2.9 (547 nm), the corresponding band gap value is 2.25 eV (bulk CdSe band gap is 1.73 eV) and the calculated chromophore size is 4.7 nm. This is consistent with the widening of the band gap of semiconducting NPs due to quantum confinement effects.

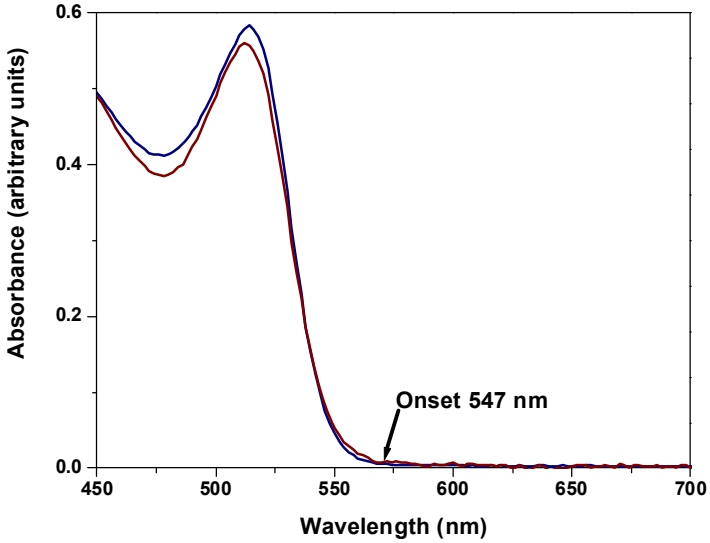

Figure 2.9. UV-Vis spectrum of TOPO- (blue) and MUA-capped (red) CdSe NPs, synthesized using the high temperature method

2.2.6 Photoluminescence Spectroscopy (PL)

After an energy absorbance event, the absorbing species (i.e. an electron) can relax back to a lower energy level by emitting energy in the form of light. This process is called photoluminescence and it is widely used to study the optical properties of semiconducting materials. A schematic illustration of some of the radiative transitions possible for electronic relaxations is represented in Figure 2.10. Fluorescence occurs when relaxation occurs from an excited singlet state (S_1, S_2 or S_3 in Figure 2.10) to the ground singlet state. This is an allowed transition and it has a high occurrence probability, and thus high signal intensity. Usually the emission occurs at a lower energy than that of the absorbed light, the difference being accounted for by vibrational relaxations. This shift towards lower energies is termed the Stokes shift. Fluorescence has a short lifetime

(10^{-9}–10^{-7} s). The excited electron can reverse its spin in a process called intersystem crossing, and populate an excited triplet state energy level, which is lower in energy than the excited singlet states. This process has a higher probability to occur if the vibrational levels of the singlet and triplet states overlap. When the light is emitted upon relaxation between an excited triplet state and the ground singlet state, another radiative process called phosphorescence occurs. The probability of this process occurring is lower than for the fluorescence, but it has a longer lifetime (10^{-3}–10^{2} s).

As previously mentioned, semiconducting NPs can absorb light with energy equal to or higher than that of the band gap, causing an electron from the valence band to be promoted into the conduction band. Upon relaxation, energy can be emitted as light. The quantum confinement effect present in semiconducting NPs can be observed in PL spectra, too, and it is expressed through the same peak shift to higher energies as the particle size decreases, as is observed in UV-vis spectroscopy. The Stokes shift is also observed. The presence of dopants, impurities or defects can cause electron or hole trap states, which in turn can generate emissive radiation occuring at energies much lower than the band gap energy.

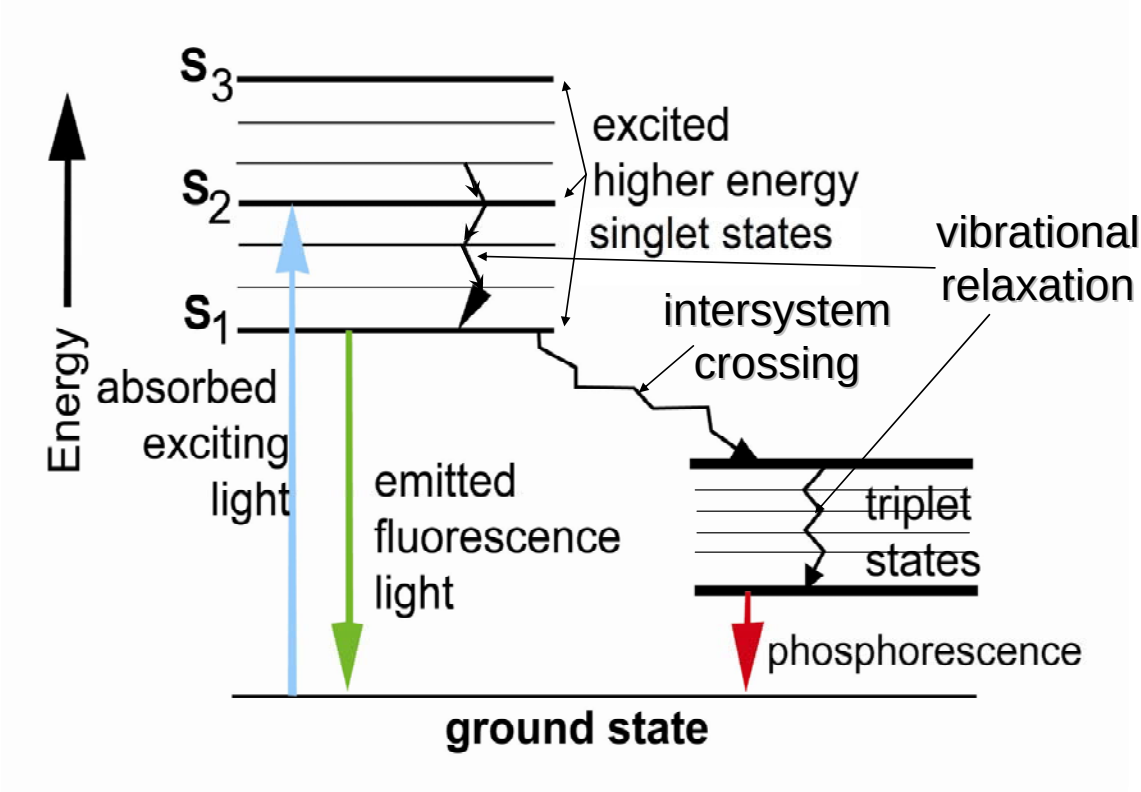

Figure 2.10. Schematic representation of the radiative transitions probed by PL spectroscopy (adapted from Skoog[99])

In the dissertation research, a Cary Eclipse (Varian, Inc.) fluorescence spectrometer was used to study the emission properties of the metal chalcogenide NPs. NPs were dispersed in appropriate solvents (toluene for TOPO-capped and methanol for MUA-capped NPs) and a 1 cm quartz fluorescence cuvette was used to collect spectra.

Emission properties of TOPO and MUA- capped CdSe NPs were investigated using photoluminescence spectroscopy (PL). The NPs exhibit a band-edge emission at 545 nm and a broad trap state emission in the form of a broad double-hump extending from 625 to 800 nm (Figure 2.11). The trap state emission is due to the presence of the

thiolate capping groups, which are known to act as hole acceptors, effectively reducing the band-edge luminescence.

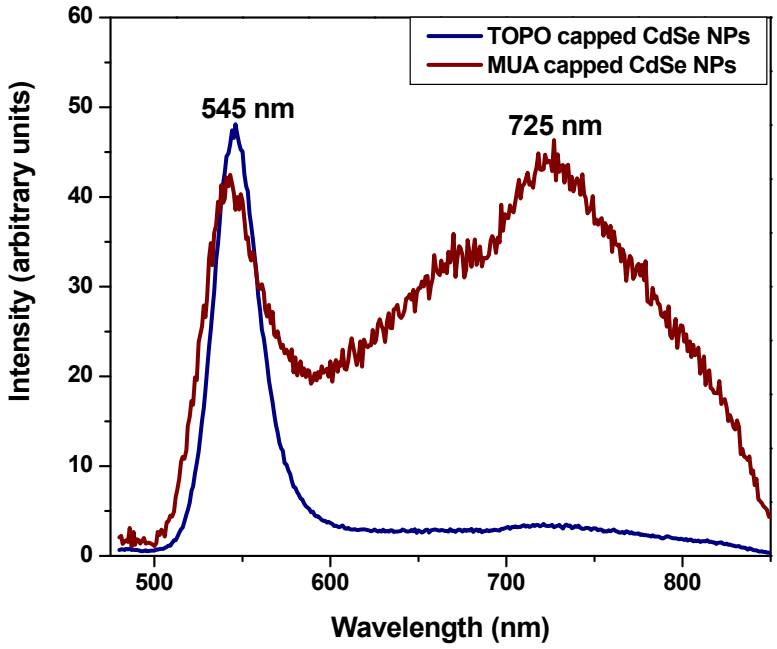

Figure 2.11. PL spectrum of TOPO- and MUA-capped CdSe NPs; the broad, red-shifted peak at 725 nm is due to hole-trapping by thiolate molecules

2.2.7 Surface Area and Porosimetry Analysis

Due to their small particle size, nanomaterials have a surface-to-volume ratio that is much larger when compared to bulk materials. The surfaces of any material have physical and chemical properties that differ from those on the interior, due to the fact that they are bound only on one side to inner atoms, leaving uncompensated atomic forces at the surface. Surface atoms usually show enhanced reactivity and thus have become the focus of numerous studies and applications such as in catalytic or sensing materials. When high surface area particles are assembled in highly porous structures, as is the case

of aerogel materials, an enhancement of the aforementioned properties is expected. To better understand the influence of such properties upon the activity of the studied materials, the surface area and porosity have to be quantified.

One of the most popular methods used for the determination of surface area and pore volume, size and structure uses the adsorption/desorption of gases on the surface and in the pores of a dry solid.[101] The "dangling bonds" intrinsic to surface atoms interact with gas molecules (adsorbates), attracting them to the surface (adsorbent). This interaction can occur via weak van der Waals forces, in which case the process is called physisorption. If the adsorbent and adsorbate participate in electron sharing, chemical bonds are formed and the process is called chemisorption. Different materials interact differently with the same gas and different gases may interact differently with the same material. By studying the behavior of the material upon adsorption/desorption of a gas under controlled conditions, information about the surface area and the porosity of the material can be extracted.[102]

In a typical gas sorption experiment, the sample surface is first cleaned of adsorbed gases, water or oil molecules, by heating it under vacuum or under the flow of an inert gas. Once the sample is dry, it is weighed and loaded into a closed glass tube, held at liquid nitrogen (77K) temperature. An inert gas, such as N_2 or He, is then introduced in small increments into the sample tube. As the gas is adsorbed on the surface of the sample, the sample mass increases and the gas pressure decreases. Once the sample is saturated, the gas pressure in the sample tube reaches equilibrium. The quantity of gas adsorbed can be calculated using the gas laws, since the temperature is constant and the

sample tube volume is known. The data are then fitted using gas adsorbtion models and the surface area for the sample can be extracted in units of square meters per gram.[101]

At constant temperature, the quantity of gas adsorbed by a sample is proportional to the mass of the sample, the pressure of the gas, the temperature, and the nature of the gas and solid. For a given gas adsorbed on a particular solid, the dependence of the quantity of gas adsorbed on these parameters can be expressed as

$$n = f\,(p/p_0)_{\,T,\,\text{gas, solid}}$$

where n is the quantity of gas adsorbed, and p/p_0 is the relative pressure, with p being the equilibrium and p_0 the saturation pressure of the gas. Adsorption isotherms are constructed by graphing the quantity of gas adsorbed as a function of the gas pressure.[102] Typically, both adsorption and desorption isotherms are measured. The shape of an adsorption/desorption isotherm depends on the type of material and the nature of the adsorption process that occurs in the sample. According to classical adsorption theory,[101] as gas molecules are introduced under incremental pressure to the surface of a clean, cold material, they would first form a monolayer on the surface before beginning a second layer. Multilayer formation occurs next, followed by capillary condensation. Depending on the porosity and pore structure of the material, a combination of these processes can occur. At low relative pressures, gas molecules form a monolayer on the sample surface and fill micropores (pores with diameters less than 2 nm). As the pressure is increased further, multilayers start to form, filling mesopores (2–50 nm) and macropores (> 50 nm). When the saturation pressure of the gas is neared, capillary condensation occurs, as the gas molecules condense into a liquid.

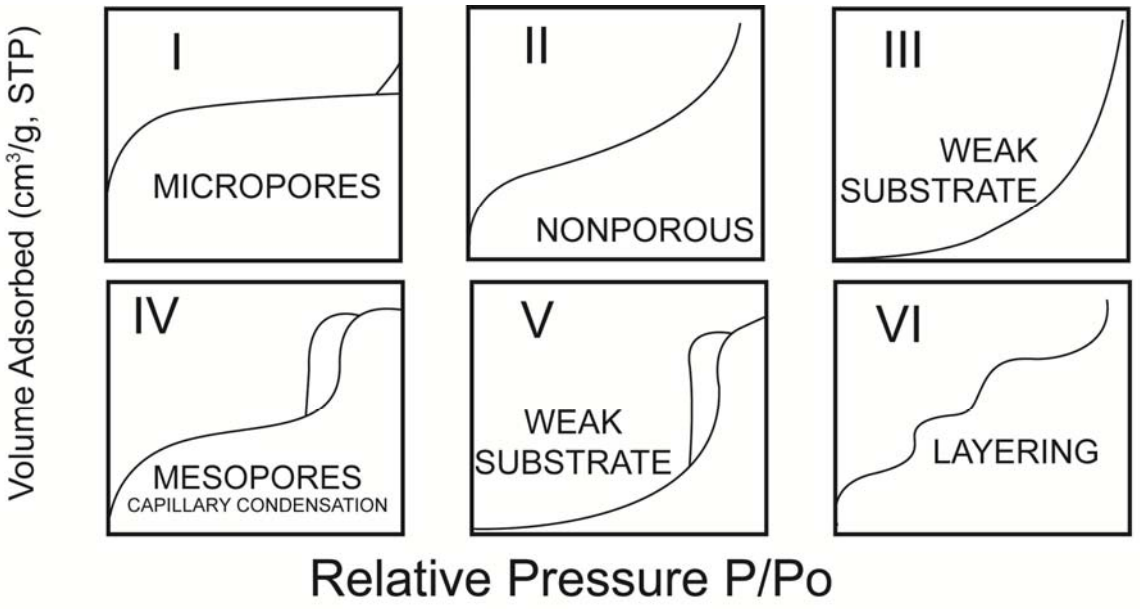

Figure 2.12. The basic types of adsorption/desorption isotherms (adapted from Gregg)[102]

Figure 2.12 illustrates the six different types of adsorption isotherms that can be observed in a gas sorption experiment, as given by the Brunauer, Emmett and Teller (BET) classification. The type of pore or interaction that would exhibit each isotherm shape is also indicated. The hysteresis loops observed in the Type IV and V isotherms are characteristic of mesoporous materials, and occur due to the different behavior of the sample as it is being filled or emptied. The lower branch represents the adsorption process and the upper branch, the desorption. The hystereses may have different shapes, depending on the pore structure and pore shape (cylinder, slit-shape or ink bottle).

Since materials may have pores in a range of sizes, isotherm shapes can vary greatly and they need to be examined in detail to extract information about the surface area and the pore structure. Accordingly, thermodynamic and other principles have been used to construct different theoretical models for the interpretation of the adsorption/desorption data. For the measurement of surface area, two of the most used

models are the Langmuir model (which describes chemisorption), and the BET model (used for physisorption processes). The Langmuir model assumes that adsorption only occurs through monolayer formation. The BET model generalizes the Langmuir theory by considering the formation of multiple layers as a result of the same attractive forces that are responsible for the condensation of gases.[101] The BET model is thus more suitable for analyzing surface area in mesoporous materials. The BET model is applied to the low relative pressure region of the adsorption isotherm (monolayer coverage). By equating the rate of condensation of gas molecules onto an already adsorbed layer to the rate of the evaporation from that layer, the BET equation can be generated (Equation 2.6)

$$\frac{P}{V_a(P_0-P)} = \frac{1}{V_mC} + \frac{C-1}{V_mC}\frac{P}{P_0} \qquad \text{(Equation 2.6)}$$

In this equation, P and P_0 are the equilibrium and saturation pressure of the adsorbtive gas; V_a is the quantity of gas adsorbed at pressure P; V_m is the quantity of gas adsorbed when one monolayer is formed; and C is a constant. If the adsorption process can be described using the BET model, a plot of $P/[V_a(P_0-P)]$ *vs.* P/P_0 should yield a straight line, with intercept $1/V_mC$ and slope $(C-1)/V_mC$. From the straight line regression, the values of V_m and C can then be extracted. From the volume of the monolayer V_m, the surface area of the sample can be determined using an approximate surface area for one gas molecule (i.e. 16.2 $Å^2$ for a N_2 molecule).[101]

For the determination of information related to the porosity of the sample (i.e. pore size, pore size distribution, cumulative pore volume), the adsorbtion/desorption isotherms can be modeled using a variety of theories, including that of Barrett, Joyner, and Halenda (BJH) which is directly relevant to the dissertation research.[101] The BJH

model usually assumes pores with a cylindrical shape. The BJH model uses the Kelvin equation to correlate the pore size with the critical condensation pressure of the adsorbed gas, therefore allowing the characterization of the mesopore size distribution of the adsorbent. The Kelvin equation is usually written as Equation 2.7

$$\ln(P^*/P_0) = -(2\gamma\upsilon\cos\theta/RTr_m) \qquad \text{(Equation 2.7)}$$

where P^* and P_0 are the critical condensation and the saturation pressure; γ is the liquid surface tension; υ is the molar volume of the condensed gas; θ is the contact angle between the solid and the condensed phase (assumed to be zero when nitrogen is used, so $\cos\theta = 1$); r_m is the mean radius of curvature of the liquid meniscus; R is the ideal gas constant; and T is the absolute temperature.[101] Considering the fact that pore filling or emptying occurs in a stepwise manner, the BJH model uses the Kelvin equation to compute the pore radius distribution. Once the radii of the pores are known, the assumption of cylindrical geometry is used to calculate the total length of the cylinder. This allows for the calculation of the cumulative pore volume of the sample.[101]

In this dissertation research, a Micromeritics Tristar II surface area and porosimetry analyzer was used to obtain nitrogen adsorption/desorption isotherms at 77K for aerogel samples. The surface area was calculated using the BET model. The pore-size distribution plot, the average pore diameter and cumulative pore volume were determined using the BJH model. Aerogel samples were degassed at 110˚C under flowing Ar for 24 hours before analysis.

2.2.8 Inductively-Coupled Plasma Mass Spectrometry (ICPMS)

ICPMS is a popular technique for elemental analysis, due to its low detection limits (parts per billion for most elements), high selectivity, and good precision and accuracy.[99] The technique involves the use of an ICP torch as an atomizer and ionizer, coupled to a quadrupole mass spectrometer, which separates the generated ions based on isotopic mass to charge ratios. The number of ions of each type is then measured by an appropriate transducer, and a spectra consisting of a simple series of isotope peaks for each element present is generated. For quantitative measurements, calibration curves need to be constructed by using standard solutions of known concentrations of the element of interest. ICPMS is used for the identification and quantification of positive metal ions; one of the advantages of the technique includes the fact that multiple analytes can be measured simultaneously.

In this dissertation research, a Perkin-Elmer Life Sciences Elan 9000 instrument equipped with an automatic sampler was used for the determination of heavy metal concentrations. The data were collected as counts per second. A standard external calibration curve was constructed by diluting stock solutions of 1000 ppm standards (High-Purity Standards) with 2% HNO_3 in HPLC grade water. Samples were prepared by similarly diluting the collected solutions to parts per billion levels.

CHAPTER 3

UNCOVERING THE MECHANISM OF METAL CHALCOGENIDE GEL FORMATION

3.1 Introduction

For biological applications, CdSe and other NPs must be soluble in polar media. This property is usually attained by attaching a monolayer of polar, usually carboxylate-terminated, thiolates on the surface of the NPs.[103] The stability of such thiolate-capped CdSe NPs is usually poor, due to photo-oxidation of the thiolate ligands to form disulfides, a process that is mediated by the semiconducting NPs. In 2001, Peng et al.[104] reported on the oxidation of thiolate capped CdSe NPs in the presence of atmospheric oxygen, resulting in aggregation and precipitation. At the same time, they observed that when excess thiols/thiolates are present in solution, the aggregates could be dispersed, therefore extending the stability of the sol. They hypothesized that the presence of ligands was key to ensuring a stable sol.

Our group has used this oxidative removal of surface thiolates as a way to link particles together into 3D architectures, in which metal chalcogenide NPs are assembled into porous network structures. Gacoin et al.[24, 26, 63, 105] have reported on the formation of similar structures between CdS NPs and on the fact that the interparticle bonding is not mediated by any organic linker. In order to probe the nature of the interparticle bonding in metal chalcogenide gels, metal chalcogenide NPs and gels were synthesized and dispersion studies using various reagents were conducted.

Regarding the nature of the interparticle bonding in forming the gel network, previous work done in our group[94] shows the following:

- CdSe wet gels, aerogels and xerogels can be dispersed upon treatment with a basic solution of mercaptoundecanoic acid (MUA) in methanol (pH=12, adjusted using solid tetramethylammonium hydroxide – TMAH);
- Treatment of the dispersed sols with an oxidant (hydrogen peroxide–H_2O_2 or tetranitromethane–TNM) leads to the re-formation of the gel ;
- Treatment with bases such as pyridine does not lead to gel dissolution, suggesting that a ligating agent is insufficient to promote dispersion;
- Raman analysis of the room temperature-synthesized NPs shows the appearance of a peak at 258 cm^{-1} in the aerogel and xerogel, which is not present in the pre-gelled NPs; this has been attributed to the presence of Se–Se bonds in the 3D structures.

Based on the prior study, it was hypothesized that surface Se^{2-} was being oxidized to form amorphous Se_n^{2-} species acting to link the particles together. To test this hypothesis, I investigated the surface speciation of the aerogel networks using XPS and conducted a more detailed investigation of the gel dispersion process, to be able to distinguish between ligation and reduction.

3.2 Experimental

All the chemicals used in this chapter are listed in Chapter 2, Section 2.1.

3.2.1 Synthesis of CdSe NPs and gels

Colloidal CdSe NPs were prepared by both an inverse micellar [24, 26, 63] and a high temperature synthetic route[33] using highly coordinating surfactant ligands (Chapter 2, Section 2.1.2). Surfactant ligands were exchanged with FPhSH (inverse micellar route) or MUA (high temperature route) as reported in the literature.[66, 104] Colloidal CdSe wet gels were prepared by oxidative aggregation of the thiolate capped CdSe NPs using a methanolic TNM solution as the oxidizing agent.[66] The resulting CdSe wet gels were transformed into monolithic aerogels and xerogels by CO_2 supercritical drying and bench top drying, respectively.

3.2.2 Synthesis of CdS NPs and gels

CdS NPs were synthesized using a slightly modified procedure, adapted from Bawendi et al.[106] In a typical synthesis, CdO (0.2 mmol), TOPO (4g, distilled and recrystallized from acetonitrile) and TDPA (0.05 g, ~0.2 mmol) were heated at 320°C under Ar for 16 hours (until a clear, colorless solution forms). In the meantime, the S precursor is prepared by stirring 0.026 g (0.8 mmol) of S into 8 mL oleylamine at room temperature, under Ar, for 2 hours. Upon the S solvation into the oleylamine, the color changes to orange. The reaction mixture temperature is then decreased to 250°C, and 2 mL of the S precursor solution is injected. The color changes to yellow immediately; the particles are grown at 250°C for 30 min. The NPs are then dispersed in a minimum amount of hexane, and precipitated using a butanol/methanol mixture. After isolation, a ligand exchange is performed by stirring the NPs for 5 hours in a MUA-methanol solution (0.3 g MUA in 15 mL methanol), adjusted to pH ~10.5 using TMAH. The

MUA-capped NPs are precipitated using an ethyl acetate/toluene mixture, centrifuged, washed with ethyl acetate and finally dispersed with 4 mL methanol. Gelation is achieved by adding 0.05 mL 3% TNM to each vial containing 4 mL CdS sol.

3.2.3 Synthesis of ZnS NPs and gels

ZnS NPs were prepared by the inverse micellar synthetic route, as described in Chapter 2, Section 2.2.4.[24, 26, 63] AOT surfactant ligands were exchanged with FPhSH.[66] Colloidal ZnS wet gels were prepared by oxidative aggregation of the thiolate-capped ZnS NPs using a methanolic TNM solution as the oxidizing agent.[66]

3.2.4 Oxidation of Na_2Se by TNM

In a typical reaction, 10 mL of anhydrous methanol, previously degassed and purged with Ar, was added to Na_2Se (0.13g, ~1 mmol). The mixture was stirred under Ar until the dissolution of the salt was complete. To this mixture, 2mL (~0.1 mmol) of 1% methanolic TNM solution (degassed and purged with Ar) was added. After several hours, a black precipitate was observed at the bottom of the flask and was isolated by decantation and washed with methanol.

3.2.5 Dispersion studies

CdSe dispersion studies. Thiolate solutions containing MUA were prepared for the dispersion studies by dissolving 0.1092 g of MUA (0.5 mmol) in methanol (5 mL) and titrating to pH = 12 with TMAH. CdSe or CdS wet gels (corresponding xerogel weight is ~ 0.002 g) prepared from a 4 mL sol of high temperature synthesized NPs were

dispersed in the above solution. Ethyl acetate was added to precipitate the dispersed particles, which were isolated using centrifugation. The resulting NPs were washed two times with ethyl acetate to remove the residual MUA and dispersed in 12 mL of methanol to form a sol. Re-gelation was achieved by adding 0.05 mL of 3 % TNM to 4 mL aliquots of the resultant CdSe or CdS sol. For dispersion studies on aerogels and xerogels, 0.002 g of the CdSe aerogel/xerogel prepared from high temperature synthesized NPs was added to the freshly prepared thiolate solution described above. The resulting dispersed NPs were precipitated and isolated using ethyl acetate as described previously.

ZnS dispersion studies. Dispersion studies of ZnS gels were carried out by adding either 2 mL pyridine, 2 mL ethylenediamine or 0.25 mL of 4-fluorobenzenethiol to wet gels.

$NaBH_4$ dispersion study. 0.04 g (~ 1 mmol) $NaBH_4$ was added to 0.003g (0.02 mmol) CdSe aerogel, in a Schlenk flask. The reaction mixture was evacuated and purged with Ar a few times. 6 mL of absolute ethanol, previously purged with Ar and cooled in an ice bath (~ 4°C) was syringed into the mixture. The flask was then placed in an ice bath and stirred for 8 hours. For the control reaction, the same amounts of CdSe aerogel and ethanol were stirred under the same conditions.

3.2.6 Characterization

UV-Visible Spectroscopy. High temperature synthesized NPs were diluted twenty-fold with methanol and analyzed against a methanol blank in the region from 200 nm to 800 nm. NPs isolated from dispersed gels, aerogels, and xerogels were dissolved in 15 mL of methanol and analyzed against a methanol blank in the same region. The

chromophore size was calculated using the absorption onset value and the effective mass approximation model, as explained in Chapter 2, Section 2.3.6.

Powder X-Ray Diffraction (PXRD). Powdered aerogel/xerogel samples, or NPs isolated from dispersed solutions, were deposited on a low background quartz (0001) holder coated with a thin layer of grease. X-ray diffraction patterns were identified by comparison to phases in the International Centre for Diffraction Data (ICDD) powder diffraction file (PDF) database (release 2000). Crystallite sizes were calculated by employing the modified Scherrer formula (Chapter 2, Section 2.3.1) to the (110) peak of the high-temperature-prepared CdSe NPs (hexagonal) and to the (111), (220) and (311) peaks of the CdS NPs (cubic).

Transmission Electron Microscopy (TEM). NP samples were prepared by depositing a drop of sol onto the grid followed by air evaporation, whereas aerogel samples were prepared on carbon-coated copper grids by dispersing fine powders in acetone using sonication, followed by depositing a drop of solution onto the grid and evaporating the acetone. For precursor NPs and dispersed NP solutions, average particle sizes were manually estimated by measuring the size of ~ 200 individual NPs in several TEM images.

X-ray Photoelectron Spectroscopy (XPS). The samples were prepared by pressing the powder samples on a piece of indium foil prior to measurement. Survey scans were collected over the range from 1200 to 0 eV, with a 117.4 eV pass energy detection and a 1eV/step resolution. Close-up scans were collected over a range of 20-24 eV around the peak of interest with 23.5 eV pass energy detection and a 0.05 eV/step

resolution. Measurements were performed at pressures lower than $2x10^{-9}$ Torr. The binding energy scales were adjusted using the C (1s) peak of graphite at 284.6 eV.

3.3 Results and discussion

If nanomaterial science is to respond to the challenges brought forth by actually integrating the discovery and innovation made in laboratory settings into the real-life device-driven industrial world, it must optimize the way in which NPs are connected into 3D, macroscopic bodies that maintain the characteristic quantum confined properties of the NP building blocks. The sol-gel process used in our lab is a bottom-up approach of accomplishing this goal. At the same time, understanding the chemical nature of the assembly process is paramount to controlling and designing the electrical, optical, magnetic properties of the material. That is the motivation behind the investigation into the nature of the bonds holding together our metal chalcogenide gel networks.

As a result of the previously made observations,[94] a mechanism for the gelation and dispersion of CdSe NPs based on the formation of diselenide was proposed (Scheme 1). During the gelation, oxidation of thiolate leads to the formation of disulfides or sulfonates, producing decomplexed Cd^{2+} ions on the particle surface. The Cd^{2+} ions can be easily solvated by the carboxylate species and/or solvent (methanol is known to bind strongly to binary metal cations[95]), leaving a selenide-rich NP surface. In the presence of excess oxidizing agent, surface selenide groups can oxidize and form diselenide (or polyselenide) species, linking the particles together. Finally, the addition of a reducing agent, such as a thiol, will result in the cleavage of the Se–Se bonds and the liberation of

HSe^- (or a more reduced Se species), forming individual NPs that are again surface-complexed with thiolate ligands.

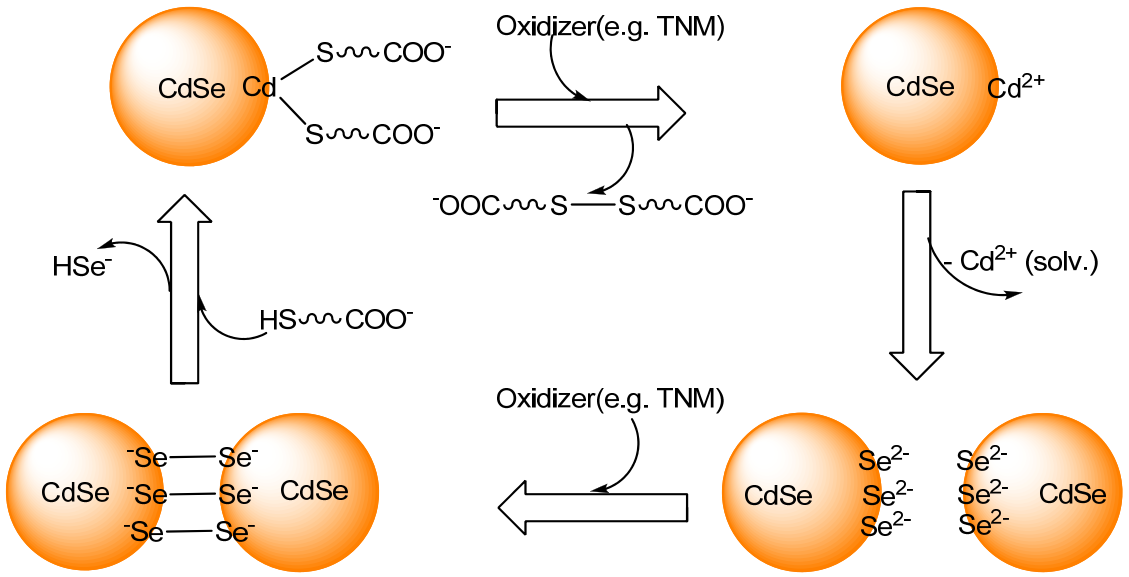

Scheme 3.1. Proposed mechanism of CdSe NP gelation/dispersion

To confirm the formation of Se_n^{2-} in the gelation process, I evaluated the surface speciation of CdSe NPs and aerogels, prepared using the standard high-temperature synthesis route, using X-ray photoelectron spectroscopy (XPS). Typical survey spectra (Figure 2.8) show the presence of Cd, Se, S and P from the NP and C and O from the NP surface and from adsorbed gaseous molecules.

Higher-resolution spectra were taken of the Cd and Se regions of the samples. The Cd $3d_{5/2}$ peak shifted from 404.5 to 405 eV and Se 3d peak shifted from 53.7 to 54.4 eV in the NP and aerogel samples, respectively. It is known[107] that the comparison of the absolute peak position is not relevant for NP systems, since it is referenced to the valence band edge of bulk CdSe, which can shift[108] due to quantum confinement effects.

To limit the effect of the band-edge shift as a function of NP size, we tested MUA capped NPs precursors and aerogel systems derived from the same NP building blocks. For the comparison between the NPs and the gel systems, the Cd $3d_{5/2}$ peak was fixed at 405.5 eV (the reference value for Cd^{2+} in CdSe NPs[107]) and the difference between it and the Se 3d peak, analyzed. This difference decreased from 351.8 eV for the MUA capped CdSe NC precursors to 350.6 eV for the CdSe aerogel samples. The data is shown in Figure 3.1.

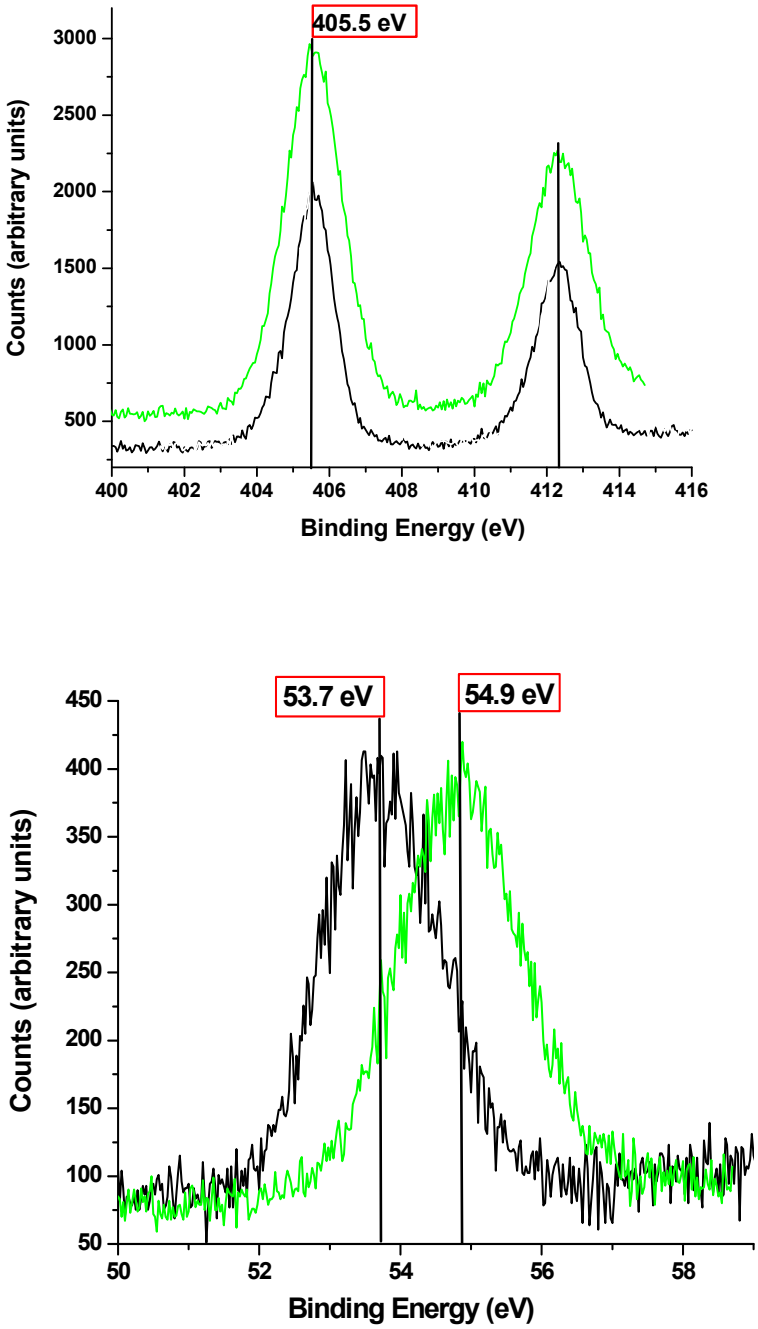

Figure 3.1. XPS spectra of the: top - Cd 3d region of MUA capped CdSe NC precursors (black) and corresponding aerogel (green); bottom – Se 3d area of the MUA-capped CdSe NPs (black, peak at 53.7 eV) and aerogels (green, peak at 54.9 eV). The escape depth of the photoelectrons in this energy range is 5-10 Å[109]

The Se 3d peak shifts by 1.2 eV from 53.7 eV in the NPs to 54.9 eV in the aerogel. This shift is intermediate between the maximum shift expected for Se^{2-} to Se_2^{2-} (0.9 eV)[110] and Se^{2-} to Se^0 (1.9 eV),[110] consistent with formation of Se_n^{2-} species (a combination of Se^0 and Se^-). Importantly, CdSe aerogel samples that were kept in air for long periods of time (a few months, Figure 3.2) show the formation of an SeO_2 peak at 59.4 eV[110], but there is no evidence of oxygen incorporation in freshly prepared CdSe gels. This confirms that surface oxygen-containing species are not formed during gelation and therefore do not participate in the interparticle bonding.

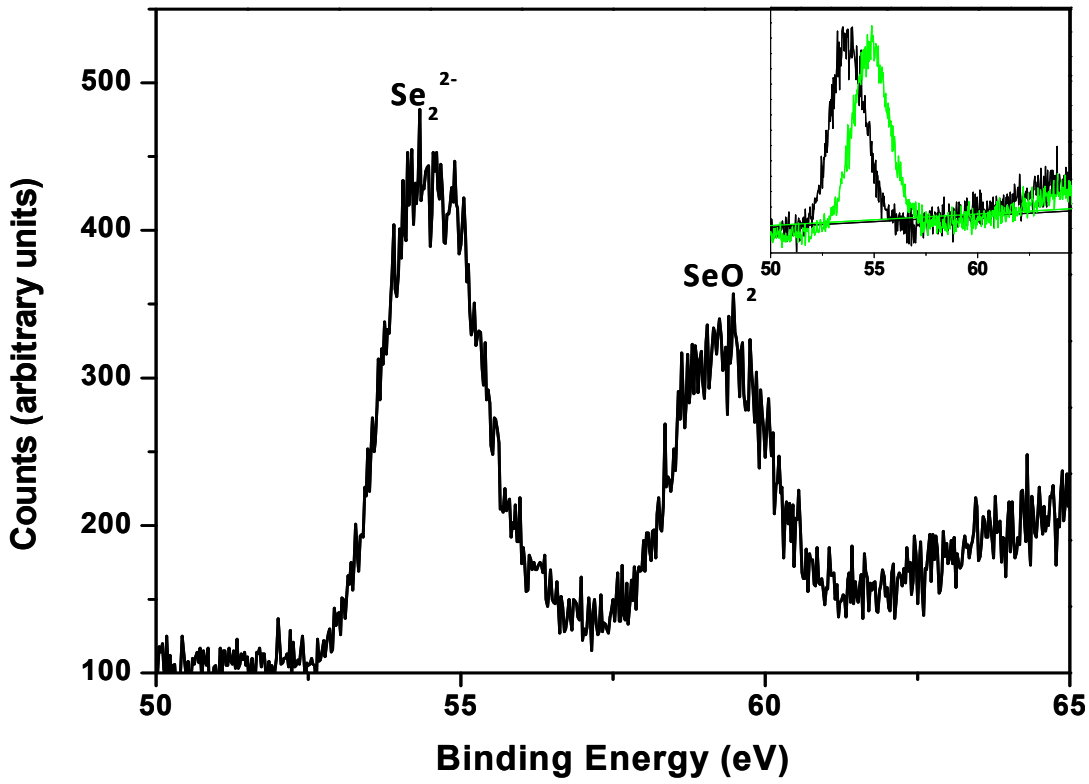

Figure 3.2. Se 3d area XPS spectra of a CdSe aerogel kept in air for one year. The peak at 59.4 eV can be indexed to SeO_2.[110] This peak is absent in the as-prepared aerogel samples (inset: black trace,CdSe NPs; green trace, CdSe aerogel)

These data strengthen the previous observation that Se-Se bond formation, arising from the oxidation of the exposed CdSe NPs, is responsible for the linkage between particles in the gel networks. To confirm that oxidation of Se^{2-} leads to Se-Se bond formation I treated Na_2Se with a methanolic solution of TNM. Even with Na_2Se: TNM mole ratios as high as 10:1, crystalline Se is formed, as evidenced by the powder X-ray diffraction (PXRD) pattern (Figure 3.3).

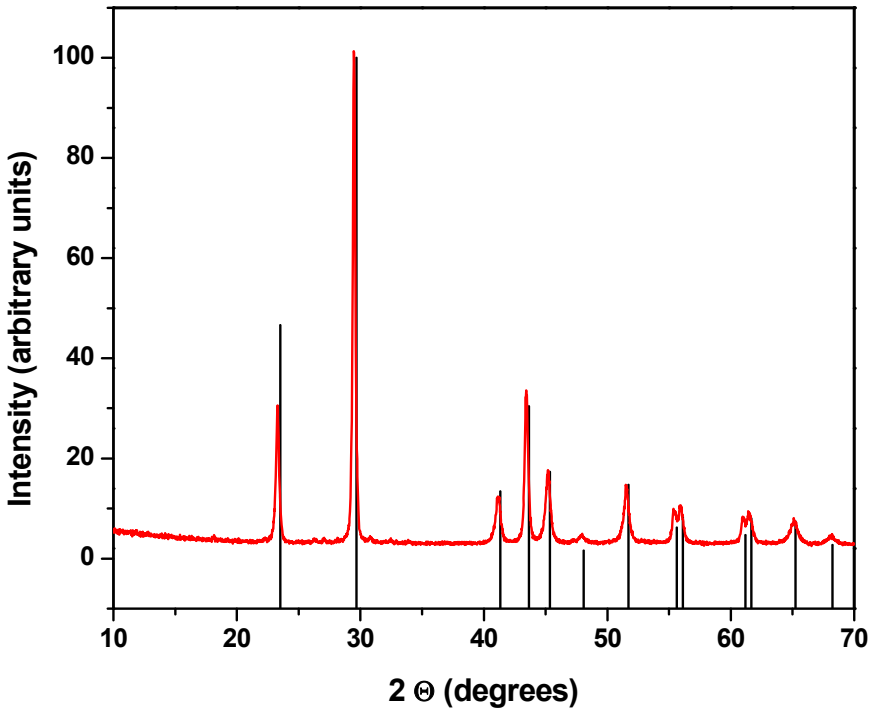

Figure 3.3. PXRD pattern of the black precipitate formed by the reaction of Na_2Se with TNM. The expected peaks for Se (PDF # 73-0465) are shown as vertical lines

Because CdSe NPs have unpassivated Se^{2-} species on their surface,[111, 112] formation of polyselenide species can be expected in the presence of an oxidizing agent, analogous to the Na_2Se to Se transformation. This, then, would explain the observation of

reversible gelation in the present case: thiols and thiolates can act as reducing agents to cleave the Se–Se bonds in these nanostructures. However, other common Lewis bases, such as pyridine, are not reducing; hence, they do not disperse the CdSe gels.

Based on the proposed mechanism (Scheme 1), the following can be predicted: 1) Cd^{2+} and oxidized thiolates will be liberated during the oxidative gelation, 2) gel dispersion can be effected with any reducing agent of suitable potential to cleave Se–Se bonds, and 3) particle etching will occur upon cycling of gelation and dispersion. The loss of Cd^{2+} and sulphur during the oxidative removal of thiolates (point 1) has been previously[94] confirmed by energy dispersive X-ray analyses. Spectra of the residue from evaporating the supernatant of a CdSe wet gel show the presence of Cd and S, and the absence of selenium. The atomic ratio of Cd: S is found to be 1:2.1, consistent with an average of two thiolates binding to one surface Cd^{2+} ion.

The previous studies[94] investigated other common reducing agents such as tris(2-carboxyethyl)phosphine hydrochloride (TCEP), (D,L)-1,4-dithiothreitol (DTT) and 2-mercaptoethanol (ME) to further probe whether the dispersion process is driven by reduction (point 2). Consistent with the formulated hypothesis, addition of the above reducing agents to wet gel structures results in a disperse solution of CdSe NPs. However, each of these reducing agents is also a good ligating agent, making it impossible to state unequivocally that it is the reducing nature of the ligand that is responsible for breaking up the gel network. Accordingly, I tested whether a “pure” (non-coordinating) reducing agent can break up the gel. To this effect, I stirred a CdSe aerogel with $NaBH_4$ in ethanol, in an ice-bath. As a control, I simultaneously stirred the same amount of CdSe aerogel in ethanol only (no reducing agent). After stirring overnight,

both monoliths have been transformed to a powder. However, TEM images (Figure 3.4) show that the $NaBH_4$ treated sample is broken into particles, while the control sample still maintains the gel structure, consistent with the proposed mechanism. The absence of a dispersed sol in the $NaBH_4$ case is attributed to the lack of suitable solubilizing functionalities.

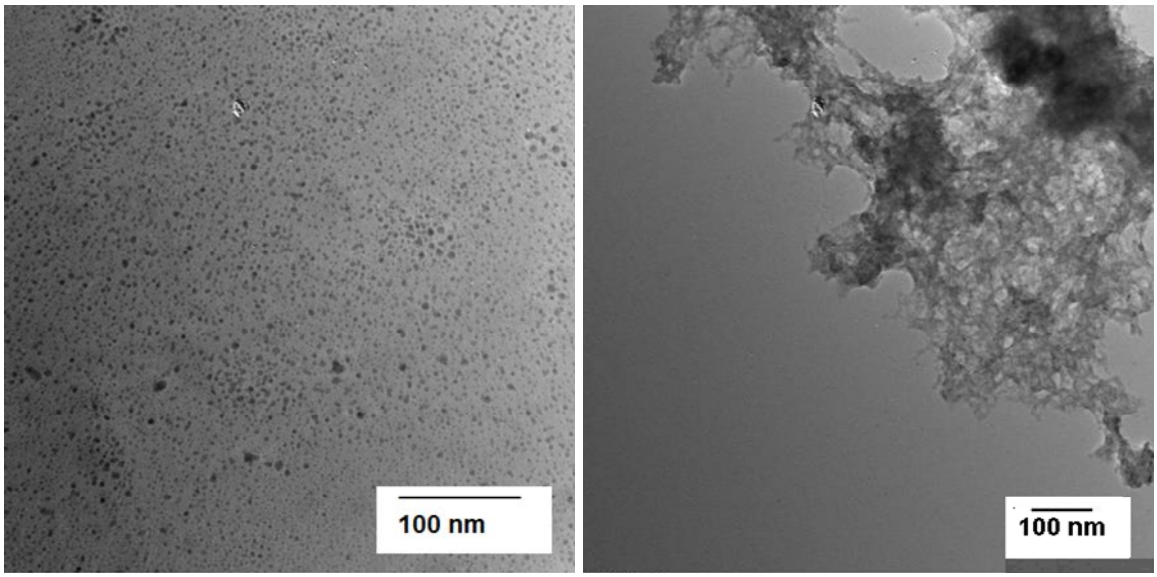

Figure 3.4. TEM images of the $NaBH_4$ (left) and ethanol (right) treated CdSe aerogel. The $NaBH_4$ treated sample has been dispersed into NPs, whereas the control sample still displays the gel network

To further differentiate the roles of reducing or ligating character on gel dispersion, I attempted to disperse ZnS wet gels using N-containing ligands (pyridine and ethylenediamine), both of which are known to have a stronger Lewis basic affinity for the harder Zn^{2+} ion than the softer Cd^{2+} ion. However, even after 1 year, the ethylenediamine and pyridine treated samples have not dispersed. On the other hand, the gels disperse

within a minute when thiols are introduced (Figure 3.5). This also supports the hypothesis that chemical reduction is a crucial step in gel dispersion.

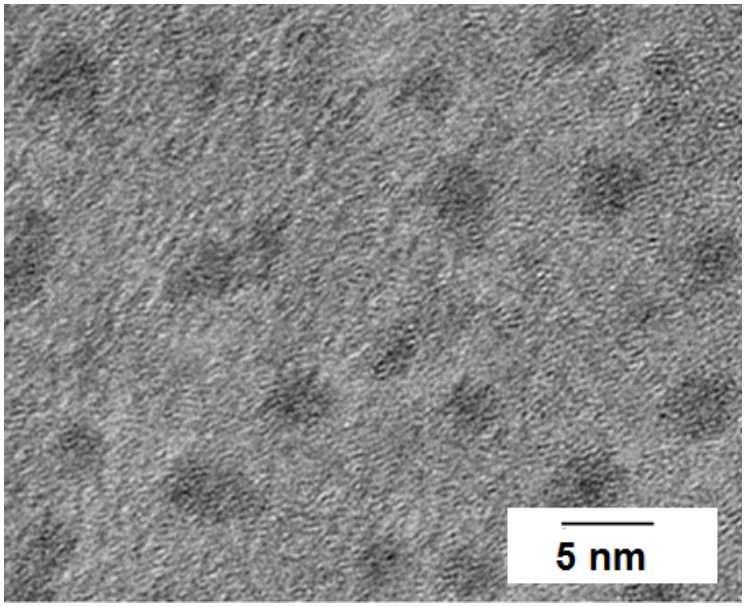

Figure 3.5. TEM images of a 4-fluorobenzenethiol-dispersed ZnS wet gel

Previous studies[94] have used powder X-ray diffraction (PXRD), transmission electron microscopy (TEM) and UV-visible spectroscopic studies (UV-vis) to probe the effect of the oxidation on the particle size (Point 3). All three techniques showed a systematic decrease in size upon successive gelation-dispersion cycles, consistent with the proposed mechanism in Scheme 3.1. A typical set of absorption data that I obtained upon repeated oxidation of CdSe NPs, followed by the reduction of the gel networks using thiolate solutions is exemplified in Figure 3.6.

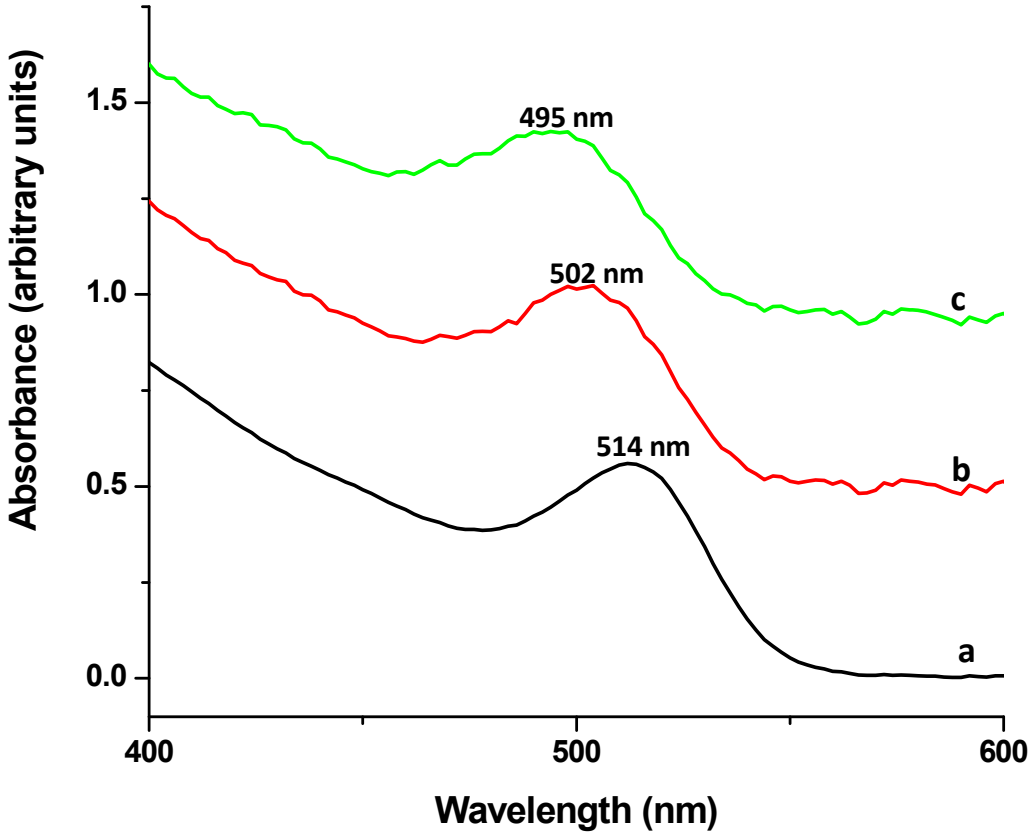

Figure 3.6. UV-vis absorbance measurements of (a) the CdSe precursor NPs, (b) NPs isolated from the dispersed wet gels, and (c) NPs isolated after a second cycle of re-gelation and re-dispersion

Absorption spectra of thiolate-capped CdSe NPs show an onset at 547 nm with a maximum at 514 nm (Figure 3.6a). After the wet gel has been dispersed by the addition of MUA, the NPs thus isolated showed a blue shift in the absorption onset position, which now occurs at 534 nm (maximum at 502 nm, Figure 3.6b). After a second gelation-dispersion cycle (i.e. treating the recovered NPs with TNM for gelation and then the monolithic wet gel thus obtained with MUA/MeOH/TMAH for dispersion), the

recovered NPs showed a further blue shift in the absorption onset to 526 nm (maximum at 495 nm, Figure 3.6c), which is consistent with the continuous decrease in particle size observed previously.[94]

It is known, though, that CdSe is susceptible to oxidation and so the observed reduction in size could also be due to the formation of an amorphous oxide layer on the NP surface. If this layer were thin enough, it would be hard to observe in TEM. Also, PXRD and UV-vis measurements would not be able to distinguish it, since they are sensitive to the crystallite and chromophore size, respectively, which would be reduced even in the event of an oxide layer formation, not only by actual particle etching. Based on the lack of Se–O species in the XPS, oxidation appears unlikely, however. To verify that the observed reduction in size is indeed due to particle etching, I tested another II-VI system, namely CdS. This system is less susceptible to oxidation than CdSe. The experiment resulted in a similar result: CdS wet gels can also be dispersed using MUA/MeOH/TMAH solutions under the same conditions as CdSe. Upon successive gelation-dispersion cycles, the UV-vis absorption maximum and onset position show a blue shift (Figure 3.7), just like CdSe, indicating that the same etching of the surface occurs.

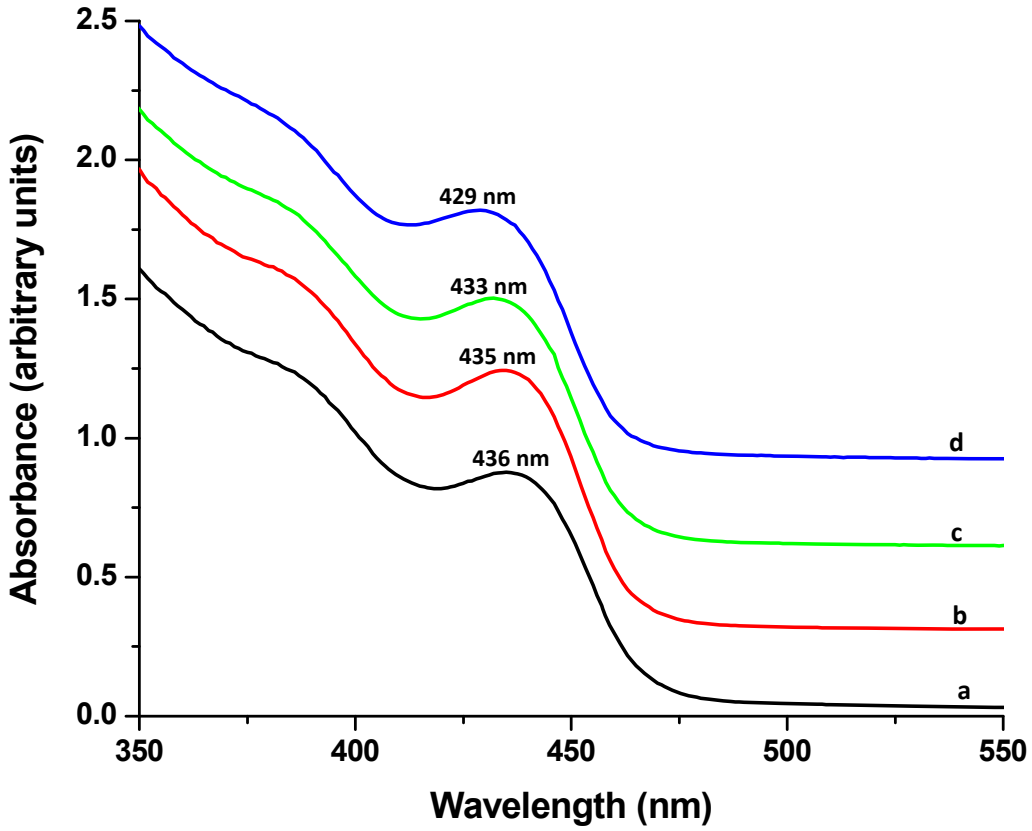

Figure 3.7. UV-visible absorption spectra of the CdS precursor NPs (a), NPs isolated from the dispersed wet gels (b), and NPs isolated after a second (c) and third (d) cycle of re-gelation and re-dispersion. The blue shift is consistent with the etching of the surface during successive gelation-dispersion cycles

Moreover, the size reduction can be monitored using transmission electron microscopy (TEM) analysis (Figure 3.8). The size of the CdS NPs decreases from 4.4 ± 0.5 nm for the original sol to 3.8± 0.4 nm, 3.7 ± 0.5 nm and 3.1 ± 0.5 nm for NPs isolated after one, two and three dispersions, respectively. Thus, it appears that a similar

oxidation-reduction mechanism is responsible for the gelation-dispersion of the CdS NPs and gels.

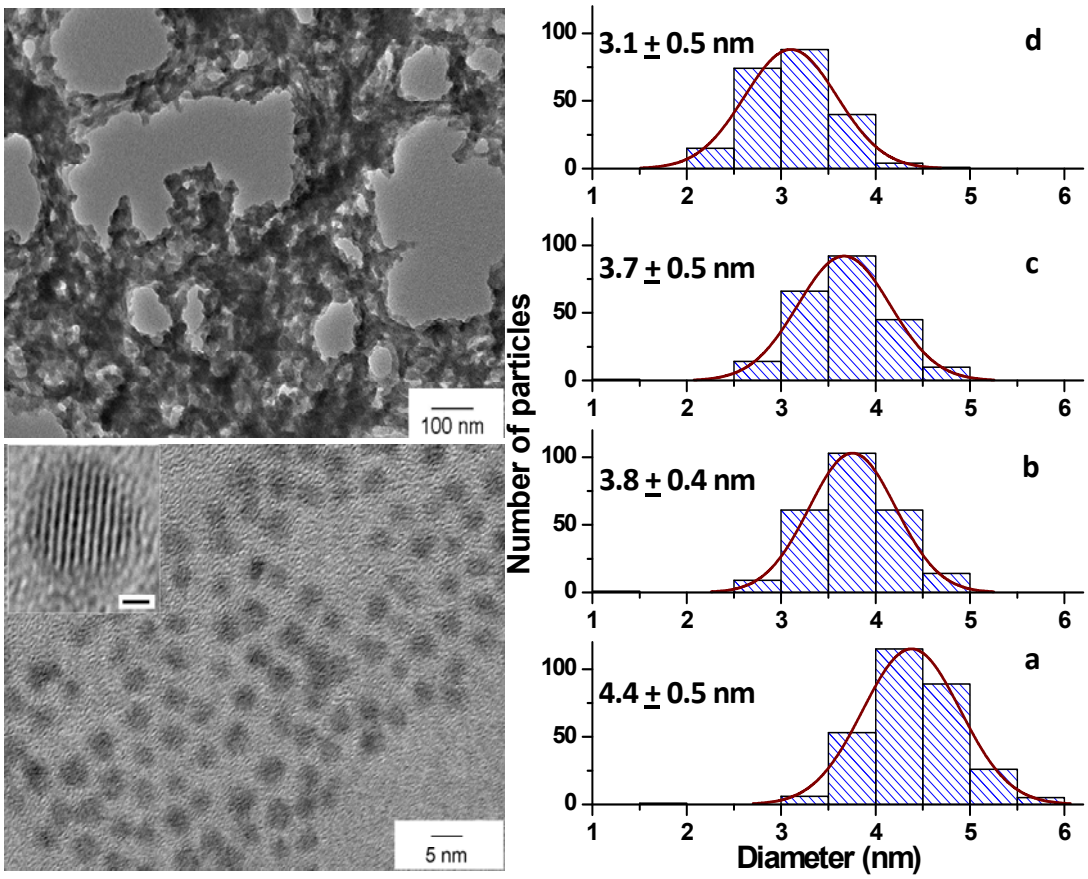

Figure 3.8. Left: TEM image of the CdS aerogel (top) and NPs after one dispersion (bottom). The inset shows the high resolution TEM image of one CdS particle (inset scale bar is 1 nm). Right: the size distribution analysis of the CdS precursor NPs (a), and NPs isolated after one (b), two (c) and three (d) dispersion-gelation cycles

A summary of the particle size estimation from the three different techniques can be found in Tables 3.1 and 3.2. There could be multiple reasons for the smaller sizes obtained by using the Scherrer formula on the PXRD pattern. One possibility is the

presence of an amorphous layer on the particle surface. We have actually not observed such a layer in TEM, but for CdSe and CdS the contrast is quite low and the amorphous layer could be difficult to resolve. The low TEM contrast might also be the reason for the consistent smaller particle size obtained by TEM, in comparison to UV-vis.

Table 3.1. Comparison of CdSe particle size calculated[94] using PXRD, TEM and UV-vis

CdSe sample	XRD size (nm)*	TEM size (nm)	UV-onset size (nm)
Initial NPs	3.0± 0.2	3.8± 0.5	4.4
After 1 dispersion	2.8± 0.2	3.5± 0.5	4.3
After 2 dispersions	n/d	n/d	4.2
After 3 dispersions	n/d	n/d	4.1

* instrument error provided by Jade software for fit of the (110) peak

Table 3.2. Comparison of CdS particle size calculated using PXRD, TEM and UV-vis

CdS sample	XRD size (nm)*	TEM size (nm)	UV-onset size (nm)
Initial NPs	3.8± 1.0	4.4± 0.5	5.1
After 1 dispersion	n/d	3.8± 0.4	5.0
After 2 dispersions	n/d	3.7± 0.5	4.9
After 3 dispersions	n/d	3.1± 0.5	4.8

*standard deviation computed from size estimates based on the (111), (220) and (311) peaks

Another reason for the discrepancy could be the accuracy of the calculation itself. When dealing with such small particles (especially in the CdSe case), the combination of size and defect broadening creates a convolution of peaks in the X-ray diffraction spectra. This makes it difficult to clearly extract the information needed (FWHM) for the use of the Scherrer formula.[113] This is evident when trying to use different peaks from the same PXRD pattern to calculate the size; when calculating the size of CdS particles using different peaks the deviation can be as large as 1 nm (Table 3.2).

By analyzing the TEM images in more detail we noticed that a lot of particles seem to have several crystalline domains oriented in different directions inside a single crystallite (Figure 3.9). Since the X-ray technique is sensitive to the dimensions of such individual domains, this could explain the smaller values obtained. These domains have been observed by other groups also, and are probably due to the colloidal growth methods of the NPs. Again, these occur more in CdSe than in CdS and can be due to the overall smaller size of the CdSe, generating more stress.

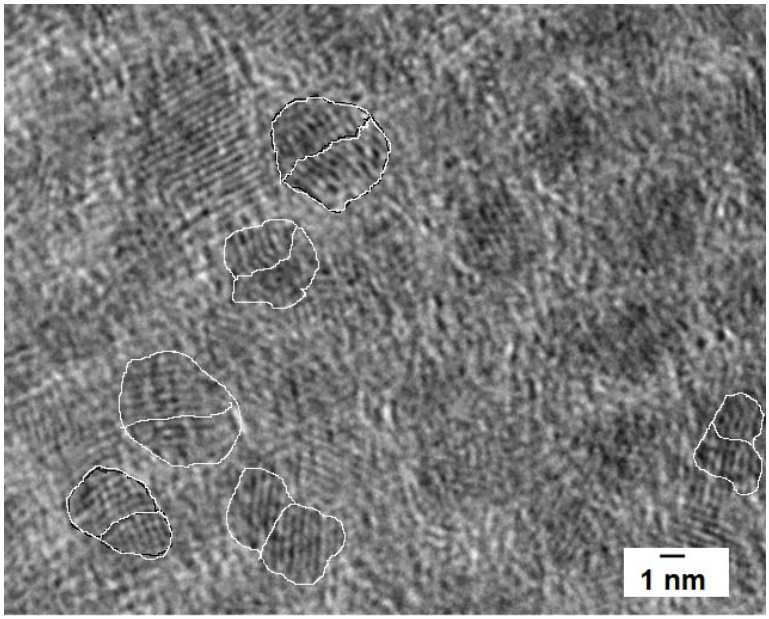

Figure 3.9. High resolution TEM image of CdSe NPs showing multiple domains

The observation of the similar behaviour of CdS gels upon treatment with a reducing agent prompts the conclusion that a similar oxidation reaction is responsible, and thus formation of S–S bonds that hold together CdS gel networks. The addition of a reducing agent cleaves the bond and disperses the gel network (Scheme 3.2).

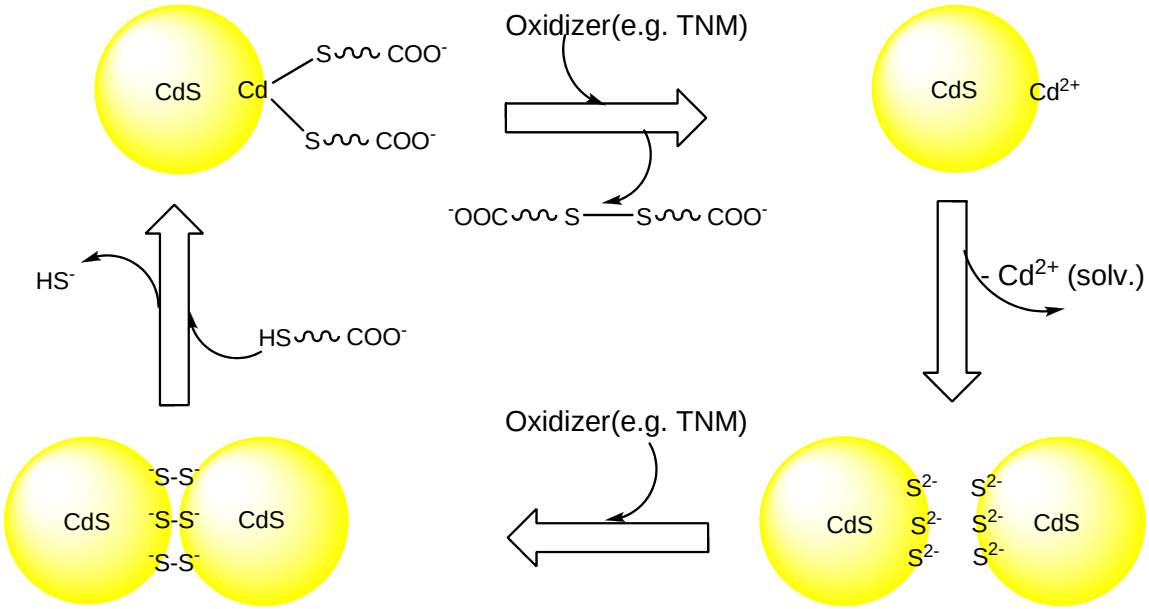

Scheme 3.2. Proposed mechanism of CdS NP gelation/dispersion

3.4 Conclusions

XPS studies strengthen the previous conclusion that the bonding between particles in as-prepared CdSe NP gels is largely due to covalent Se–Se bonds. This is why the gel networks can only be dispersed upon the addition of a suitable reducing agent (i.e. a thiol or thiolate) and not with a non-reducing Lewis base (i.e. pyridine). The fact that a "pure" reducing agent, $NaBH_4$, can break the gel network unequivocally distinguished between the role of thiol species as reductants or ligands. Cycling between oxidation and reduction causes successive surface layers to etch, effectively reducing the particle size, as was observed for both CdSe and CdS through UV-visible spectroscopy and TEM analysis.

The mechanism has been verified for CdSe and CdS and it can be surmised to extend to other metal chalcogenide NPs (i.e. ZnS, PbS) that undergo sol-gel assembly into networks. Overall, these data suggest that the well-known photochemical instability of chalcogenide semiconductor NPs can be attributed to photo-oxidation and subsequent interparticle linkage of surface chalcogenide species, not simply to aggregation of decomplexed particles, as originally proposed.[104]

CHAPTER 4

NEW AEROGEL MATERIAL GENERATION USING CATION EXCHANGE REACTIONS

4.1 Introduction

Sol-gel chemistry enables the creation of solid networks in which semiconducting metal chalcogenide NPs (i.e. CdS, CdSe, PbS, and ZnS) are linked together into a highly porous 3D network (aerogel), without organic ligands at the interfaces between particles.[93] The high porosity and dual particle/void interconnected networks enable the fast and efficient movement of matter through the structure and to the NP surfaces.[72]

I have recently demonstrated[114] that the chalcogenide gel network is held together by covalent di- or poly-selenide bonds (Chapter 3), enabling cation exchange to occur without destroying the 3D gel network. The validity of this hypothesis has been tested[78] through the conversion of CdSe gels into Ag_2Se, PbSe and CuSe simply by immersing an already gelled CdSe wet gel monolith in the cation solution of choice. The exchange resulted in complete conversion, while the monoliths remained intact.

The dissertation research investigated the extension of the cation exchange chemistry to ZnS gel networks, in an attempt to access a variety of new aerogel materials and to use the cation exchange reaction for the removal of heavy metals from aqueous solutions (Chapter 5). In the dissertation research, I targeted binary phases of Ag-S, Pb-S, Cd-S and Cu-S in order to compare the facility of ion exchange of sulfides to the previously studied selenides, and then targeted more complex ternary and quaternary phases of interest for solar cell applications ($CuInS_2$, $CuZnInS_2$).

4.2 Experimetal section

All the chemicals used in this chapter are listed in Chapter 2, Section 2.1.

4.2.1 Synthesis of ZnS NPs, gels and aerogels

Colloidal ZnS NPs were synthesized using the inverse micellar route.[24, 26, 63] In a typical synthesis, 111.53g (0.25 moles) of sodium bis(ethylhexyl) sulfosuccinate (AOT) was dissolved in 477.5 mL n-heptane. This solution was divided into two round bottom flasks and 11.25 mL of 0.15 M aqueous solutions of $Zn(NO_3)_2$ and Na_2S was added to each flask, creating the inverse micelle nanoreactors in which the reaction would occur. The solutions were then degassed under vacuum and purged with Ar gas. After 1 hour of stirring to achieve homogeneity, the sulfide solution was cannulated into the zinc solution and the resultant zinc sulfide was stirred for 12 hours. The capping groups were then exchanged by adding 1.8 mL 4-fluorothiophenol (FPhSH) and 2 mL triethylamine (TEA), causing the NPs to precipitate from solution. The NPs were isolated by centrifugation, washed with hexanes and dispersed in 20 mL acetone. The colloidal NPs were then assembled into 3D wet gel networks by adding 0.2 mL aliquots of 3% tetranitromethane (TNM) solution in acetone to each 4 mL ZnS NP sol. The wet gels were left to age for one week, and the solvent was then exchanged with fresh acetone 2-3 times a day over a two day period.

The wet gels were transformed into aerogels using supercritical carbon dioxide drying (SCD). The wet gel monoliths were dried in glass vials, with a punctured polyethylene cap to allow for solvent exchange. The drying procedure is presented in detail in Chapter 2, Section 2.

4.2.2 Cation exchange with Ag^{+}, Pb^{2+}, Hg^{2+}, Cd^{2+} and Cu^{2+}

The initial cation exchange study was conducted by carefully adding 4 mL of 0.15M $AgNO_3$, $Cd(NO_3)_2$, $Hg(NO_3)_2$, $Cu(NO_3)_2$ in methanol or $Pb(NO_3)_2$ in 1:1 v/v methanol/water solutions (representing an approximate 3 fold heavy metal excess) to ZnS wet gel monoliths that were previously exchanged with fresh methanol. The cation exchange process was conducted for various time periods (from 3 hours to two weeks, see discussion below), followed by exchange with fresh solvent, supercritical drying, and analysis of the resultant gels.

4.2.3 Exchange with Cu^{+} and In^{3+}

The exchange was performed inside an inert atmosphere glove box, using dry solvents. Stock solutions for the exchange reaction were prepared by dissolving 0.670 g CuI in 15 mL methanol and 35 mL acetonitrile (0.07 M Cu^{+}) or 0.830 g $InCl_3$ in 25 mL methanol and 25 mL acetonitrile (0.07 M In^{3+}). As a precursor, both ZnS aerogel monoliths and wet gels were used. The exchange was conducted by adding 2 mL of each Cu^{+} and In^{3+} solutions (1.5 fold metal excess) to the ZnS precursor. The vials were left undisturbed for 12 hours and were then exchanged with methanol and then acetone over a period of 3–5 hours. The solvent was then evaporated under vacuum, drying the sample into a xerogel, which was taken out of the inert atmosphere and analyzed using PXRD and TEM/EDS. For TEM/EDS, Ni grids were used so that an accurate atomic ratio could be obtained, without interference from the Cu in the grids usually used.

4.3 Results and discussion: Synthesis of binary phases via cation exchange

4.3.1 Characterization of precursor ZnS NPs and aerogels

PXRD spectra of the ZnS NPs indicate that they crystallize in the cubic structure (Figure 4.1). The broad peaks are a consequence of the small particle size. TEM images of the particles indicate that they are spherical, about 4 nm in size and well dispersed in solution. The optical properties of the NPs were investigated using PL spectroscopy. The NP sol is highly luminescent, exhibiting a broad emission peak at around 400 nm (Figure 4.1). The excitation scan indicates that the main wavelength responsible for the emission is around 330 nm, corresponding to an approximate band gap value of 3.78 eV. This is slightly higher than the bulk band gap of ZnS (3.68 eV), consistent with the widening of the band gap due to quantum confinement.

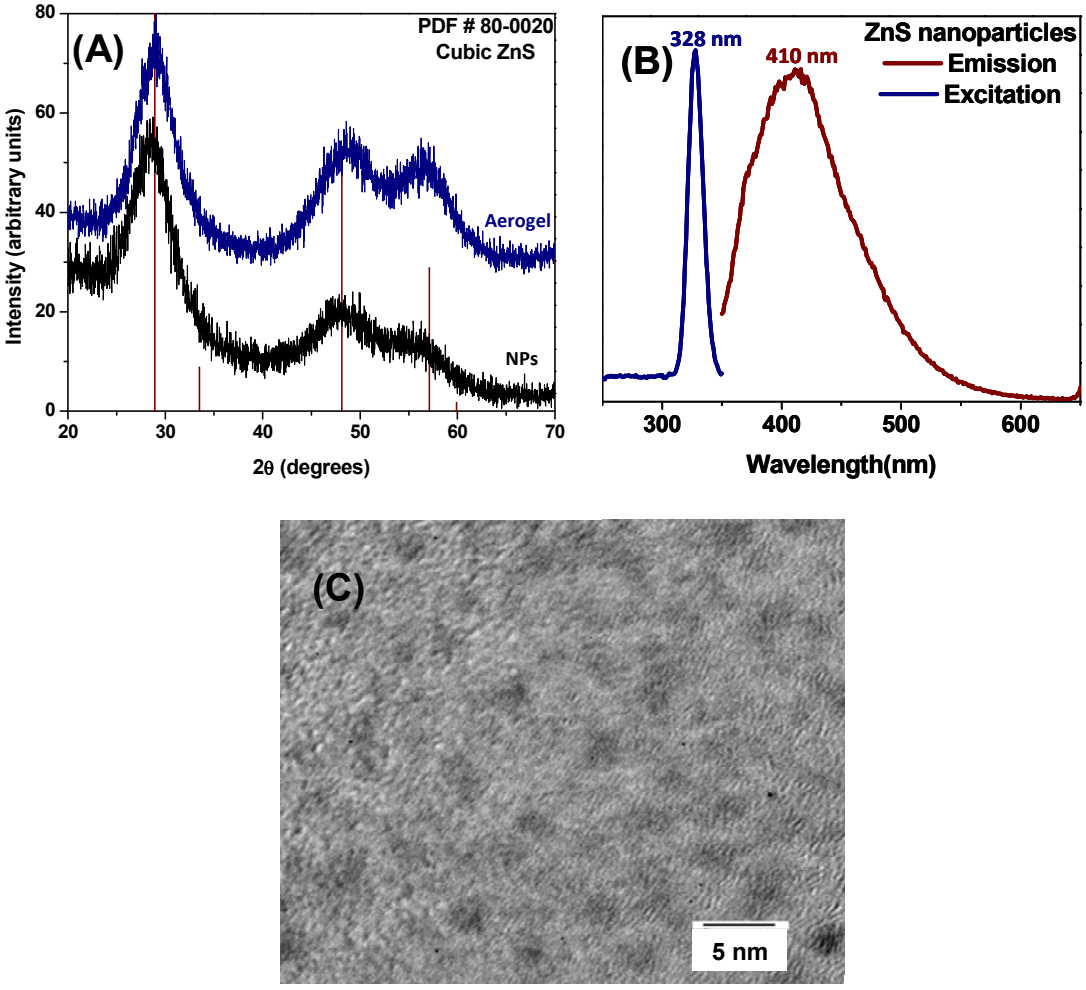

Figure 4.1. (A) PXRD spectra of ZnS NPs and aerogel; (B) PL emission and excitation spectra of thiolate-capped ZnS sol; (C) TEM image of ZnS NPs

After gelation, the crystal phase is maintained, as indicated by PXRD (Figure 4.1, A). TEM images show the highly porous, interconnected morphology specific to aerogels (Figure 4.2). Lattice fringes are visible in HRTEM, indicating the fact that the NPs are crystalline; the orientation of the different domains in the gel network indicates that the NPs maintained their individuality in the 3D structure.

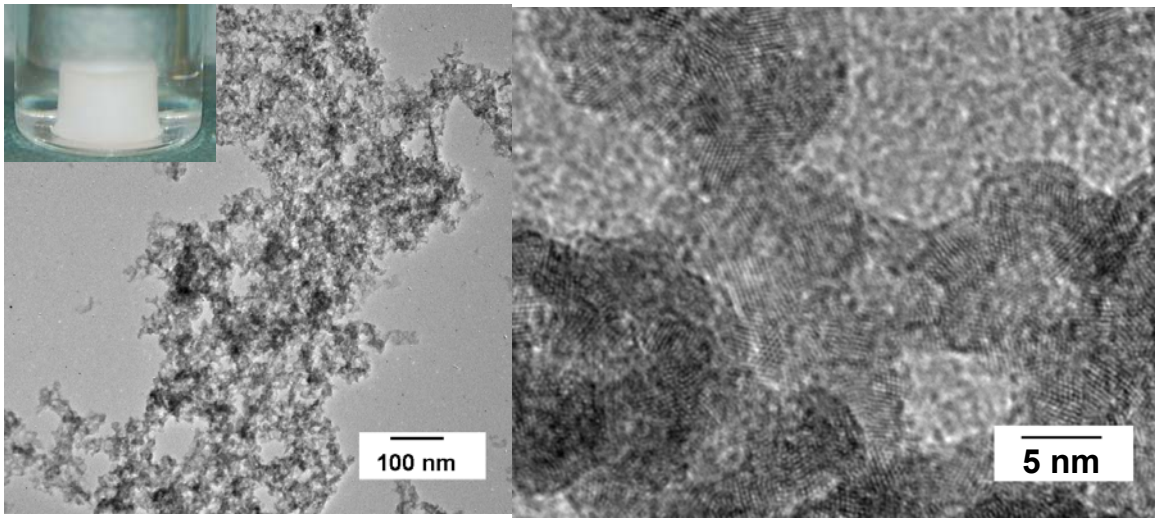

Figure 4.2. (A) TEM and (B) HRTEM image of a ZnS aerogel. The inset in (A) shows a picture of a ZnS wet gel monolith

If we consider the overall cation exchange reaction between ZnS and a heavy metal cation (H_m^{n+})

(1) $ZnS_{(s)} + Hm^{n+}_{(aq)} \leftrightarrow Hm_2S_{n(s)} + Zn^{2+}_{(aq)}$, K

it can be thought of thermodynamically as the combination of the solubilization processes

(2) $ZnS_{(s)} \leftrightarrow Zn^{2+}_{(aq)} + S^{2-}_{(aq)}$ $K_{sp1} = 3 \times 10^{-23}$

and (3) $Hm_2S_{n(s)} \leftrightarrow Hm^{n+}_{(aq)} + S^{2-}_{(aq)}$ K_{sp2} .

Thermodynamically, (1) = (2) – (3) and the equilibrium constant (K) for the cation exchange process can be derived from the solubility product constants for ZnS and HmS: $K = K_{sp1} / K_{sp2}$. As long as K_{sp1} is higher than K_{sp2} (ZnS is more soluble than the incoming metal sulfide), there is a thermodynamic driving force for the reaction. Incoming cations were thus chosen whose sulfides have different K_{sp} values, all lower that that of ZnS, but that also differed in size, charge, mobility and reduction potential

(Table 4.1), in order to gauge the influence of such factors upon the overall cation exchange reaction.

Table 4.1. Solubility product constants, reduction potentials and size of the exchanging cations

Material/ Exchanging cation	Solubility product constant (K_{sp})	Reduction potential[115] (E^0) of the cation (M^{n+}/M) (V)	Size[115] to charge ratio of cation (pm)
ZnS / Zn^{2+}	3×10^{-23}	- 0.763	37
CdS / Cd^{2+}	1×10^{-27}	- 0.403	48
PbS / Pb^{2+}	3×10^{-28}	- 0.125	60
CuS / Cu^{2+}	8×10^{-37}	+ 0.340	37
Cu_2S / Cu^{+}	2.7×10^{-42}	+ 0.520	77
Ag_2S / Ag^{+}	8×10^{-51}	+ 0.800	115
In_2S_3 / In^{3+}	1.94×10^{-68}	- 0.338	27
HgS / Hg^{2+}	2.0×10^{-53}	+ 0.854	51

4.3.2 Exchange with Ag^+

The use of cation exchange for the generation of new materials stems from the desire to use the knowledge gained from the optimization of composition and morphology of certain phases and access new ones, while circumventing tedious new optimization processes. Ag^+ is known to undergo facile cation exchange reactions in a

variety of precursor metal chalcogenide NP systems (CdSe[75], CdS[116]). Its high mobility allows for a fast exchange reaction that conserves the shape of the precursor NPs. It also allows for the exchange to occur in thin film morphologies (i.e. ZnS[117], CdS[118, 119]), where the exchange kinetics are usually prohibitive. The exchange has been extended to CdSe NP gel networks[78] yielding monolithic Ag_2Se gels in which the cation exchange occurred without destroying the anionic lattice and interparticle connecting bonds. In this dissertation research, the cation exchange behavior of ZnS NP gel networks with Ag^+ was studied. The solubility of Ag_2S is lower than that of ZnS and the reaction is thus thermodynamically favored ($K = 3.8 \times 10^{27}$).

Upon treatment of a ZnS wet gel monolith with a 3 fold excess Ag^+ methanolic solution, the color changes from white, characteristic of the wide band gap ZnS, to black, within seconds, indicating that the cation exchange occurred. The monolith stayed intact, but shrunk by about 10%. To ensure complete exchange, the vial was left undisturbed for 3 hours, in the dark (covered with aluminum foil). After that, the gel was exchanged with fresh solvent (methanol, then acetone) over two days, supercritically dried and analyzed.

PXRD data (Figure 4.3) indicate that the exchange took place, and that Ag_2S is the only crystalline phase formed. It is also obvious that the peak sharpness has increased substantially between the ZnS precursor (Figure 4.1) and the Ag^+ exchanged material, indicating an increase in the crystallite size. Applying the Scherrer formula to the (111) peak at $2\theta = 28.966^\circ$ reveals that the size has increased from 4.3 nm for the ZnS precursor gel, to 25.3 nm in the Ag^+ exchanged gel.

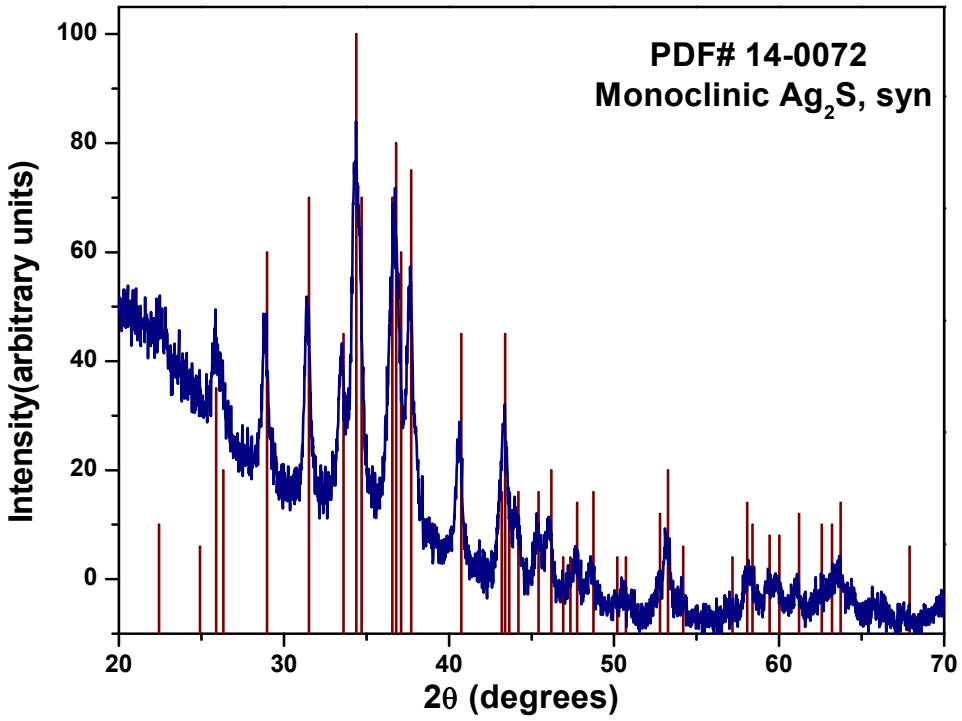

Figure 4.3. PXRD pattern of a ZnS wet gel after 3 hours exchange with Ag^{+}, in the dark

TEM images (Figure 4.4) indicate that the NP interconnectivity is maintained, and the porous structure characteristic to aerogels, conserved. The particle size in the network is between 10-20 nm, consistent with the increase observed in PXRD. EDS data show the presence of Ag and the absence of Zn, indicating that the exchange is complete, and the Ag:S atomic ratio is consistent with the Ag_2S formulation.

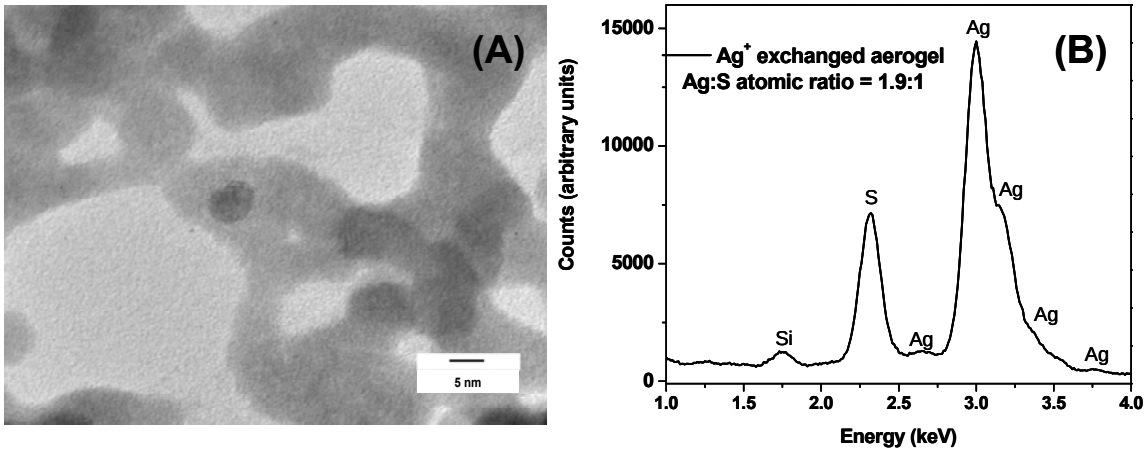

Figure 4.4. (A) TEM image and (B) EDS spectrum of a Ag^+ exchanged aerogel

When the exchange is conducted for 12 hours and the vial is left under ambient fluorescent lighting, PXRD data indicate the formation of crystalline Ag, together with the Ag_2S phase (Figure 4.5). In TEM, spherical regions of higher contrast are observed (Figure 4.6), and the EDS analysis of those regions show a higher (~ 9:1) Ag:S atomic ratio. Based on this information, I surmise that Ag NP-decorated Ag_2S aerogel can be synthesized by using a longer exchange time, in the presence of light. It is worth noting than even at short times, in the absence of light, some spherical dark features are observed in TEM, suggesting Ag NP formation (Figure 4.4). From this it can be concluded that reduction of Ag^+ to Ag is facile and difficult to control. A small peak can also be detected in PXRD, consistent with Ag formation (Figure 4.5,C).

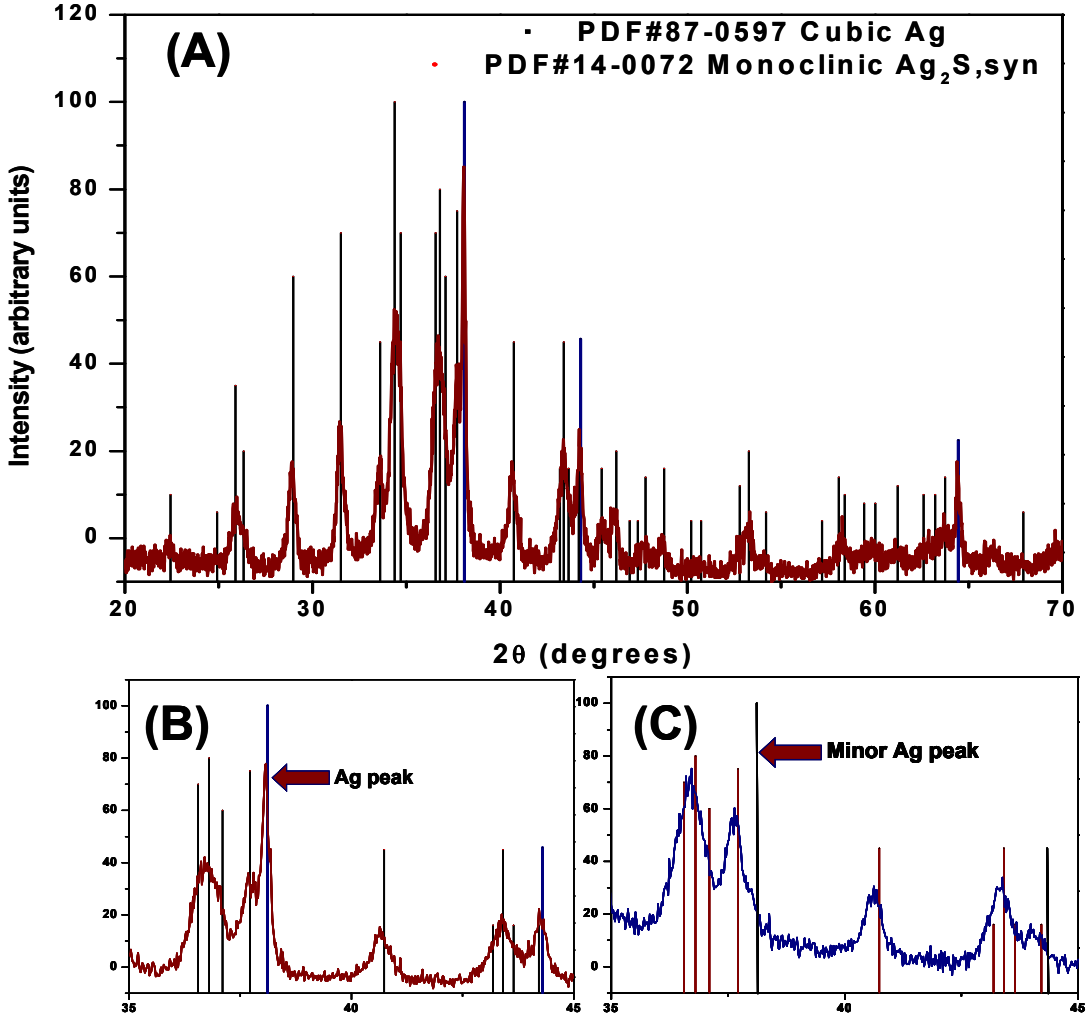

Figure 4.5. (A) PXRD spectrum of the aerogel obtained after 12 hours exchange with Ag^{+}; (B) detail of spectrum in (A) showing the characteristic Ag peak; and (C) detail of the spectrum in Figure 4.3, emphasizing the minor Ag peak for those experimental conditions

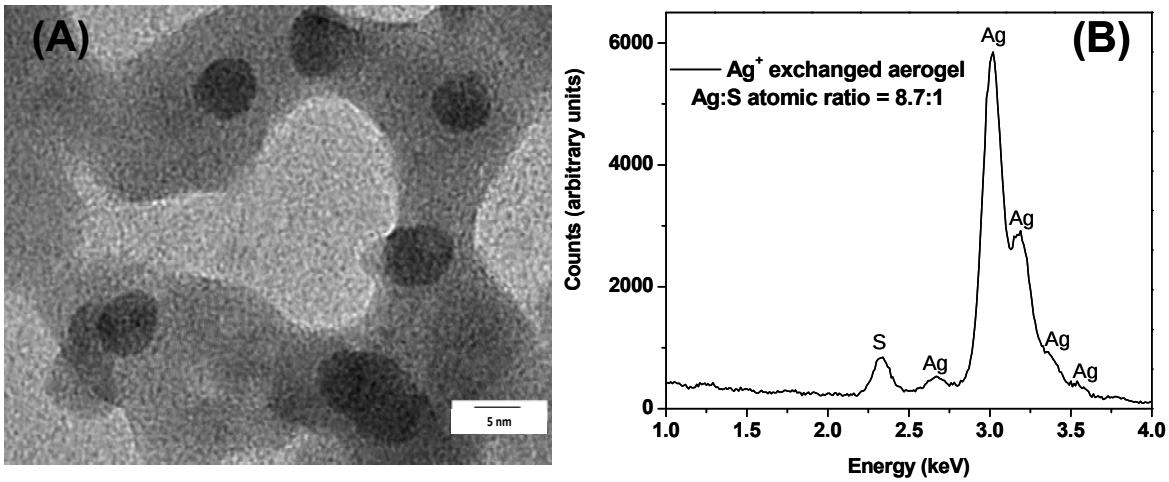

Figure 4.6. (A) TEM image and (B) EDS spectrum of the aerogel obtained after 12 hours exchange with Ag^{+}

4.3.3 Exchange with Cd^{2+} and Pb^{2+}

I investigated whether the direct exchange between dications previously studied in CdSe aerogel materials[78] can be extended to ZnS aerogels, as well as the speed of the exchange, since practical applications in water remediation would require reasonably fast kinetics. To interrogate whether thermodynamic or kinetic factors are the main reaction driving factor in our systems, we compared Pb^{2+} and Cd^{2+} as the incoming exchanging cations, since their sulfides have similar solubility constants (K_{sp}) : K_{sp} = 3 x 10^{-28} for PbS, and 1 x 10^{-27} for CdS. These values are similar, and lower than that for ZnS (K_{sp} = 3 x 10^{-23}), and thus the solubility-based reaction driving force is similar for the exchange of both cations.

Wet gels of ZnS were treated with solutions of Pb^{2+} and Cd^{2+} under forcing conditions (3 fold excess of exchanging ion) and the process monitored visually by the gel color change. Results indicate (Figure 4.7) that the Zn^{2+} cation can be exchanged with

Pb^{2+} and Cd^{2+} upon treatment of ZnS wet gels with solutions containing these ions in a one step cation exchange reaction, under very mild conditions (room temperature, methanol (Cd) or methanol/water (Pb) solvent).

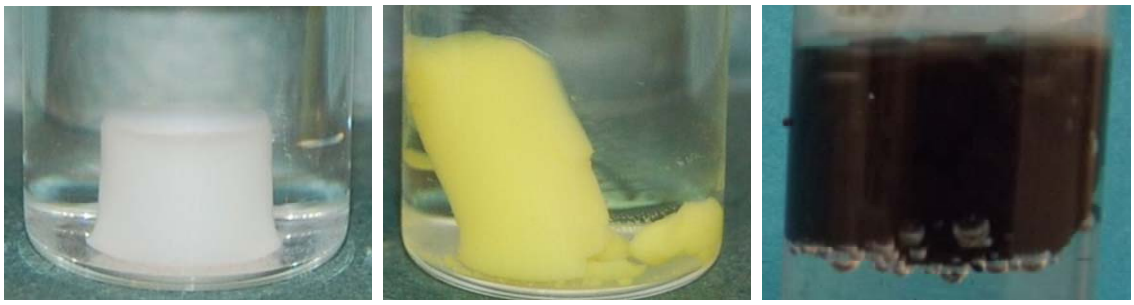

Figure 4.7. Pictures of a (left) ZnS wet gel; (middle) Cd^{2+} and (right) Pb^{2+} exchanged wet gel, showing the specific color change and the conservation of the 3D gel monolith integrity upon the cation exchange. (The size of the monoliths is not to scale, nor does it represent a series in which a particular ZnS monolith was exchanged)

A first observation was that the timescale of the exchange is very different for the two ions: the exchange between Pb^{2+} and Zn^{2+} (color change from white ZnS to black PbS) happened in less than one minute, while the characteristic yellow color of CdS did not appear until several days later. For both systems, the gel networks remained undisturbed (Figure 4.7), as previously observed in the selenide systems.[78] PXRD data of the xerogels resulting from exchange with Pb^{2+} overnight and with Cd^{2+} for two weeks show that the incoming metal cation has been incorporated into the lattice, generating PbS and CdS (Figure 4.8) and that crystallinity is preserved as the structure changes. The peak sharpness increases for the faster Pb^{2+} exchange, indicating that the crystallite size has increased. Using the Scherrer equation, the crystallite size can be calculated to be 4.3 nm for the ZnS precursor gel, 4.1 nm for the Cd^{2+} and 18.6 nm for the Pb^{2+} exchanged

gels. The small size difference observed between the ZnS and Cd^{2+} exchanged material is indicative of the fact that during the slow exchange process, the anionic network is not, or very little, disturbed. The fast Pb^{2+} exchange, though, proceeds with a greater lattice rearrangement and causes the particle building blocks to grow in size, similar to the Ag^{+} exchanged samples. Nevertheless, the NPs maintain their connectivity and the integrity of the gel network is conserved (Figure 4.7).

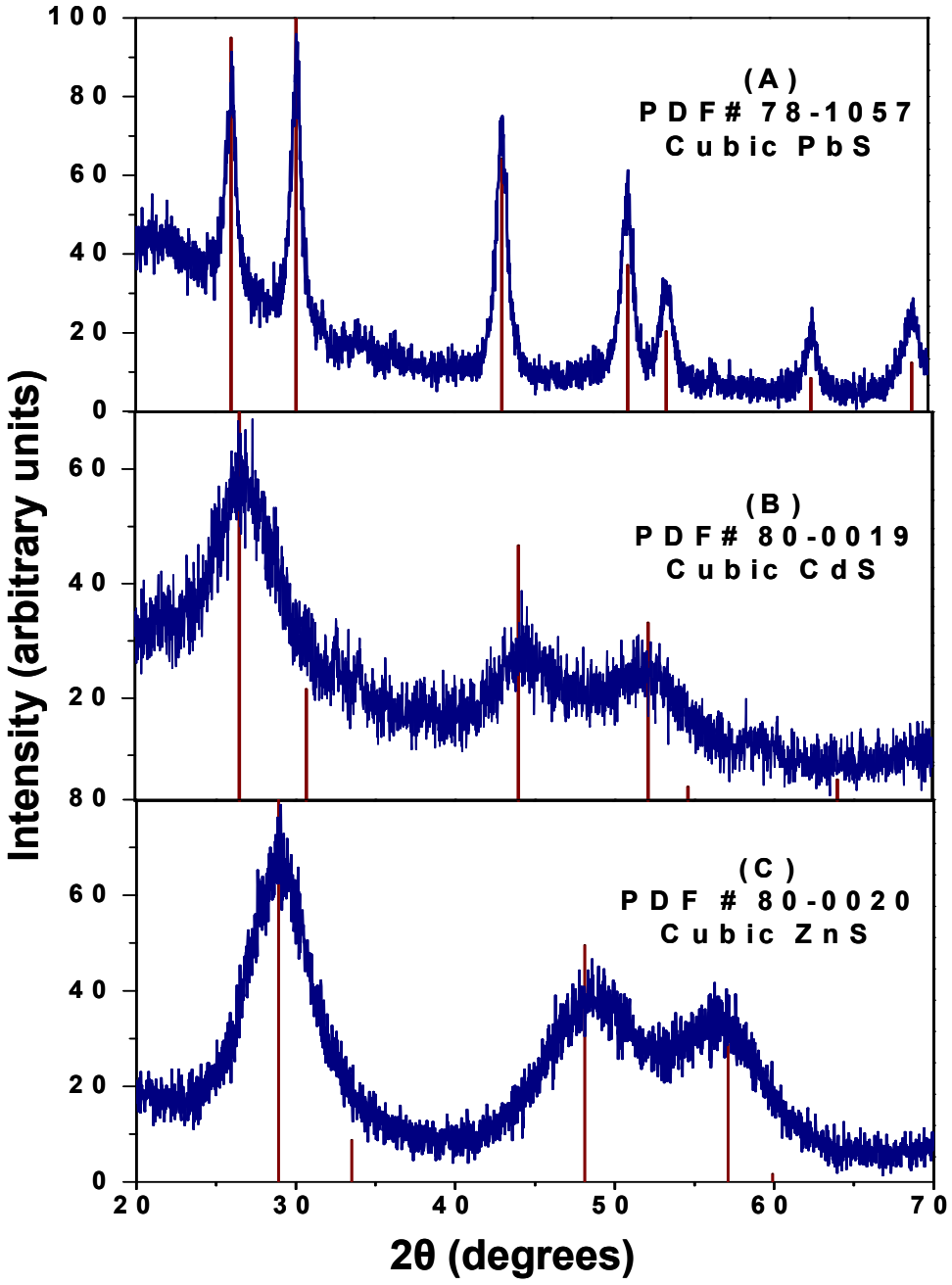

Figure 4.8. PXRD spectra of (A) Pb^{2+}, (B) Cd^{2+} exchanged ZnS xerogel, and (C) ZnS precursor gel. The vertical lines represent the respective crystal patterns, according to the PDF patterns noted in the figure

TEM images (Figure 4.9) confirm the retention of the gel network connectivity during exchange. The minimal increase in NP size indicated by the PXRD data is consistent with crystallite sizes indicated by TEM for ZnS (~ 4 nm) and CdS (~ 5 nm) materials. Likewise, TEM reveals PbS primary particle sizes on the order of 7–15 nm, confirming the increase in crystallite size noted by PXRD. EDS analyses show that not all ions exchange equally (e.g. removal of Zn^{2+} by displacement with Cd^{2+} proved difficult to drive to completion). The reason for the incomplete cation exchange between Cd^{2+} and Zn^{2+} might stem from the known capacity of II-VI compounds for forming pseudobinary alloy systems.[73, 120] On the other hand, IV-VI compounds are sparsely soluble in II-VI crystals, and thus the ion exchange of ZnS with Pb^{2+} is expected to form heterostructures, not solid solutions, leading to complete conversion, which is what we observe.

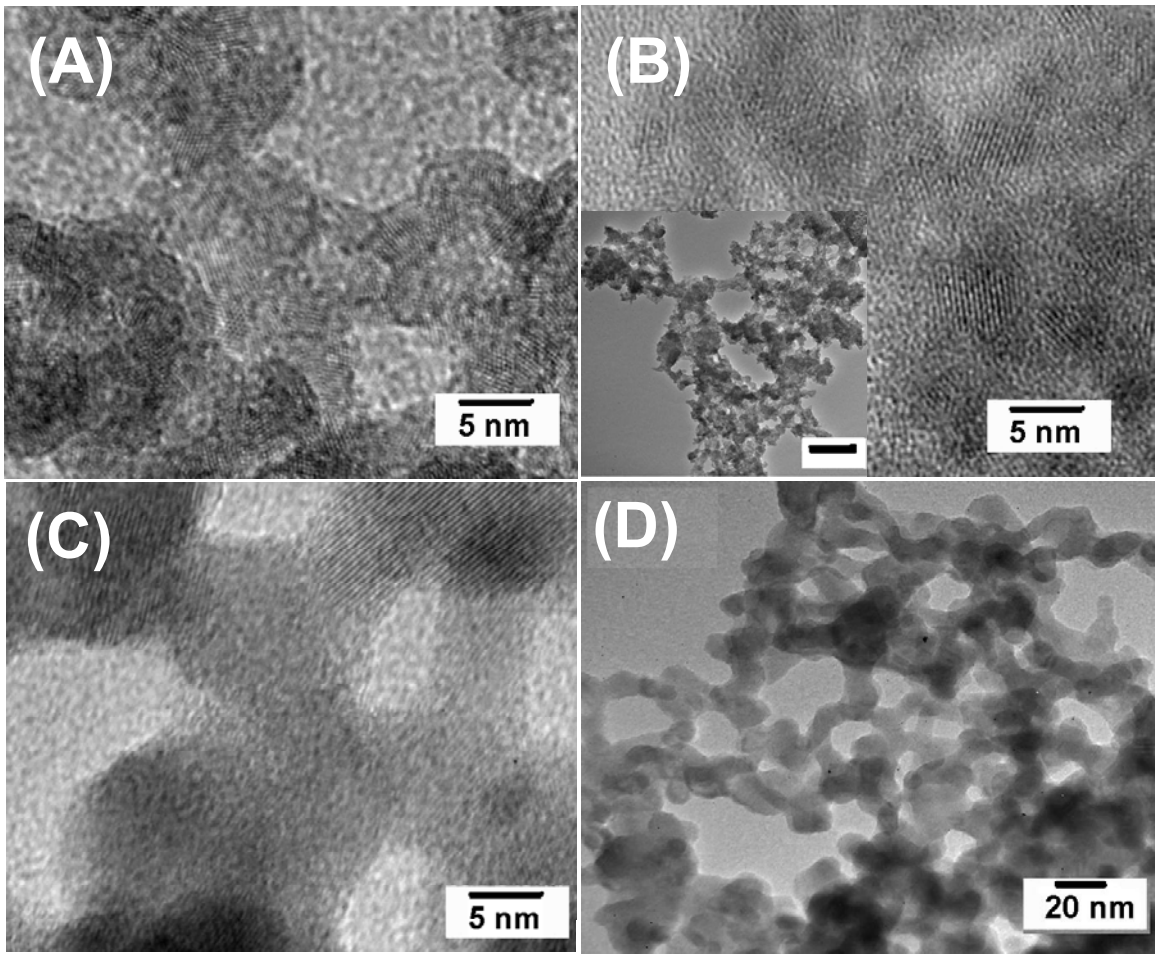

Figure 4.9. TEM micrographs of (A) ZnS precursor aerogel and (B) Cd^{2+} and (C, D) Pb^{2+} exchanged ZnS aerogel networks. The inset in B shows a lower magnification of the Cd^{2+} exchanged gel, with the gel network intact (scale bar 100 nm). The NP size increases slightly during the cation exchange (B, C), but the gel network remains connected (B inset, D)

Based on these data, it can be surmised that the ion-exchange reaction occurring in the ZnS gel materials is driven by factors other than solubility, since ions with similar solubility product constants exchange at very different rates (minutes for Pb^{2+}, days for Cd^{2+}). The speed of the exchange correlates with the difference in the reduction potential

between Zn^{2+} and the incoming metal cation: the bigger the difference, the faster the exchange (Table 4.2). A similar trend was previously reported[76] for the cation exchange of ZnS thin films. This trend has been justified by the fact that the low solubility and highly covalent character of heavy metal sulfides causes the electrochemical electron transfer to have a higher importance over solubility-difference-driven conversion. The facile exchange observed in the case of Ag^{+} is also consistent with the large difference between the two metals' reduction potentials (Table 4.2).

Table 4.2. Solubility product constants, reduction potentials and observed cation exchange speed for ZnS and cation exchanged aerogels

Material	Solubility product constant (K_{sp})	Reduction potential (E^0) of the cation (M^{n+}/M) (V)	ΔE^0 (M^{n+}/M – Zn^{2+}/Zn) (V)	Qualitative speed of exchange
ZnS	3×10^{-23}	- 0.763	-	-
CdS	1×10^{-27}	- 0.403	+ 0.360	weeks
PbS	3×10^{-28}	- 0.125	+ 0.638	minutes
CuS	8×10^{-37}	+ 0.340	+ 1.103	minutes
Ag_2S	6×10^{-53}	+ 0.800	+ 1.563	seconds
HgS	2×10^{-53}	+ 0.854	+ 1.617	seconds

This study allowed for a better understanding of one of the factors affecting the exchange mechanism, which will facilitate the optimization of the reaction conditions and the extension to other heavy metals for remediation studies. The process should be generic and should work for any metal with a more positive standard reduction potential than that of Zn(II)/ Zn. The trend was tested by using Hg^{2+} for the exchange (K_{sp}= 2 x 10^{-53}, $E^0_{Hg^{2+}/Hg}$ = +0.854 V). When a ZnS wet gel is treated with a solution of Hg^{2+}, the white gel turns black almost immediately, suggesting exchange for Hg^{2+} has occurred and happens more rapidly than for Pb^{2+}, as expected based on the large, positive reduction potential.

The observation of the direct exchange between divalent metal cations is different from previous work on cation exchange in NP systems,[120-123] in which CdSe/CdS NPs were reported to be unable to directly convert to PbSe/PbS under mild reaction conditions, requiring an intermediate step of converting to Cu_2Se/Cu_2S. These previous reports justified their observations based on the assumption that the cation exchange reactions are driven mainly by the difference in solubility of the incoming and outgoing cation in various solvents, and thus a direct exchange between two similar dications would not be possible, requiring the intermediate singly charged ion exchange step.

The observed ability of our material to undergo direct cation exchange between two cations with the same charge stems from the fact that, unlike the previously reported NP systems, the capping groups that are normally used to stabilize NPs are almost entirely removed in our systems during the gelation process, leaving behind a surface that is much more easily accessible to the incoming cation. Previous reports[66] have shown that the S content — indicative of the coverage of thiol surfactants used to stabilize the NPs—

decreases from almost 20% for CdSe NPs to about 10% in the corresponding aerogels. Once the surface cations are exchanged, the concentration gradient created generates a reaction potential (Donnan potential[124]) that is propagated through the gel network, allowing for the complete exchange. Indeed, we find that treating a thiolate-capped ZnS NP sol with 0.15 M $Pb(NO_3)_2$ solution (the same conditions as the wet gel exchange) required nearly a month for conversion (Figure 4.10). Other studies have also shown that there is a kinetic effect that depends on the surfactant nature and concentration, where a decrease in the speed of reaction with increased surfactant concentration was observed.[125, 126]

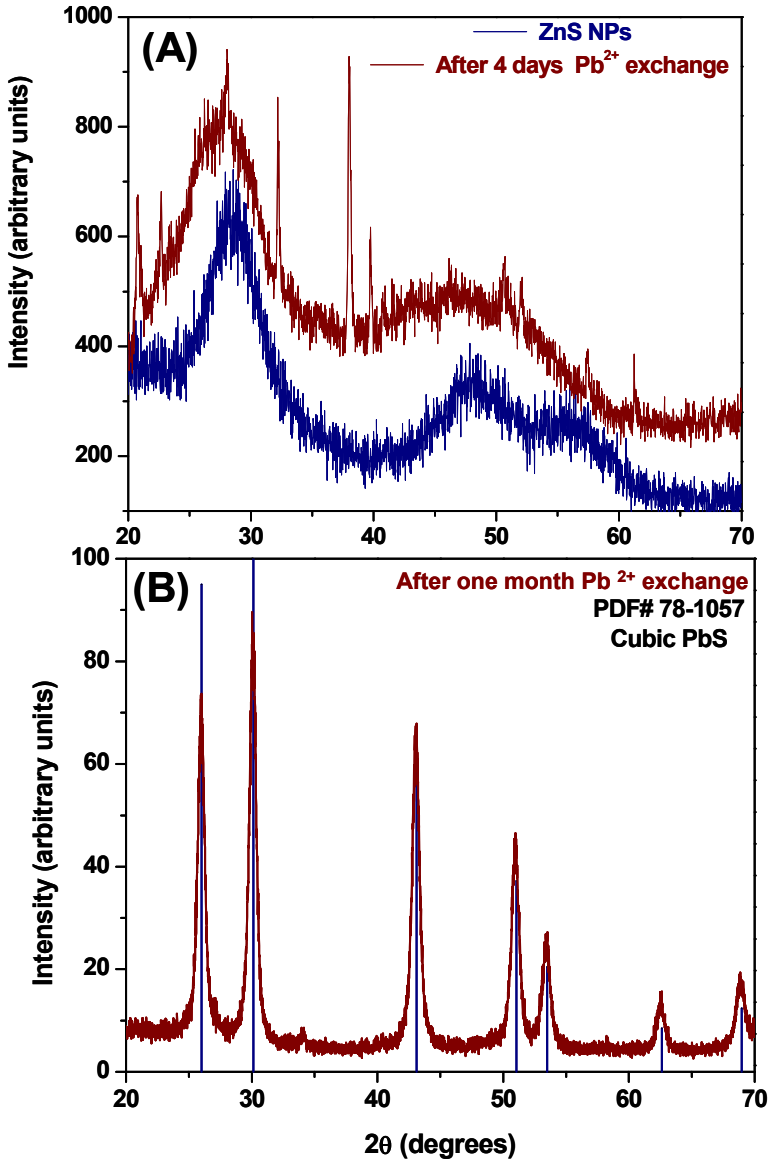

Figure 4.10. (A) PXRD spectra of thiolate-capped ZnS NPs precursor (navy) and after four days of exchange with Pb^{2+} (red). The sharp peaks in the wine-colored trace are from unwashed bulk $Pb(NO_3)$. (B) PXRD spectrum of thiolate-capped ZnS NPs after one month of exchange with Pb^{2+}. The vertical lines correspond to the cubic PbS crystal phase

The resulting aerogels surface area/porosity was characterized using N_2 adsorption/desorption isotherms (Table 4.3).

Table 4.3. Measured surface areas and silica equivalents for ZnS and cation exchanged aerogels

Sample	Measured surface area (m^2/g)	Silica equivalents[a] (m^2/g)	Primary NP radius (nm)	Total pore volume (cm^3/g)	Average pore diameter (nm)
ZnS aerogel	368	596	2.2	1.42	13.1
CdS[b] aerogel	88	210	2.1	0.178	8.13
PbS aerogel	49	195	9.3	0.178	12.8
$Cu_{7.2}S_4$ aerogel	206	328	4.6	0.641	10.0
Ag_2S aerogel	37	154	10.0	0.140	12.1

a) Silica equivalents were calculated by converting the grams of metal sulfide gel into moles and consequently into grams of silica. This is a standard way of comparing the surface area of different materials, and also referencing them to the more well-known porous silica materials.

b) The cadmium exchange resulted in a solid CdS/ZnS solution; the silica equivalents for the samples were calculated assuming complete exchange.

The decrease in surface area upon cation exchange is proportional to the NP building block increase (for an equal volume of material, increasing the NP diameter from 4.3 for ZnS to, i.e. 18.6 nm in the case of PbS, results in a theoretical decrease of surface area of

75%, when compared to the initial surface area: it scales as R_1/R_2, where R_1 and R_2 are the initial and final radii, respectively). This conclusion is substantiated by the almost constant average pore diameter and the corresponding decrease in the total pore volume. The Cd^{2+} exchanged gel is an exception, showing a decrease in the average pore diameter, as well. Probably, the slow exchange time resulted in more aging of the gel networks, since gelation is a dynamic, continuous process.

4.4 Exchange with Cu^{2+}, Cu^{+} and In^{3+}

The solubility product constants of CuS, Cu_2S and In_2S_3 are lower than that of ZnS (Table 4.1), so the exchange reactions are thermodynamically favored. Considering the reduction potentials, though, and the trend observed (Table 4.2) for the cations tested above, Cu^{2+} and Cu^{+} are expected to exchange faster than In^{3+}.

The exchange with Cu^{2+} was conducted in air, overnight. The color changed from white to black immediately after the addition of the Cu^{2+} solution, indicating that the ion exchange occurred. The PXRD of the Cu^{2+} exchanged aerogel has a raised baseline (Figure 4.11), which could be indicative of the presence of disorder in the structure, or the possibility of more than one stoichiometry of Cu_xS_y. The main peaks can be indexed to $Cu_{7.2}S_4$, indicating that, similar to the Ag^{+} case, the Cu^{2+} underwent a reduction reaction, probably to Cu^{+}. Unlike the case with Ag^{+}, the complete reduction to Cu^{0} was not observed in the PXRD spectrum. TEM images (Figure 4.11) indicate that the particle interconnectivity and the gel network were retained, as well as the presence of lattice fringes characteristic of a crystalline sample. The sample contrast was uniform throughout, without the presence of higher-contrast regions observed for the Ag^{+}

exchange, which in that case indicated phase segregation. EDS data indicates a Cu:S atomic ratio of 2.3:1, which also corresponds to the reduction of Cu^{2+} to Cu^{+} and suggests an even more metal-rich phase is present in addition to the $Cu_{7.2}S_4$ indicated by PXRD. Alternatively, the higher copper ratio might be due to incomplete washing of the exchanging metal ion, or complexation by the thiolate capping groups still present on the wet gel surface. The fast kinetics of the exchange is in agreement with the observed trend based on reduction potentials (Table 4.2). Also, the positive reduction potential of Cu^{2+}, just like that of Ag^{+}, is conducive for the reduction of the metal, not only the cation exchange reaction.

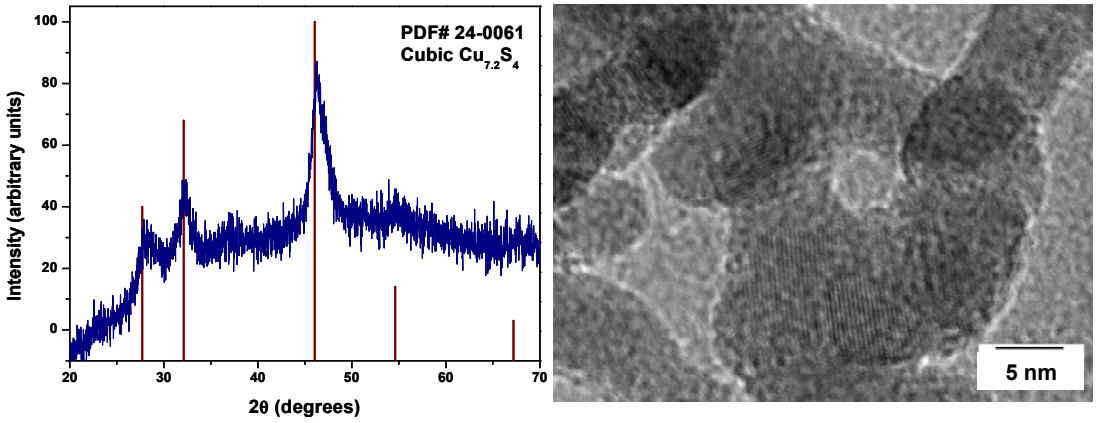

Figure 4.11. PXRD spectrum (left) and TEM image (right) of a Cu^{2+} exchanged aerogel

The fact that the Cu^{2+} exchanged with Zn^{2+} indicated that a synchronized exchange with Cu^{+} and In^{3+} might be possible. The goal of this reaction was to access $CuInS_2$, which is highly desirable for photovoltaic applications. Upon the addition of the Cu^{+} and In^{3+} solutions to the aerogel, the color changed to black instantaneously. The sample in which a wet ZnS gel was used as a precursor changed color gradually from

white, to yellow, then red, brown and finally black within a couple of hours. As a note, the exchange with In^{3+} by itself was attempted by treating a ZnS wet gel with 2 mL of the same 0.07 M $InCl_3$ solution used in the simultaneous Cu^{+} and In^{3+} exchange. No initial color change was observed, and the gel monolith seemed to have dispersed overnight. PXRD and EDS analysis of the dispersed sol show no indication of In being incorporated in the sample. This observation is consistent with the negative reduction potential of In^{3+} and it follows the reaction speed trend observed for Ag^{+}, Cd^{2+} and Pb^{2+}.

PXRD patterns show broad peaks and a raised baseline, indicating slight disorder in the lattice (Figure 4.12) and also the possibility that more than one stoichiometry is present. TEM images show the presence of lattice fringes in the exchanged gel and EDS data indicates that both Cu and In have been incorporated (Figures 4.13, 4.14), but the sample in which the aerogel was used as precursor still exhibits a signal for Zn, indicating that the exchange was not complete. The fact that In^{3+} can be incorporated in the lattice when Cu^{+} is also present, as opposed to the instance of it being the only exchanging cation, suggests that the mobile Cu^{+} can act as a promoter for the cation exchange process, creating the potential needed for the less mobile In^{3+} to exchange. The reason for the incomplete exchange in the aerogel sample might reside in a "wettability" capacity of the dried sample, i.e. the reacting solution being unable to penetrate some of the smaller micropores present in the gel network. This, combined with the sluggish In^{3+} diffusion, resulted in incomplete exchange. This does not seem to be the case in the wet gel precursor, where there is no indication of Zn after the exchange, but the resultant material is also of low crystallinity, and with additional peaks that cannot be accounted for, but

which may suggest the presence of one or more impurity phases that form under the mild reaction conditions employed.

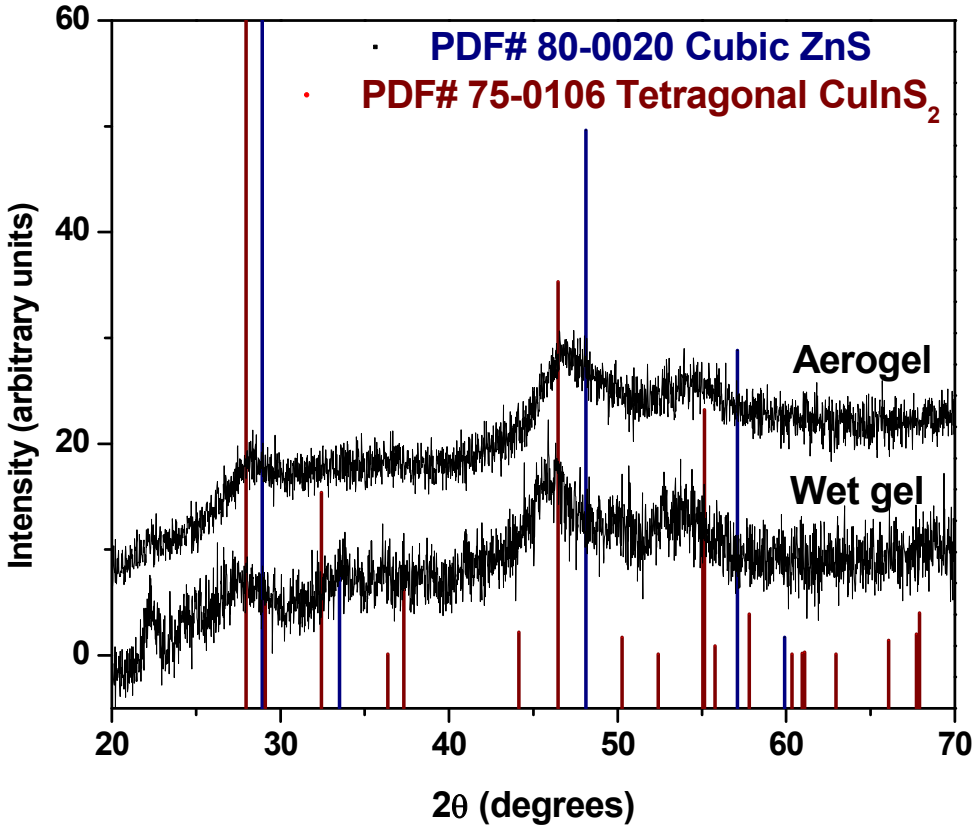

Figure 4.12. PXRD spectra of Cu^{+} and In^{3+} exchanged aerogel and wet gel

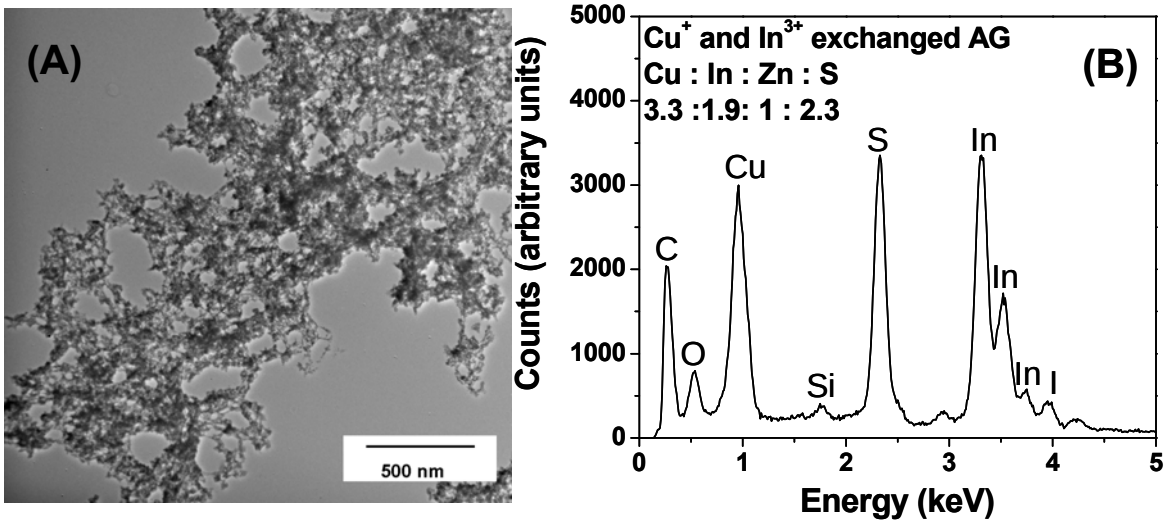

Figure 4.13. (A) TEM image and (B) EDS data of the Cu^{+} and In^{3+} treated ZnS aerogel

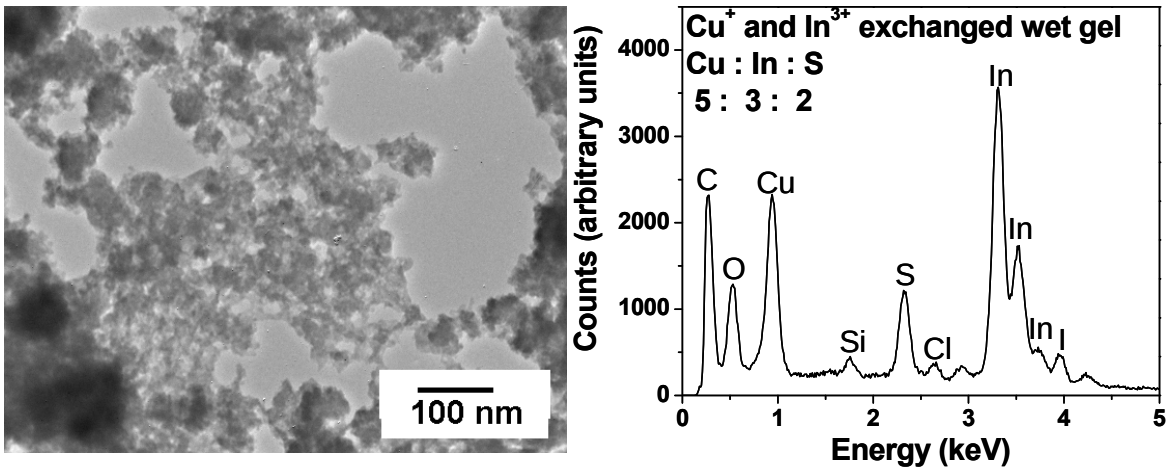

Figure 4.14. TEM image and EDS data of Cu^{+} and In^{3+} exchanged ZnS wet gel

Overall, under the mild conditions used for the exchange, and in agreement with the previous observed reaction kinetics trend, the complete exchange with Cu^{+} and In^{3+} and the achievement of a definite $Cu_xIn_yS_z$ crystal phase was not achieved. The reason for the non-stoichiometric ratios observed in EDS might be the presence of excess metals,

due to incomplete washing of the samples. Washing with another solvent, such as acetonitrile, could allow for the achievement of less metal-rich ratios. Cu (I) acetate and In (III) acetate were used as the metal ion sources to analyze the effect of the counterion on the exchange. Indium acetate is very sparingly soluble in methanol or acetonitrile and copper acetate disproportionates readily even with degassed and dried solvents, under inert atmosphere. Also, in an attempt to increase the mobility of In^{3+} and perform the exchange, 0.1 M solutions of $InCl_3$ in ethylene glycol were added to ZnS aerogel and wet gel samples, and the reaction mixture was heated at 175 ˚C for 12 hours. No color change was observed, and the gels densified upon heating. After washing with acetone and methanol, no In^{3+} incorporation could be observed in PXRD.

4.5 Conclusions

The current study has shown that ZnS aerogel materials are capable of undergoing cation exchange reactions with dications (i.e. Pb^{2+}, Cd^{2+} and Hg^{2+}), directly, under mild reaction conditions. The presence of an accessible pore structure is paramount for the promotion of the reaction. The ZnS gel materials studied possess a characteristic dual interconnected network of NPs and pores, which allows for the direct exchange between dications with similar solubility to occur, contrary to what we and others have observed in ligand-capped metal chalcogenide NPs or in xerogels, where the pore structure is partially collapsed. The speed of the reaction correlates with the difference in reduction potential of the incoming versus the outgoing cation (Ag^{+}, Pb^{2+} and Hg^{2+} exchange very fast, while Cd^{2+} is slow and only partial exchange occurs under the same mild reaction

conditions). There was no correlation observed between the size or size to charge ratio of the exchanging cation and the speed of the reaction.

The complete conversion of ZnS to $CuInS_2$ was not achieved under reaction conditions identical with those used for the exchange with Pb^{2+}, Ag^{+}, and Cd^{2+}, due to the slow kinetics of the In^{3+} cation —the reduction potential of In^{3+} (– 0.338 V) is similar to that of Cd^{2+}— whereas Cu^{+} exchanges much faster (E^0 = +0.520 V). An investigation into modifying the reaction conditions (using a different Cu^{+} precursor, solution pH, different solvents) to achieve the complete conversion might provide better control into the completion of the reaction, as well as the control of the desired phase. Nevertheless, combining ZnS and $CuInS_2$ NPs in various ratios has been reported to yield materials with bandgaps that span the entire visible spectrum, thus the incomplete exchange observed to date may prove beneficial for tuning the optical properties.[127, 128] The absorbance characteristics observed in NP systems, combined with the 3D interconnectivity inherent to aerogels, could open the door for accessing a series of materials with enhanced efficiency towards PV devices (where electronic transport throughout the network— which is facilitated by the interparticle connectivity— is paramount).

CHAPTER 5

HEAVY METAL WATER REMEDIATION USING ZnS GELS AS AN ION EXCHANGER

5.1 Introduction

The dissertation research analyzes the suitability of ZnS NP gel networks for use as heavy metal remediation materials via the easy cation-exchange chemistry previously demonstrated in our group for CdSe systems.[78] The cation exchange process occurring in the soft metal sulfide aerogels, combined with the high porosity and high surface area inherent to aerogels, should allow for increased heavy metal removal capacities when compared to the reported oxidic and even layered sulfide materials, where most of the removal occurs through chemisorption to the accessible surface. Indeed, chalcogenide aerogels based on molecular frameworks have been proven suitable for remediation.[62] However, the efficacy of their NP aerogel cousins has yet to be tested.

A schematic representation of the proposed heavy metal water remediation protocol is shown in Figure 1.3. Assuming that the cation exchange process will occur in a mole–to–mole ratio, a theoretical capacity of 2127 mg Pb/ g ZnS aerogel (10.3 mmol/ g) is predicted. This is almost an order of magnitude higher than the highest capacities reported to date, 331 mg/g (1.6 mmol/g) for a zinc sulfide chalcogel[62] or 365 mg/g (1.8 mmol/g) for thiol functionalized oxidic materials.[85]

5.2 Experimental

All the chemicals used in this chapter are listed in Chapter 2, Section 2.1. The synthesis of the ZnS NPs, gels and aerogels, and the cation exchange reaction with Pb^{2+}, Cd^{2+} and Hg^{2+} were described in Chapter 4, Sections 4.2.1 and 4.2.2.

5.2.1 Quantitative heavy metal uptake studies

The heavy metal uptake from solutions of various concentrations was determined using the batch method at $V/m \sim 1{,}000$ mL solution / 1 g solid exchanger, where V is the solution volume in mL and m is the mass of the ZnS solid exchanger used, in grams. In a typical experiment, 10 mL aqueous (HPLC grade water) solutions of the heavy metal of interest (i.e. Pb^{2+}, Hg^{2+}) of various initial concentrations was added to 10 mg of ZnS aerogel or xerogel. The mixture was kept undisturbed or stirred at room temperature for a specific time. The mixture was then centrifuged and an aliquot of solution taken out carefully, to avoid removing solid particles. The aliquots were then diluted with 2% nitric acid in HPLC grade water and the heavy metal content was analyzed using ICP-MS. Competitive ion exchange experiments were also performed using the batch method with a V/m ratio of 1000 mL/g, at room temperature and a contact time of 24 hours. Competing ions (i.e. Na^{+}, Ca^{2+}, and Mg^{2+}) were added in a 1000 fold excess to the heavy metal tested (1 M competing ion vs. 1 mM heavy metal ion) and the experiments were carried out the same as described above. The material was also tested using tap water that was spiked with the heavy metal ion of interest, to mimic more real-life conditions. For each sample, a control test without adsorbent was also conducted, to normalize for possible metal precipitation.

The affinity and selectivity of the ZnS material for the heavy metal ion tested is expressed using the distribution coefficient K_d, calculated using the equation $K_d = (V/m)\cdot[(C_0-C_f)/(C_f)]$, where C_0 and C_f are the initial and final metal ion concentrations (ppm or ppb), V is the testing solution volume (mL) and m is the amount of solid exchanger (g) used in the experiment. Also, the capacity, q_e, of the aerogel for heavy metal removal was calculated using the equation $q_e = (V/m)(C_0 - C_f)$, with the variables defined the same as above, but with C_0 and C_f expressed in ppm, and V expressed in L.

5.2.2 Inductively-coupled Plasma Mass Spectrometry (ICP-MS) measurements

Metal concentrations were measured using a Perkin-Elmer Life Sciences Elan 9000 instrument equipped with an automatic sampler. The data were collected as counts per second. A standard external calibration curve was constructed by diluting stock solutions of 1000 ppm standards (High-Purity Standards) with 2% HNO_3 in HPLC grade water. Four calibration standards from 1 to 20 ppb were prepared. The calibration curves were linear, with less than 0.1% deviation. The samples were also diluted before measurement with 2% HNO_3 to concentrations within the calibration range and the concentrations of the targeted heavy metals were measured before and after treatment with the ZnS aerogel. Isotopes ^{208}Pb, ^{202}Hg, ^{64}Zn and ^{66}Zn were analyzed. For each sample, three readings of the ICP-MS intensity were recorded and averaged. Standards were measured before and after the samples to analyze for instrument drift. Blank samples were analyzed periodically between samples, to check for sampling probe contamination.

5.2.3 Error determination

The weight of the ZnS aerogel used for the heavy metal remediation was determined using an analytical balance with ± 0.1 mg precision. In a typical experiment, the amount of ZnS aerogel used was between 5 and 11 mg. This introduced an error of approximately 2% in the final calculation of capacity and distribution coefficient.

The samples collected after the heavy metal remediation experiments needed to be diluted using multi-step dilution to the low ppb levels required by the ICP-MS analytical technique used. The dilution skill of the human operator was determined by preparing duplicate samples of each collected sample. The samples were than separately analyzed, and the results reported as an average value and standard deviation.

The instrument error or drift over time was also determined by analyzing the same samples twice over a few hours' interval. The experiment was repeated at least twice for each initial heavy metal concentration and the results were then reported as the average value of the measurements and standard deviation.

5.3 Quantitative estimation of Pb^{2+} removal from aqueous solutions by ZnS aerogels

The qualitative study described in Chapter 4 indicated that the ZnS gels should be suitable for the removal of both Pb^{2+} and Hg^{2+} ions from contaminated solutions. Therefore, I conducted a quantitative study of the material's removal efficiency, focusing on aqueous Pb^{2+} solutions. Briefly, I treated ZnS aerogels with solutions containing different concentrations of heavy metal ranging from 20,000 ppm to 10 ppb, and measured the metal concentrations before and after treatment using ICP-MS. The ratio of

heavy metal contaminated solution to ZnS aerogel was kept constant at 1000 mL solution/ 1 g aerogel for all experiments.

The measure of the ZnS aerogel's affinity for the heavy metal ion was gauged by calculating the distribution coefficient, K_d. K_d measures the exchanging material's capacity to partition the heavy metal between the solution and the aerogel; values larger than 500 mL/g are considered acceptable, those above 5000 mL/g are very good, and those above 50,000 mL/g are considered outstanding.[129]

There are three distinct behaviors corresponding to low, medium, and high Pb^{2+} concentrations as a result of the exchange thermodynamics. Considering the overall cation exchange reaction:

(1) $$ZnS_{(s)} + Pb^{2+}_{(aq)} \leftrightarrow PbS_{(s)} + Zn^{2+}_{(aq)},$$

it can be thought of thermodynamically as the combination of the solubilization processes

(2) $$ZnS_{(s)} \leftrightarrow Zn^{2+}_{(aq)} + S^{2-}_{(aq)} \qquad K_{sp} = 3 \times 10^{-23}$$

and (3) $$PbS_{(s)} \leftrightarrow Pb^{2+}_{(aq)} + S^{2-}_{(aq)} \qquad K_{sp} = 3 \times 10^{-28}$$

Thermodynamically, (1) = (2) – (3) and the equilibrium constant (K) for the cation exchange process can be derived from the solubility product constants for ZnS and PbS: $K = K_{sp\ ZnS} / K_{sp\ PbS} = 1.0 \times 10^5$. At low, non-forcing Pb^{2+} concentrations (10-100 ppb), the equilibrium is limited by the native solubility of ZnS. At medium concentrations (20-200 ppm), ZnS solubility is no longer limiting and the equilibrium is more favorable for PbS formation. Finally, at high concentrations (2000-20,000 ppm), the equilibrium is forced strongly to the right, and the native solubility of PbS becomes limiting.

5.3.1 Initial concentrations ranging from 10 to 100 ppb

The ZnS aerogel is very effective at removing lead ions from solutions with low initial concentrations (up to 100 ppb Pb^{2+}), decreasing the concentration below the EPA recommended action level of 15 ppb Pb^{2+} (Table 5.1, Figure 5.2). This initial concentration range is a good mimic for an actual environmental spill, where large volumes of dilute solutions must be treated. The K_d values obtained are in the "very good" range, since the low initial concentrations are not creating thermodynamically driving conditions. However, the low final concentrations attained are encouraging for the use of ZnS aerogels in remediation.

Table 5.1. Initial (10–100 ppb) and final concentrations, percent removal and distribution coefficient K_d (error represents instrument accuracy)

Initial Pb^{2+} concentration (ppb)	Final Pb^{2+} concentration (ppb)	Amount of Pb^{2+} removed (mmol)	Amount of Zn^{2+} liberated (mmol)	Removal (%)	K_d (mL/g)
97.08 ± 0.03 [(a)]	12.24 ± 0.06	0.0041	n/a	87.3	7.27×10^3
93.47 ± 0.25	9.08 ± 0.18	0.0041	n/a	90.1	9.13×10^3
10.15 ± 0.15	1.49 ± 0.07	0.00042	n/a	84.9	6.49×10^3

(a) sample was not stirred.

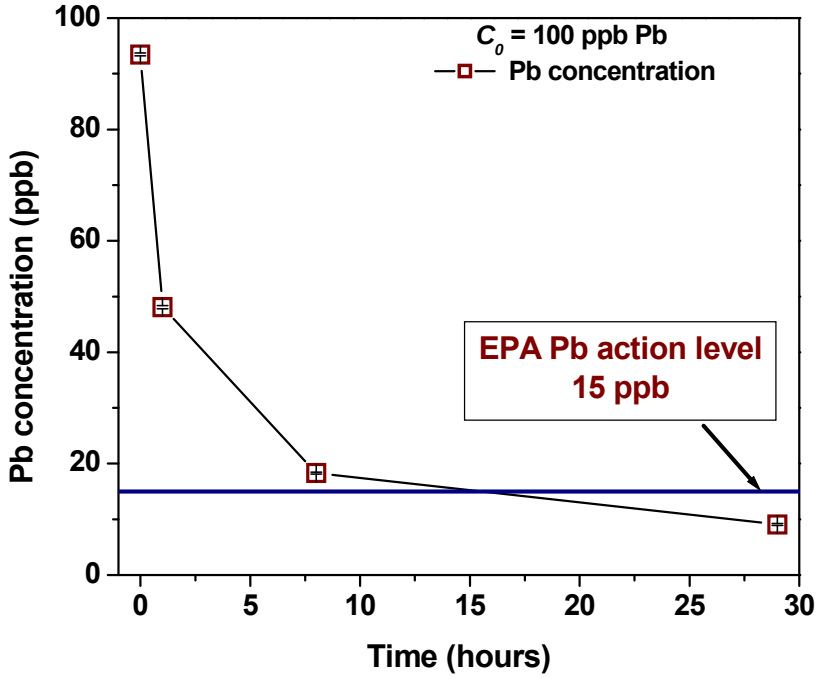

Figure 5.1. Decrease of Pb^{2+} concentration with time for an initial concentration of 100 ppb

5.3.2 Initial concentrations ranging from 20 to 200 ppm

In the initial concentration range from 20 to 200 ppm, the forward reaction equilibrium is favored and the ZnS aerogel proved to be the most efficient (of all concentrations studied) in removing Pb^{2+} ions from aqueous solutions (Table 5.2, Figure 5.3), showing "very good" to "excellent" K_d values ranging from 17,200 to 72,300 mL/g for Pb^{2+}. Nearly all of the Pb^{2+} can be removed ($\geq$ 95%), but the more forcing conditions result in higher final Pb^{2+} concentrations (>50 ppb).

Table 5.2. Initial (20–200 ppm) and final concentrations, percent removal and distribution coefficient K_d (error represents dilution accuracy)

Initial Pb^{2+} concentration (ppm)	Final Pb^{2+} concentration (ppm)	Amount of Pb^{2+} removed (μmol)	Amount of Zn^{2+} liberated (μmol)	Removal (%)	K_d (mL/g)
171 ± 15 [a)]	9.86 ± 0.3	6.45	9.14	94.5	1.72×10^4
171 ± 15	3.61 ± 0.1	7.27	11.5	98.1	5.05×10^4
13.80 ± 1.09	0.189 ± 0.01	0.545	1.65	98.6	7.23×10^4
1.26 ± 0.10	0.066 ± 0.007	0.0450	2.35	95.5	2.14×10^4

a) sample was not stirred.

For similar initial Pb^{2+} concentrations, stirring the solution during the exchange contributed to a mere 3-4% increase in the percent removal (see first entry in Tables 5.1 and 5.2). This is an indication that, for all practical purposes, stirring the samples is not required.

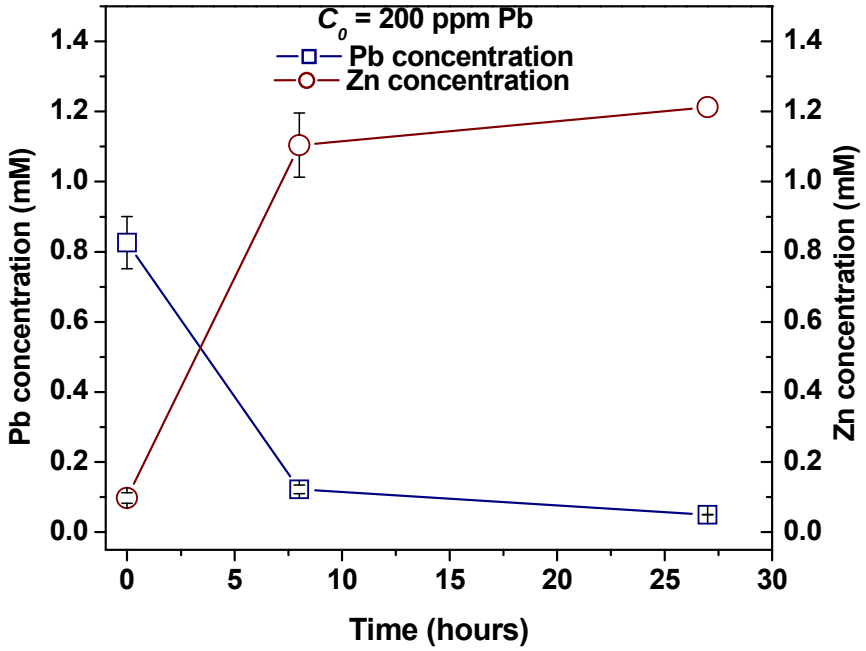

Figure 5.2. Decrease of Pb^{2+} and increase of Zn^{2+} concentrations as a function of contact time (error bars represent dilution accuracy). The concentrations have been converted to molarity to aid in gauging the cation exchange magnitude

5.3.3. Initial concentrations ranging from 2000 to 20000 ppm;

With initial Pb^{2+} concentrations higher (i.e. 1.5 fold Pb^{2+} excess) than the saturation value for the amount of ZnS aerogel used (if mole to mole exchange occurs) the aerogel exhibits a removal capacity of 1730 ± 90 mg Pb / g ZnS exchanger, which is much higher than the previously reported capacities of 331 mg/g for a zinc tin sulfide chalcogel[62] or 365 mg/g for thiol functionalized oxidic materials,[85] and close to the theoretical capacity of 2127 mg Pb/ g ZnS. If the equilibrium is pushed to the right by the use of higher excess Pb^{2+} (i.e. 5- or 10-fold) , see Table 5.3, even higher capacities can be reached. The fact that the measured capacities are higher than that theoretically calculated

based solely on exchange suggests that Pb^{2+} is also being chemisorbed to the aerogel surface, perhaps by residual thiol groups that are still present. Under these strongly forcing conditions, the concentration of Pb^{2+} is largely governed by the PbS solubility constant and it is no longer useful to compare K_d values.

5.4 Ion-exchange mechanism

In order to discern whether the ion remediation was occurring by exchange, the Zn^{2+} concentration was also monitored. The heavy metal ion concentration decreases while the Zn^{2+} concentration increases, supporting the fact that the removal is occurring via an ion-exchange mechanism, and not merely by physisorbtion or chemisorption to surface thiol groups. Typical curves obtained are shown in Figure 5.3. When the initial concentration of the exchanging ion is low (below full capacity of the ZnS aerogel), the moles of released zinc are higher than those of lead removed (Table 5.2). The observed formation of the PbS phase by PXRD (Chapter 4, Figure 4.8) indicates that the cation exchange reaction does take place, so we attribute this slight Zn^{2+} excess to the dissolution of the ZnS aerogel. At the same time, there is also the possibility of a slight ZnS NP contamination due to the breakdown of the gel network. When the initial concentration is at or above full exchange capacity, the zinc is completely replaced and the number of moles is always lower than the incoming lead (see Table 5.3). Nevertheless, the amount of Zn^{2+} ions liberated during the process is almost constant and within the range expected for the complete exchange with Pb^{2+} (0.056 mmol ZnS were used for the experiment), which indicates that the ion exchange occurs preferentially over chemisorption of Pb^{2+}. A similar observation of Pb^{2+} being absorbed above the cation

exchange capacity of the material was noticed with the mineral montmorillonite[83] and was explained by the formation of small Pb NPs at the surface and edges of the crystallites. However, we found no evidence of Pb formation, either in TEM, or by PXRD (see Figures 4.8 and 4.9).

Table 5.3. Removal capacity and amounts of Pb^{2+} removed and Zn^{2+} liberated when using 0.056 mmol ZnS aerogel with solutions with different initial Pb^{2+} concentrations (2000–20,000 ppm)

Initial Pb^{2+} concentration (ppm)	Amount of Pb^{2+} removed (mmol)	Amount of Zn^{2+} liberated (mmol)	Removal capacity (mg Pb/ g ZnS)	Removal capacity (mmol Pb/ g ZnS)
24600 ± 320	0.078 ± 0.007	0.041 ± 0.009	2950 ± 270	14.2 ± 1.3
12000 ± 150	0.071 ± 0.003	0.050 ± 0.010	2680 ± 120	12.9 ± 0.58
2320 ± 27	0.046 ± 0.002	0.031 ± 0.022	1730 ± 90	8.35 ± 0.43

5.5 Effect of competing ions/porosity on removal efficacy;

When competing ions such as Na^{+}, Ca^{2+} or Mg^{2+} —which can be expected to be present in real world samples— are present in large excess (i.e. 1M competing ion vs. ~1 mM Pb^{2+}), the K_d decreases by one order of magnitude (Table 5.4). This phenomenon has been previously observed in a layered potassium manganese tin sulfide material.[88] The reason for the decrease could be the creation of electrostatic repulsion forces between the ZnS aerogel surface and the incoming cation, due to the increase in the solution's activity at these high concentrations. Nevertheless, the ZnS aerogel still showed Pb^{2+} removal of

74% in the presence of Mg^{2+}, 85% in the presence of Ca^{2+}, and 92% in the presence of Na^{+}, indicative of the strong material preference for heavy, soft cations.

ZnS xerogels (bench-top-dried, low porosity and surface area gels) show almost no ability to undergo cation exchange (K_d = 6.7 for 20 ppm Pb^{2+} solution). A recent report[130] indicates that, even though xerogels still maintain some porosity after drying, most of the pores are occluded, and thus inaccessible to reactants, behaving more like the bulk material. The observation of the suppressed heavy metal removal capability underscores the importance of accessible pores to the effectiveness of the cation exchange reaction

Table 5.4. Distribution coefficients for Pb^{2+} in the presence of competing ions

Initial Pb^{2+} concentration (ppm)	Competing ion and concentration (M)	K_d for Pb (mL/g)	Previous report*[88] K_d (mL/g)
172	None	2.35×10^4	$1.1–8.9 \times 10^5$
172	Na^{+} (1M)	1.11×10^4	8.34×10^4
176	Ca^{2+} (1M)	5.58×10^3	1.88×10^4
173	Mg^{2+} (1M)	2.91×10^3	n/a

***** In the previous report[88] K_d values were obtained by treating a layered potassium manganese sulfide with a slightly more forcing initial Pb^{2+} concentration (~ 300 ppm) and a slightly lower V/m ratio (~ 900 mL/g) than the ones used here.

5.6 Effect of "real-life" samples on removal efficacy;

The ZnS aerogel materials were also tested under "real-life" conditions, by treating tap water spiked with Pb^{2+} ions, to mimic a hypothetic contamination occurrence. After a 24 hour contact period, the material showed similar behavior as in HPLC grade water (Table 5.5) removing more than 90% of the contaminant from solutions with initial concentrations ranging from 200 ppb to 200 ppm.

Table 5.5. Percent removal and K_d values for tap water spiked with different Pb^{2+} concentrations

Initial Pb^{2+} concentration (ppm)	Final Pb^{2+} concentration (ppm)	Removal after 24 hours (%)	K_d value (mL/g)
196	2.99	98.5	6.47×10^4
14.7	1.17	92.0	1.15×10^4
0.253	0.013	94.8	1.80×10^4

5.7 Quantitative study of Hg^{2+} removal ability;

A less detailed study was conducted on the ability of ZnS aerogels to remove Hg^{2+} from aqueous solutions. Briefly, the batch method was employed using aqueous solutions with initial concentrations ranging from 200 ppm to 200 ppb. Based on the observation that the Hg^{2+} exchange occurs faster, made during the qualitative study (Table 4.2), samples were collected after 30 minutes, 1 and 3 hours (Figure 5.4).

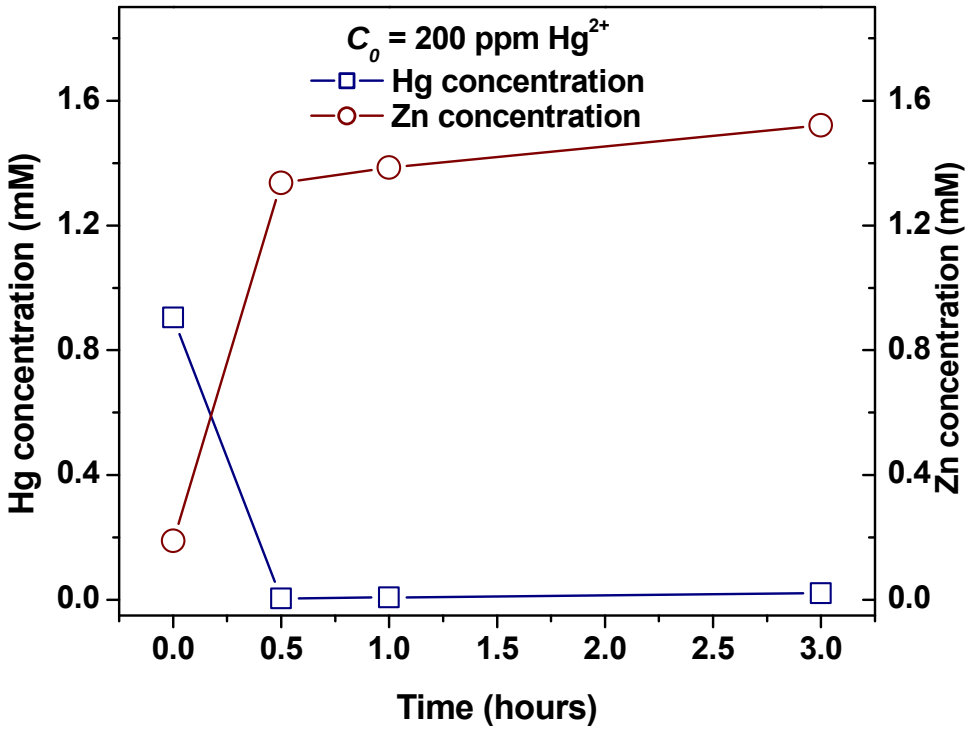

Figure 5.3. Decrease of Hg^{2+} and increase of Zn^{2+} concentrations as a function of contact time

The equilibrium concentration is reached within 30 minutes, confirming the observed reaction speed trend. Even higher partition abilities than for the case of Pb^{2+} were observed (K_d values from 5.59 x 10^4 to 2.05 x 10^5 mL/g), as expected from the softer acid character of Hg^{2+}. Moreover, the presence of competing Ca^{2+} ions does not seem to affect the Hg^{2+} removal ability of the ZnS aerogel, probably also a result of the faster kinetics (Table 5.6). A previous report[62] on a zinc tin sulfide chalcogel material has reported K_d values between 1.62 x 10^6 and 1.12 x 10^8 for the removal of Hg^{2+}, albeit using a higher volume to mass ratio (10,000 mL solution / g exchanger) and a lower

initial Hg^{2+} concentration (100 ppm), which can affect the equilibrium behavior and thus preclude a direct comparison.

Table 5.6. Hg^{2+} removal ability for initial concentrations of 200 ppm and 200 ppb, and in the presence of excess Ca^{2+} (the maximum contaminant level in drinking water allowed by the EPA is 2 ppb Hg)

Initial Hg^{2+} concentration (ppb)	Final Hg^{2+} concentration (ppb)	Contact time (hours)	K_d value (mL/g)
1.82×10^5	$(5.01 \pm 0.80) \times 10^3$	3	1.95×10^5
329	5.99 ± 0.20	3	5.59×10^4
2.57×10^5 (1 M Ca^{2+})	1.25×10^3	24	2.05×10^5

5.8 Conclusions

The quantitative study revealed that the ZnS aerogel shows the highest capacity reported to date (14.2 mmol/g) for the removal of Pb^{2+} from aqueous solutions. Distribution coefficient measurements indicate that the material is more efficient with initial Pb^{2+} concentrations in the 20–200 ppm range. This is expected, since this is an equilibrium reaction and the balance between thermodynamic and kinetic factors changes as the initial concentrations approach the solubility of the cationic species. Nevertheless, with initial concentrations around 100 ppb, the ZnS aerogels reduce the lead concentration below the 15 ppb Pb action level recommended by the EPA. In the presence of competing ions, a one order of magnitude decrease in the distribution

coefficients is observed, but the percent removal is still more than adequate. Finally, the material shows similar efficiency in "real-life conditions" (i.e. tap water spiked with lead ion contaminant), suggesting the real possibility of use for water remediation applications.

The K_d values measured for the lead remediation are similar to those previously reported using the zinc tin sulfide chalcogel[62]; the same report measured higher K_d values for mercury. Their experimental conditions were different (they used 10,000 mL solution/ g exchanger, compared to 1,000 mL/g used in the dissertation research) and a direct comparison is not entirely possible. Another report[88] that tested layered potassium manganese sulfides using the same V/m ratio as us measured K_d values closer to those we report for ZnS aerogels. Nevertheless, the observed overall capacity exhibited by the ZnS aerogel exceeds all the other previous reports.

The high lead removal capacity demonstrated by the intrinsically soft Lewis basic ZnS aerogels makes them promising for applications as fixed bed metal removal materials. Finally, I note that the distribution coefficient values might be improved upon lowering the pH of the contaminant-containing solution, as was previously observed by other groups.[88] Also, I surmise that the reason for the lower than expected K_d values may reside in the less accessible micropores present in the aerogel networks. This is most obvious when lower contaminant concentrations are used, and the concentration gradient is not large enough to push the equilibrium to completion.

CHAPTER 6

CONCLUSIONS AND PROSPECTUS

6.1 Conclusions

One of the challenges presented to the emerging field of nanotechnology is the ability to transfer the properties of individual nanoparticles (NPs) to assemblies that are easily handleable and amenable for device fabrication, while still maintaining the unique properties characteristic to the individual NP building blocks. Various approaches have been used to this effect, some more effective than others in terms of cost and/or final material properties. Our group has used sol-gel chemistry as a means to assemble semiconducting metal chalcogenide NPs such as CdSe, CdS, CdTe, ZnS, PbS, PbTe into 3D gel networks.[22, 35, 66, 71, 93, 131] This approach consists of the initial NP synthesis, followed by controlled oxidative assembly of the NPs into wet gels and supercritical drying to yield aerogels. The resulting materials consist of a dual interconnected 3D network of NPs and pores that exhibits a high surface area and maintains the quantum confined properties of the semiconducting NP building blocks. These characteristics make these materials good candidates for applications that require easily accessible, large surface areas (catalysis, sensing), or continuous pathways for charge transport (photovoltaics, thermoelectrics).

This dissertation was focused on the synthesis, characterization and application of metal chalcogenide gel networks. The main goals were to (1) investigate the mechanism of metal chalcogenide NP gel formation, (2) extend the cation exchange reactions to ZnS gels for generating new aerogel materials and understanding the driving forces of the

process, and (3) conduct a quantitative study on the ability of ZnS aerogels to remove harmful heavy metals from aqueous solutions, using the same facile cation exchange reactions.

In the dissertation research, the nature of the forces holding the metal chalcogenide gel networks together was probed by looking at chemical changes that occur during the sol-gel process. Previous Raman studies[94] of CdSe gels indicated that Se–Se covalent bonds are present in the gel network and might be responsible for the interparticle linkage, and that the addition of an appropriate reducing agent is able to cleave these bonds, re-generating the NP sol. Also, it was noted that the gelation-dispersion process is cyclable, and a decrease in the primary particle size upon successive cycles was observed by PXRD, TEM and UV-Vis measurements.

In Chaper 3, I tested the proposed hypothesis by probing the presence of covalent selenide or polyselenide species by XPS. Analysis of the thiolate-capped CdSe NPs and the corresponding gel networks indicates that the selenium species present on the surface changes to a more oxidized species upon gelation, and the shift was consistent with the formation of polyselenide species, thus strengthening the previous observation made in Raman. At the same time, a pure reducing agent, $NaBH_4$, was successfully used to break the interparticle bonds, enabling the clear distinction between the dual reducing/ligating role of the thiolates used for the dispersion of the gel networks. The fact that species with reducing character are able to cleave the gel network, while those with Lewis base ligating character were not, strengthened the proposed oxidative/reductive mechanism for the gel formation/dispersion. Consistent with the proposed mechanism, the successive gelation/dispersion cycles result in surface etching of metal and chalcogenide species,

yielding smaller particles. This trend was observed in the case of CdS NP gels, extending the initial observation in CdSe materials, and allowed for the proposition that the gelation mechanism applies beyond CdSe to CdS, i.e., to other metal chalcogenides, such as ZnS, PbS or CdTe.

The ability of metal chalcogenide NP monolithic gel networks to undergo facile cation exchange reactions while maintaining the integrity of the 3D network was demonstrated recently.[78] This report was an extension of previous studies[74, 75, 116] that brought forth the ability of metal chalcogenide NPs to surmount the activation energy barriers present in dense 3D bulk materials and participate in easy cation exchange. The observed extension of the fast cation exchange to CdSe gel networks has presented the opportunity of accessing new aerogel materials from already-constructed ones, without the need for independent optimization of the NP synthesis and gelation processes.

In Chapter 4 of the dissertation research, the cation exchange reaction was extended to ZnS gel networks, with the aim of accessing new sulfide aerogel chemistries and of better understanding the factors that control the exchange process in the porous, 3D structures. The exchange does occur under the same mild reaction conditions (room temperature, methanol or methanol/water solvent) previously observed for CdSe gels. Ag_2S and Ag NP-decorated Ag_2S gels were accessed by exchanging Ag^+ for Zn^{2+}, and controlling the reaction time and exposure to light. The interplay between thermodynamic and kinetic driving forces for the reaction was gauged by analyzing the exchange with two ions that have similar thermodynamic driving forces, namely Pb^{2+} and Cd^{2+}. The exchange occurs at very different rates (minutes for Pb^{2+} and days for Cd^{2+}) which is an indication that, for the experimental conditions used, the difference in solubility is not the

driving force governing the overall cation exchange reaction speed. The trend observed for the ZnS aerogel cation exchange speed has been observed previously[76] for the cation exchange of ZnS thin films. A correlation exists between the difference between the reduction potential of the incoming cation and that of Zn^{2+}: the larger the difference, the faster the exchange. The correlation is present in the ZnS gel networks tested here and it was further confirmed by the fast exchange with Cu^{2+} and Hg^{2+}, both of which have more positive reduction potentials when compared to that of Zn^{2+}.

The simultaneous cation exchange with Cu^{+} and In^{3+} resulted in quaternary ZnS-$CuInS_2$ gels. Under the same mild reaction conditions, the complete conversion of ZnS to $CuInS_2$ was not achieved, probably due to the very different mobility of Cu^{+} and In^{3+}. Controlling the speed of the reaction by using different cation precursor species, solvent systems or even reaction temperature, is a possible avenue towards accessing this particular phase, which is also desirable as a 3D connected NP network for photovoltaic applications, due to the fact that the emission spectrum can be tuned throughout the visible spectrum.[127]

The observed ability of ZnS gel networks to undergo facile cation exchange reactions indicated the possibility of using them as heavy metal remediation materials. The intrinsic soft Lewis basic character of the sulfide framework should show increased affinity and selectivity for the removal of soft heavy metals, when compared to the traditionally used oxidic porous materials. Indeed, as presented in Chapter 5, upon treating ZnS aerogels with Pb^{2+} aqueous solutions under thermodynamically forcing conditions (10 fold heavy metal ion excess), a removal capacity of 14.2 mmol Pb/ g ZnS aerogel was measured, which is the highest reported to date, and almost one order of

magnitude higher than previous reports.[62] Also, when treating ZnS aerogels with low initial concentrations mimicking an actual environmental spill (i.e. ~100 ppb Pb^{2+}), final concentrations below the EPA recommended action level of 15 ppb Pb were achieved. In the intermediate initial concentration range (20–200 ppm Pb^{2+}), excellent distribution coefficient values between 2.14 and 7.23 x 10^4 mL/g were measured. The distribution coefficients decrease by one order of magnitude in the presence of competing ions in high excess (1000 fold), but the percent removal of Pb^{2+} is still adequate (74%, 85% or 92% in the presence of Mg^{2+}, Ca^{2+} or Na^{+}, respectively). The ZnS aerogel is just as efficient in removing Pb^{2+} under real-life conditions (using heavy metal spiked tap water, as opposed to HPLC water). The study also revealed that stirring the sample only improves the percent removal by a mere 3–4%, and that having an accessible porous network is paramount for achieving the high removal capacity. The removal of Hg^{2+} occurs even faster than that of Pb^{2+}, consistent with the qualitative observation made in Chapter 4, and excellent distribution coefficients between 5.59 x 10^4 and 2.05 x 10^5 mL/g were measured. Overall, the high heavy metal removal capacity exhibited by the ZnS aerogels makes them suitable candidates for incorporation into water remediation filters.

6.2 Prospectus

The metal chalcogenide NP gel networks developed in our lab using the sol-gel process provide a link that extends the size-dependent and tunable properties of individual semiconducting NPs into the device-amenable area of 3D structures. Understanding the transport properties of the gel networks and correlating them with their intrinsic compositional, morphologic and structural characteristics, requires a thorough

understanding of the exact chemical nature of such systems. The presence of an anionic network connecting the particles together into 3D structures is beneficial for applications in cation exchange reactions. Also, considering electronic transport through the gel network, a systematic study of such transport properties might provide even more insight into the nature of the selenide species present and their effect on the overall properties of the gel network.

The distribution coefficient values might be further improved if the pH of the contaminated solution is decreased slightly, as it was previously noted in another report.[88] A similar increase might occur by using wet gels instead of aerogels as the exchange materials. Also, we surmise that the reason for the lower than expected K_d values may reside in the less accessible micropores present in the aerogel networks. This is most obvious when lower contaminant concentrations are used, and the concentration gradient is not large enough to push the equilibrium to completion. We hypothesize that the distribution coefficient values will be improved upon switching to a system composed mainly of meso- and macropores, one that would allow even better and faster access to the surface of the material (i.e. growing the ZnS gel network on the fibers of a porous silica paper, similar to previous reports for RuO_2 materials[132]).

For the generation of the ternary $CuInS_2$ aerogel, a step-wise approach similar to that reported elsewhere[121] and that takes advantage of the selective solubility of cations with various charges, might prove useful. For example, using a methanolic solution of tetrakisacetonitrilecopper(I) hexafluorophosphate as the copper ion source might provide a slower, more controlled cation exchange that might result in a single Cu_xS_y stoichiometry. Once this is achieved, using stoichiometric or only slight excess of In^{3+}

dissolved in a tri-n-butylphosphine (TBP)-methanol mixture could effect the controlled exchange for the final $CuInS_2$ composition. This step should take advantage of the fact that TBP has a stronger binding affinity to the monovalent Cu^+ when compared to divalent or trivalent cations, and might allow for the removal of Cu^+ and the replacement with In^{3+}. Considering the overall scope of the study, that of providing an easy way of achieving these new and interesting aerogel materials while avoiding new optimization procedures, the balance between the possibility of achieving the desired material and the practicality of the procedure, must be carefully considered.

REFERENCES

1. West, A. R., *Basic Solid State Chemistry* 2nd ed.; John Wiley & Sons Ltd.: New York, 1999.

2. Trindale, T. O.; O'Brien, P.; Pickett, N. L., *Chem. Mater.* **2001,** *13*, 3843-3858.

3. Steigerwald, M. L.; Brus, L. E., *Acc. Chem. Res.* **1990,** *23*, 183-188.

4. Brus, L. E., *J. Chem. Phys.* **1984,** *80*, 4403.

5. Brus, L. E., *J. Chem. Phys.* **1983,** *79*, 5566.

6. Michalet, X.; Pinaud, F. F.; Bentolila, L. A.; Tsay, J. M.; Doose, S.; Li, J. J.; Sundaresan, G.; Wu, A. M.; Gambhir, S. S.; Weiss, S., *Science* **2005,** *307*, 538-544.

7. Gur, I.; Fromer, N. A.; Geier, M. L.; Alivisatos, A. P., *Science* **2005,** *310*, 462-465.

8. Huynh, W. U.; Dittmer, J. J.; Alivisatos, A. P., *Science* **2002,** *295*, 2425-2427.

9. Liu, J.; Tanaka, T.; Sivula, K.; Alivisatos, A. P.; Fréchet, J. M. J., *J. Am. Chem. Soc.* **2004,** *126*, 6550-6551.

10. Sun, B.; Marx, E.; Greenham, N. C., *Nano Lett.* **2003,** *3*, 961-963.

11. Konstantatos, G.; Howard, I.; Fischer, A.; Hoogland, S.; Clifford, J.; Klem, E.; Levina, L.; Sargent, E. H., *Nature* **2006,** *442*, 180-183.

12. Ivanisevic, A.; Reynolds, M. F.; Burstyn, J. N.; Ellis, A. B., *J. Am. Chem. Soc.* **2000,** *122*, 3731-3738.

13. Meeker, K.; Ellis, A. B., *J. Phys. Chem. B* **1999,** *103*, 995-1001.

14. Nazzal, A. Y.; Lianhua, Q.; Peng, X.; Xiao, M., *Nano Lett.* **2003,** *3*, 819-822.

15. Scholes, G. D., *Adv. Funct. Mater.* **2008,** *18*, 1157-1172.

16. Yin, Y.; Alivasatos, A. P., *Nature* **2005,** *437*, 664-670.

17. Alivisatos, A. P., *Science* **1996,** *271*, 933-937.

18. Rossetti, R.; Brus, L. E., *J. Phys. Chem.* **1982,** *86*, 4470-4472.

19. Meyer, M.; Wallberg, C.; Kurihara, K.; Fendler, J. H., *J. Chem. Soc., Chem. Commun.* **1984,** (2), 90-91.

20. Fendler, J. H., *Chem. Rev.* **1987,** *87* (5), 877-899.

21. Steigerwald, M. L.; Alivisatos, A. P.; Gibson, J. M.; Harris, T. D.; Kortan, R.; Muller, A. J.; Thayer, A. M.; Duncan, T. M.; Douglass, D. C.; Brus, L. E., *J. Am. Chem. Soc.* **1988,** *110* (10), 3046-3050.

22. Mohanan, J. L.; Arachchige, I. U.; Brock, S. L., *Science* **2005,** *307*, 397-400.

23. Trindade, T. O.; O'Brien, P.; Pickett, N. L., *Chem. Mater.* **2001,** *13*, 3843-3858.

24. Gacoin, T.; Malier, L.; Boilot, J.-P., *Chem. Mater.* **1997,** *9*, 1502-1504.

25. Mohanan, J. L.; Brock, S. L., *J. Sol-Gel Sci. Technol.* **2006,** *40*, 341-350.

26. Gacoin, T.; Lahlil, K.; Larregaray, P.; Boilot, J.-P., *J. Phys. Chem. B* **2001,** *105*, 10228-10235.

27. Murray, C. B.; Norris, D. J.; Bawendi, M. G., *J. Am. Chem. Soc.* **1993,** *115*, 8706-8715.

28. Peng, X. G.; Wickham, J.; Alivisatos, A. P., *J. Am. Chem. Soc.* **1998,** *120*, 5343-5344.

29. Murray, C. B.; Kagan, C. R.; Bawendi, M. G., *Annu. Rev. Mater. Sci.* **2000,** *30*, 545-610.

30. Sugimoto, T., *Adv. Colloid Interface Sci.* **1987,** *28*, 65-108.

31. Pradhan, N.; Reifsnyder, D.; Xie, R. G.; Aldana, J.; Peng, X. G., *J. Am. Chem. Soc.* **2007,** *129*, 9500-9509.

32. Medintz, I. L.; Uyeda, H. T.; Goldman, E. R.; Mattoussi, H., *Nature Mater.* **2005,** *4*, 435-446.

33. Peng, Z. A.; Peng, X., *J. Am. Chem. Soc.* **2001,** *123*, 183-184.

34. Frame, A. F.; Carroll, E. C.; Larsen, D. S.; Sarahan, M.; Browning, N. D.; Osterloh, F. E., *Chem. Comm.* **2008**, 2206-2208.

35. Ganguly, S.; Brock, S. L., *J. Mater. Chem.* **2011,** *21* (24), 8800-8806.

36. Ganguly, S.; Zhou, C.; Morelli, D.; Sakamoto, J.; Uher, C.; Brock, S. L., *J. Solid State Chem.* **2011,** *184* (12), 3195-3201.

37. Manna, L.; Scher, E. C.; Li, L.; Alivasatos, A. P., *J. Am. Chem. Soc.* **2002,** *124*, 7136-7145.

38. Greenham, N. C.; Peng, X.; Alivisatos, A. P., *Phys. Rev. B* **1996,** *54*, 17628-17637.

39. Decher, G., *Ber. Bunsen-Ges.* **1991,** *95* (11), 1430.

40. Shavel, A.; Gaponik, N.; Eychmüller, A., *Eur. J. Inorg. Chem.* **2005**, 3613-3623.

41. Franzl, T.; Shavel, A.; Rogach, A. L.; Gaponik, N.; Klar, T. A.; Eychmueller, A., *Small* **2005,** *1*, 392-395.

42. Murray, C. B.; Kagan, C. R.; Bawendi, M., *Science* **1995,** *32*, 1335-1338.

43. Brinker, C. J.; Scherer, G. W., *Sol-Gel Science*. Academic Press: San Diego, 1990.

44. Rolison, D. R.; Dunn, B., *J. Mater. Chem.* **2001,** *11*, 963-980.

45. Hüsing, N.; Schubert, U., *Angew. Chem. Int. Ed.* **1998,** *37*, 22-45.

46. Pierre, A. C.; Pajonk, G. M., *Chem. Rev.* **2002,** *102*, 4243-4265.

47. Sriram, M. A.; Weil, K. S.; Kumta, P. N., *Appl. Organomet. Chem.* **1996,** *11*, 163-179.

48. Sriram, M. A.; Kumta, P. N., *J. Mater. Chem.* **1998,** *8*, 2441-2451.

49. Carmalt, C. J.; Dinnage, C. W.; Parkin, I. P.; White, A. J. P.; Williams, D. J., *Inorg. Chem.* **2002,** *41*, 3668-3672.

50. Allen, G. C.; Paul, M.; Dunleavy, M., *Adv. Mater.* **1992,** *4*, 424-427.

51. Purdy, A. P.; Berry, A. D.; George, C. F., *Inorg. Chem.* **1997,** *36*, 3370-3375.

52. Stanić, V.; Pierre, A. C.; Etsell, T. H., *J. Mater. Res.* **1996,** *11*, 363-372.

53. Stanić, V.; Etsell, T. H.; Pierre, A. C.; Mikula, R. J., *J. Mater. Chem.* **1997,** *7*, 105-107.

54. Stanić, V.; Etsell, T. H.; Pierre, A. C.; Mikula, R. J., *Mater. Lett.* **1997,** *31*, 35-38.

55. Stanić, V.; Pierre, A. C.; Etsell, T. H.; Mikula, R. J., *J. Non-Cryst. Solids* **1997,** *220*, 58-62.

56. Stanić, V.; Pierre, A. C.; Etsell, T. H.; Mikula, R. J., *J. Am. Ceram. Soc.* **2000,** *83*, 1790-1796.

57. Stanić, V.; Pierre, A. C.; Etsell, T. H.; Mikula, R. J., *J. Phys. Chem. A* **2001,** *105*, 6136-6143.

58. Kalebaila, K. K.; Georgiev, D. G.; Brock, S. L., *J. Non-Cryst. Solids* **2006,** *352*, 232-240.

59. Wachhold, M.; Rangan, K. K.; Billinge, S. J. L.; Petkov, V.; Heising, J.; Kanatzidis, M. G., *Adv. Mater.* **2000,** *12* (2), 85-91.

60. Bag, S.; Trikalitis, P. N.; Chupas, P. J.; Armatas, G. S.; Kanatzidis, M. G., *Science* **2007,** *317*, 490-493.

61. Bag, S.; Gaudette, A. F.; Bussell, M. E.; Kanatzidis, M. G., *Nat. Chem.* **2009,** *1* (3), 217-224, s217/1-s217/24.

62. Oh, Y.; Bag, S.; Malliakas, C. D.; Kanatzidis, M. G., *Chem. Mater.* **2011,** *23* (9), 2447-2456.

63. Gacoin, T.; Malier, L.; Boilot, J.-P., *J. Mater. Chem.* **1997,** *7*, 859-860.

64. Mohanan, J. L.; Brock, S. L., *J. Non-Cryst. Solids* **2004,** *350*, 1-8.

65. Yu, H.; Liu, Y.; Brock, S. L., *ACS Nano* **2009,** *3* (7), 2000-2006.

66. Arachchige, I. U.; Brock, S. L., *J. Am. Chem. Soc.* **2006,** *128* (24), 7964-7971.

67. Arachchige, I. U.; Brock, S. L., *J. Am. Chem. Soc.* **2007,** *129*, 1840-1841.

68. Yu, H.; Bellair, R.; Kannan, R. M.; Brock, S. L., *J. Am. Chem. Soc.* **2008,** *130* (15), 5054-5055.

69. Yu, H.; Brock, S. L., *ACS Nano* **2008,** *2* (8), 1563-1570.

70. Gaponik, N.; Wolf, A.; Marx, R.; Lesnyak, V.; Schilling, K.; Eychmueller, A., *Adv. Mater. (Weinheim, Ger.)* **2008,** *20* (22), 4257-4262.

71. Yao, Q.; Brock, S. L., *Inorg. Chem. (Washington, DC, U. S.)* **2011,** *50* (20), 9985-9992.

72. Yao, Q.; Brock, S. L., *Nanotechnol.* **2010,** *21* (11), 115502.

73. Fedorov, V. A.; Ganshin, V. A.; Korkishko, Y. N., *Phys. Stat. Sol.* **1993,** *139* (9), 9-65.

74. Wark, S. E.; Hsia, C.; Son, D. H., *J. Am. Chem. Soc.* **2008,** *130*, 9550-9555.

75. Son, D. H.; Hughes, S. M.; Yin, Y.; Paul Alivisatos, A., *Science* **2004,** *306* (5698), 1009-1012.

76. Engelken, R. D.; Ali, S.; Chang, L. N.; Brinkley, C.; Turner, K.; Hester, C., *Mater. Lett.* **1990,** *10* (6), 264-274.

77. Dloczik, L.; Lux-Steiner, M. C.; Koenenkamp, R., *Thin Solid Films* **2003,** *431-432*, 131-134.

78. Yao, Q.; Arachchige, I. U.; Brock, S. L., *J.Am.Chem.Soc.* **2009,** *131*, 2800-2801.

79. Nriagu, J. O.; Pacyna, J. M., *Nature (London)* **1988,** *333* (6169), 134-139.

80. Schwarzenbach, R. P.; Escher, B. I.; Fenner, K.; Hofstetter, T. B.; Johnson, C. A.; von Gunten, U.; Wehrli, B., *Science* **2006,** *313* (5790), 1072-1077.

81. Dabrowski, A.; Hubicki, Z.; Podkoscielny, P.; Robens, E., *Chemosphere* **2004,** *56* (2), 91-106.

82. Benhammou, A.; Yaacoubi, A.; Nibou, L.; Tanouti, B., *J. Colloid Interface Sci.* **2005,** *282* (2), 320-326.

83. Nagy, N. M.; Konya, J.; Beszeda, M.; Beszeda, I.; Kalman, E.; Keresztes, Z.; Papp, K.; Cserny, I., *J. Colloid Interface Sci.* **2003,** *263* (1), 13-22.

84. Blanchard, G.; Maunaye, M.; Martin, G., *Water Res.* **1984,** *18* (12), 1501-1507.

85. Lagadic, I. L.; Mitchell, M. K.; Payne, B. D., *Environ. Sci.Technol.* **2001,** *35* (5), 984-990.

86. Liu, J.; Feng, X.; Fryxell, G. E.; Wang, L.-Q.; Kim, A. Y.; Gong, M., *Adv. Mater.* **1998,** *10* (2), 161-165.

87. Manos, M. J.; Kanatzidis, M. G., *J. Am. Chem. Soc.* **2009,** *131* (18), 6599-6607.

88. Manos, M. J.; Kanatzidis, M. G., *Chem. Eur. J.* **2009,** *15* (19), 4779-4784.

89. Ding, N.; Kanatzidis, M. G., *Nat. Chem.* **2010,** *2* (3), 187-191.

90. Ozverdi, A.; Erdem, M., *J. Hazard. Mater.* **2006,** *137* (1), 626-632.

91. Erdem, M.; Ozverdi, A., *Sep. Purif. Technol.* **2006,** *51* (3), 240-246.

92. Borah, D.; Senapati, K., *Fuel* **2006,** *85* (12-13), 1929-1934.

93. Arachchige, I. U.; Brock, S. L., *Acc. Chem. Res.* **2007,** *40* (9), 801-809.

94. Arachchige, I. U. Sol-gel routes for metal chalcogenide nanoparticle assembly. Wayne State University, Detroit, 2006.

95. Son, D. H.; Hughes, S. M.; Yin, Y.; Alivisatos, A. P., *Science* **2004,** *306*, 1009-1012.

96. Arachchige, I. U.; Mohanan, J. L.; Brock, S. L., *Chem. Mater.* **2005,** *17*, 6644-6650.

97. Kistler, S. S., *J. Phys. Chem.* **1932,** *36*, 52.

98. Lieu, V. T., *J. Chem. Ed.* **1996,** *73* (9), 837.

99. Skoog, D. A.; Holler, F. J.; Nieman, T. A., *Principles of Instrumental Analysis*. Fifth ed.; Brooks/Cole: New York, 1998.

100. Egerton, R. F., *Physical Principles of Electron Microscopy*. Springer: New York, 2005.

101. Webb, P. A.; Orr, C., *Analytical Methods in Fine Particle Technology*. Micromeritics: Norcross (Georgia), 1997.

102. Gregg, S. J.; Sing, K. S. W., *Adsorption, Surface Area and Porosity*. 2nd Ed. ed.; Academic Press: New York, 1982.

103. Medintz, I.; Uyeda, H. T.; Goldman, E. R.; Mattoussi, H., *Nature Mater.* **2005,** *4*, 435-446.

104. Aldana, J.; Wang, Y. A.; Peng, X., *J. Am. Chem. Soc.* **2001,** *123*, 8844-8850.

105. Malier, L.; Boilot, J.-P.; Gacoin, T., *J. Sol-Gel Sci. Technol.* **1998,** *13*, 61-64.

106. Steckel, J. S.; Zimmer, J. P.; Coe-Sullivan, S.; Stott, N. E.; Bulovic, V.; Bawendi, M. G., *Angew. Chem. Int. Ed.* **2004,** *43* (16), 2154-2158.

107. Katari, J. E. B.; Colvin, V. L.; Alivisatos, A. P., *J.Phys.Chem.* **1994,** *98* (15), 4109-4117.

108. Colvin, V. L.; Alivisatos, A. P.; Tobin, J. G., *Phys. Rev. Lett.* **1991,** *66* (21), 2786-2789.

109. Lindau, I.; Spicer, W. E., *J. Electron Spectrosc. Relat. Phenom.* **1974,** *3*, 409-413.

110. Wagner, C. D.; Naumkin, A. V.; Kraut-Vass, A.; Allison, J. W.; Powell, C. J.; Rumble, J. R., NIST, Ed. 2007.

111. Aruguete, D. M.; Marcus, M. A.; Li, L.; A.Williamson; Fakra, S.; Gygi, F.; Galli, G. A.; Alivisatos, A. P., *J. Phys. Chem. C* **2007,** *111*, 75-79.

112. Carter, A. C.; Bouldin, C. E.; Kemmer, K. M.; Bell, M. I.; Woicik, J. C.; Majetich, S. A., *Phys. Rev. B* **1997,** *55* (20), 13 822-13 828.

113. Borchert, H.; Shevchenko, E. V.; Robert, A.; Mekis, I.; Kornowski, A.; Grubel, G.; Weller, H., *Langmuir* **2005,** *21*, 1931-1936.

114. Pala, I. R.; Arachchige, I. U.; Georgiev, D. G.; Brock, S. L., *Angew. Chem. Int. Ed.* **2010,** *49* (21), 3661-3665.

115. Greenwood, N. N.; Earnshaw, A., *Chemistry of the Elements*. Second ed.; Elsevier: Oxford, 2005.

116. Robinson, R. D.; Sadtler, B.; Demchenko, D. O.; Erdonmez, C. K.; Wang, L.-W.; Alivisatos, A. P., *Science* **2007,** *317* (5836), 355-358.

117. Dloczik, L.; Koenenkamp, R., *Nano Lett.* **2003,** *3* (5), 651-653.

118. Ristova, M.; Ristov, M., *Appl. Surf. Sci.* **2001,** *181* (1-2), 68-77.

119. Ristova, M.; Ristov, M.; Tosev, P.; Mitreski, M., *Thin Solid Films* **1998,** *315* (1-2), 301-304.

120. Li, H.; Zanella, M.; Genovese, A.; Povia, M.; Falqui, A.; Giannini, C.; Manna, L., *Nano Lett.* **2011**.

121. Jain, P. K.; Amirav, L.; Aloni, S.; Alivisatos, A. P., *J. Am. Chem. Soc.* **2010,** *132* (29), 9997-9999.

122. Luther, J. M.; Zheng, H.; Sadtler, B.; Alivisatos, A. P., *J. Am. Chem. Soc.* **2009,** *131* (46), 16851-16857.

123. Rivest, J. B.; Swisher, S. L.; Fong, L.-K.; Zheng, H.; Alivisatos, A. P., *ACS Nano* **2011,** *5* (5), 3811-3816.

124. Helfferich, F., *Ion Exchange*. McGraw-Hill Book Company, Inc.: New York, 1962; p 2.

125. Chan, E. M.; Marcus, M. A.; Fakra, S.; ElNaggar, M.; Mathies, R. A.; Alivisatos, A. P., *J. Phys. Chem. A* **2007,** *111* (49), 12210-12215.

126. Tang, Z.; Podsiadlo, P.; Sup Shim, B.; Lee, J.; Kotov, N. A., *Adv. Funct. Mater.* **2008,** *18*, 3801-3808.

127. Nakamura, H.; Kato, W.; Uehara, M.; Nose, K.; Omata, T.; Otsuka-Yao-Matsuo, S.; Miyazaki, M.; Maeda, H., *Chemistry of Materials* **2006,** *18* (14), 3330-3335.

128. Torimoto, T.; Adachi, T.; Okazaki, K.-i.; Sakuraoka, M.; Shibayama, T.; Ohtani, B.; Kudo, A.; Kuwabata, S., *Journal of the American Chemical Society* **2007,** *129* (41), 12388-12389.

129. Fryxell, G. E.; Lin, Y.; Fiskum, S.; Birnbaum, J. C.; Wu, H.; Kemner, K.; Kelly, S., *Environ. Sci. Technol.* **2005,** *39* (5), 1324-1331.

130. Pawsey, S.; Kalebaila, K. K.; Moudrakovski, I.; Ripmeester, J. A.; Brock, S. L., *J. Phys. Chem. C* **2010,** *114* (31), 13187-13195.

131. Brock, S. L.; Arachchige, I. U.; Kalebaila, K. K., *Comment. Inorg. Chem.* **2006,** *27* (103-126).

132. Chervin, C. N.; Lubers, A. M.; Pettigrew, K. A.; Long, J. W.; Westgate, M. A.; Fontanella, J. J.; Rolison, D. R., *Nano Letters* **2009,** *9* (6), 2316-2321.

ABSTRACT

METAL CHALCOGENIDE NANOPARTICLE GEL NETWORKS: THEIR FROMATION MECHANISM AND APPLICATION FOR NOVEL MATERIAL GENERATION AND HEAVY METAL REMEDIATION VIA CATION EXCHANGE REACTIONS

by

IRINA R. PALA

May 2012

Advisor: Dr. Stephanie L. Brock

Major: Chemistry

Degree: Doctor of Philosophy

The dissertation research is focused on (1) uncovering the mechanism of metal chalcogenide nanoparticle (NP) gel formation; (2) extending the cation exchange reaction protocol to zinc sulfide gel networks, with the goal of accessing new aerogel chemistries and understanding the factors that drive the process; and (3) conducting a quantitative analysis of the ability of ZnS aerogels to remove heavy metal ions from aqueous solutions.

The mechanism of metal chalcogenide NP gel formation was investigated using Raman spectroscopy and X-ray Photoelectron Spectroscopy to probe the chemical changes that occur during the gelation process. These techniques suggest that the bonding between the particles in the CdSe NP gels is due to the oxidation of surface selenide species, forming covalent Se–Se bonds. Treating the gel networks with a suitable reducing agent, such as a thiol, breaks the covalent bond and disperses the gel network. The addition of sodium borohydride, a “pure” reducing agent, also breaks down the gel network, strengthening the hypothesis that the reducing character of the thiols, not their

ligation ability, is responsible for the gel network breakdown. UV-Vis spectroscopy, Transmission Electron Microscopy and Powder X-ray Diffraction were used to analyze the particles after successive gelation-dispersion cycles. The primary particle size decreases after repeated oxidation-reduction cycles, due to NP surface etching. This trend is observed for CdSe and CdS gel networks, allowing for the proposition that the oxidative-reductive mechanism responsible for the formation-dispersion of the gels is general, applying to other metal chalcogenide NP as well.

The cation exchange reaction previously demonstrated for CdSe gels was extended to ZnS gel networks. The exchange occurs under mild reaction conditions (room temperature, methanol solvent) with exchanging ions of different size, charge and mobility (Ag^{+}, Pb^{2+}, Cd^{2+}, Cu^{2+}). The overall reaction is kinetically controlled, since systems with similar solubility, and thus similar thermodynamic driving force (e.g. PbS and CdS) exchange at very different rates. A correlation exists between the speed of the reaction and the difference between the reduction potential of the incoming cation and that of Zn^{2+}; the larger the difference, the faster the exchange. At the same time, the porosity of the aerogels and the surfactant-free surfaces hold great importance for the exchange reactions, allowing for exchange between cations of similar size and charge (i.e. Pb^{2+} for Zn^{2+}), a phenomenon that was previously reported as impossible in ligand-capped metal chalcogenide NPs. These observations allowed for a better understanding of the factors governing the cation exchange reaction in nanoscale metal chalcogenides. Quaternary ZnS-$CuInS_2$ gels were obtained by cation exchange with Cu^{+} and In^{3+}, but the pure $CuInS_2$ phase was not obtained under the mild reaction conditions used, probably due to the very different mobility of the two exchanging cations.

The kinetically fast cation exchange process and the propensity of the soft chalcogenide gel networks to bind heavy metal ions selectively, suggest that these materials could also be suitable for the removal of heavy metal ions from the environment. The dissertation research studied the capacity of ZnS aerogels to sequester heavy metal ions such as Pb^{2+} and Hg^{2+} from water. The materials are efficient in removing the heavy metal ions from aqueous solutions with a wide range of initial concentrations. For initial concentrations that mimic an environmental spill (i.e. 100 ppb Pb^{2+}), the treatment with the aerogel affords a final concentration lower than the 15 ppm action level recommended by the EPA. Under thermodynamically forcing conditions, the water remediation capacity of the ZnS NP aerogels was determined to be 14.2 mmol Pb^{2+} / g ZnS aerogel, which is the highest value reported to date.

AUTOBIOGRAPHICAL STATEMENT

IRINA R. PALA

Education

- **2006–2012 Ph.D.** Inorganic Chemistry, Wayne State University, Detroit, MI
  Dissertation: Metal Chalcogenide Nanoparticle Gel Networks: Their Formation Mechanism and Application for Novel Material Generation and Water Remediation via Cation Exchange Reactions
  Advisor: Prof. Stephanie L. Brock
- **2002–2006 B.S.** Chemistry, with High Distinction, University of Michigan-Dearborn, Dearborn, MI

Research and Teaching Experience

- **08/2006–12/2011** Graduate Research/Teaching Assistant, Department of Chemistry, Wayne State University, Detroit, MI
- **08/2004–08/2006** Undergraduate Researcher/Chemistry Tutor, University of Michigan-Dearborn, Dearborn, MI

Awards and Fellowships

- NSF funded fellowship to attend the 2011 Pan-American Advanced Studies Institute – "Scalable, Functional Nanomaterials", August 4th-14th 2011, Costa Rica
- Esther and Stanley Kirschner Graduate Award in Inorganic Chemistry, April 2011
- Summer Dissertation Fellowship, WSU Graduate School, Summer 2011
- Thomas C. Rumble Graduate Research Fellowship, Fall-Winter 2006 and Fall-Winter 2010
- Schaap Fellowship, 2007- 2009
- Esther & Stanley Kirschner General Chemistry Teaching Award, May 2009
- Departmental Citation for Excellence in Service, May 2008
- Honors Scholar in Chemistry, U of M-Dearborn, March 2006
- U of M-Dearborn Best Inorganic Student American Chemical Society Award, April 2006
- James B. Angell Scholar, March 2006
- University Honors, University of Michigan, March 2006
- Undergraduate Research Fellowship recipient, U of M-Dearborn, Summer 2005 and 2006
- College Honors Program (determined by GPA), U of M-Dearborn
- Dean's List, U of M-Dearborn, 2002-2006

Publications

- Urdaneta, M.; Stepanov, P.; Weinberg, I.N.; Pala, I.; Brock, S. *J. Instrum*. **2011**, 6, C01027.
- Pala, I. R.; Arachchige, I. U.; Georgiev, D. G.; Brock, S. L. *Angew. Chem. Int. Ed.* **2010**, 49(21), 3661–3665.
- Kaiser E. W.; Pala I. R.; Wallington T. J. *J. Phys. Chem. A,* **2010**, 114(*25*), 6850–60
- Khalid, M.; Pala, I.; Wasio, N.; Bandyopadhyay, K. *Colloids Surf. A* **2009**, 348(*1-3*), 263–269.
- Kaiser, E. W.; Donahue, C. J.; Pala, I. R.; Wallington, T. J.; Hurley, M. D. *J. Phys. Chem. A* **2007**, 111(*7*), 1286–1299.
- Smith, S. R.; Pala, I.; Benore-Parsons, M. *J. Inorg. Biochem.* **2006**, 100(*11*), 1730–1733.